Integrated HAMR Light Delivery System via High Q Resonators

Submitted in partial fulfillment of the requirements for

the degree of

Doctor of Philosophy

in

Electrical & Computer Engineering

Hongliang (Joe) Liang

B.S., Engineering, Swarthmore College
M.S., Electrical & Computer Engineering, Carnegie Mellon University

Carnegie Mellon University
Pittsburgh, PA

August, 2018

Acknowledgements

I am very thankful for the guidance and support of my adviser Prof. James Bain throughout the years of my Ph.D. I appreciate his optimistic outlook and constantly encouraging me to perform at my best. I would also like to thank Prof. Jonathan Malen, Prof. Maysam Chamanzar, and Dr. Scott Olson for taking the time to serve on my Ph.D. committee. I appreciate the many insightful discussions regarding portions of my work specific to their areas of expertise.

The staff of the Carnegie Mellon Nanofabrication Facility was important to me in fabricating the devices in this work. They brainstormed with me on certain process development steps, helped me with numerous equipment problems, and gave me good advice on how to best use some tools.

I am grateful to the many research staff and fellow graduate students who have provided assistance along the way. Lou Chomas was instrumental at the start of my Ph.D. career in training me on various lab equipment and cleanroom methodology. Within my research group, I appreciate the help I have gotten from Abhishek, Greg, Min, and Cheng-Ming. They were patient with me no matter how many questions I had. Outside of my group, I would like to thank in particular Lutong, Shafee, and Mohamed for their expertise in Lumerical modeling and allowing me to borrow their test setup to complete my experiments.

Many people outside of academics provided support to me as well. I would especially like to acknowledge Agapé Life Church and the members of the Graduate Student Ministry for their encouragement, advice, and perspective. I would like to thank my friends who regularly work out with me at the gym and members of the Pittsburgh Ultimate (Frisbee) Community for

making staying healthy and active very fun for me. Last but not least, I am deeply grateful for support from my family—I thank my parents who cultivated a desire in me to pursue knowledge and learning for the greater good; I thank my brother Jeffrey and sister Lisa for always cheering me on and believing in me. I owe my success to them all.

This work is funded by the industrial sponsors of the Data Storage Systems Center (DSSC) at Carnegie Mellon University, and their financial support of my research is appreciated.

Abstract

In the age of Big Data, the demand for higher capacity hard disk drives (HDDs) is ever increasing. To enable higher recording densities, heat assisted magnetic recording (HAMR) is being investigated as a promising approach. This technology uses a high coercivity material for the recording medium to overcome the superparamagnetic limit and a laser in the recording head to temporarily heat the medium above the Curie temperature at locations where data needs to be written. Because the generated heat spot must be in the tens of nanometers, the laser must be coupled to a near field transducer (NFT) to reduce its spot size. While numerous laser-to-NFT coupling schemes have been proposed, they involve little monolithic integration and have low coupling efficiency. We desire to improve the laser-to-NFT coupling efficiency such that optical power output requirement decrease by an order of magnitude to as low as 1 mW. We present a HAMR light delivery scheme in which we first optimize our laser through mode stabilization then couple it to the NFT by means of a waveguide and a high Q dielectric resonator, with all components placed onto the same chip. This level of integration may lead to lower manufacturing costs and a reduction in system complexity.

We begin our study by fabricating a Fabry-Perot GaAs/AlGaAs quantum dot bar laser. To optimize our laser, we first address the issue of power fluctuation as it directly affects the quality of the data written in HAMR. We minimize power fluctuation by enforcing single mode operation on the laser, achieved through a novel method of coupling the laser to a periodic array of gold NFT-like metal nanostructures. We found that at coupling distance of 50 nm the array was able to completely suppress any appearance of secondary modes as observed through the laser emission spectrum.

We continue our optimization by examining what is needed to allow the laser to operate in continuous-wave (CW) rather than pulsed to enable continuous data writing. Based on the pump duty cycle and thermal resistance of our structure, we examine different heat sinking topologies and estimate the amount of heat sinking necessary to make possible CW operation. We determine CW operation can be achieved by either using a copper heat sink or reducing the laser ridge width down to 1 μm.

The final study examines the coupling efficiency of the waveguide-resonator-NFT system using Si_3N_4 core/SiO_2 cladding. We achieve critical coupling between a rectangular waveguide and a disk resonator using a coupling distance of 100 nm, disk radius of 11 μm, and waveguide width of 1 μm. By examining the effect of the NFT on the quality factor of the resonator, we estimate a coupling efficiency from laser to NFT of 50%. Thermal characterization through resistance measurements is performed to verify launch of plasmonic modes on the NFT. The measurement results combined with simulations in COMSOL suggest a propagation length of 6 to 8 μm, which is consistent with that of a mode being launched.

In summary, this work presents an analysis of a complete HAMR light delivery system design and supports key aspects of that design with experimental confirmation of design assumptions. Specifically, the design includes a mode stabilized laser operating in CW and coupled to a NFT through a waveguide-resonator system. The coupling efficiency is improved such that the power requirements of the source laser decreases by more than an order of magnitude compared to those of current coupling schemes. The level of integration of the system can lead to lower costs and complexity for the HAMR recording head.

Table of Contents

List of Figures

List of Tables

Chapter 1: Introduction

This chapter begins with a discussion on the current state of the magnetic hard drive industry. Ever increasing demand for higher storage densities lead to the proposal of heat assisted magnetic recording (HAMR) as a promising candidate. A brief overview of this technology is given and more in-depth details are provided for its light delivery system. Various approaches to light delivery are reviewed as well as each of its components, which typically consist of a semiconductor laser coupled via some innovative mechanism to a near field transducer (NFT). Ways to improve laser operation through mode stabilization and coupling efficiency through NFT design are provided. The chapter ends with a discussion on dielectric resonators and how they may be incorporated into a high coupling efficiency HAMR light delivery system this thesis proposes. Details on the specific designs of this system will be presented in Chapter 5.

1.1 Need for Heat Assisted Magnetic Recording (HAMR)

While many devices use solid state technologies nowadays, hard disk drives (HDDs) are still ubiquitous and can be found in almost every PC and data center. Compared to solid state drives (SSDs), HDDs offer much higher capacity for the same price. Although SSDs are faster (throughput, latency, Input/Out operations/second [1]), they are still too expensive to replace the terabytes of data offered by HDDs in the space of a traditional 3.5-inch enclosure, at least for the near future [2]. The demand for higher capacity drives is ever rising, and the hard drive industry is struggling to keep up with the supply. Mark Whitby, Seagate's vice president for branded products, estimated the total amount of digital data produced around the world was 3.5 zettabytes

(10^{21} bytes) in 2013. That figure is expected to go up to 44 zettabytes in 2020, which is six more zettabytes than the expected data storage capacity available at that time [3].

For the past decade, the data capacity gap problem has been tackled by perpendicular magnetic recording (PMR) in which data bits are aligned vertically as opposed to longitudinally as in the first hard drives. To enable higher recording densities, the bits can be packed closer together and become smaller. However, as the microscopic grains that make up these bits become so tiny they will start to lose their ability to hold their magnetic orientation, causing data corruption and rendering a HDD unusable. This phenomenon is known as the superparamagnetic effect [4]. Although advances in PMR go beyond just changing the bit orientation, it only pushes back the superparamagnetic limit and does not eliminate it. It is only a temporary solution and the search for the ability to shrink the actual size of the grains continues [5].

HAMR is a promising approach to overcoming the superparamagnetic limit. By using a recording medium with higher coercivity, or the ability of a bit to retain its magnetic charge, it can counteract demagnetization and keep the bits stable under thermal fluctuations. During the write process, a laser is used to momentarily heat the recording medium above the Curie temperature to reduce its coercivity below that of the applied magnetic field from the recording head. The orientation of the applied head field encodes the data, and afterwards the heated region is rapidly cooled.

HAMR requires the development of a number of novel components such as the light delivery system, thermomagnetic writer, head/disk interface, and rapid cooling media. System level optimization of each of these components is required, with all of them presenting their own

unique challenges. The recording density of a fully realized HAMR system is expected to be up to an order of magnitude higher than that of PMR, reaching several Tb/in^2 [6].

1.2 HAMR Light Delivery: Various Approaches

At storage densities of several TB/in^2, grain sizes in the recording layer will be <10 nm in diameter and therefore require a heating spot of similar size [7]. While laser diodes, inexpensive sources of high-power coherent light, have long been a staple in optical storage, further developments in their performance beyond what has been achieved in optical storage are required for their successful implementation in the HAMR light delivery system. In particular, the delivered light spot has to overcome the diffraction limit given by:

$$d = \frac{0.5\lambda}{NA} \quad (1.2.1)$$

where d is the spot size, λ is the wavelength of the light source, and NA is the numerical aperture of the focusing lens. Near field optics is one way to achieve spot sizes much smaller than the diffraction limit by making use of apertures and antennas. Confining light to subwavelength dimensions is relatively straight forward, but the primary difficulty in HAMR is to deliver a significant fraction of incident light power within this spot to the recording medium [6].

The problem of delivering enough power to the recording medium can be alleviated if the power coupling between laser and NFT is maximized, and Figure 1 shows our vision of the placement of the light delivery system in relation to the rest of the hard drive. We note that while we are integrating the HAMR laser onto the side of the slider, it has been traditionally placed on top with its own heat sink [8]. It may be difficult to place a heat sink on the slider side, but since we use a much lower output laser source, overall temperature rise should not be more than that of

a laser with heat sink on top of the slider. The reason why we place our light delivery system on the slider side has to do with our design, which we show in Figure 2.

Before we discuss our proposed system, we show some examples of existing ideas for HAMR light delivery. In 2007, Lim *et al.* proposed a HAMR head that uses a grating structure with a nano slit cut into the middle. Incident laser light propagates into this slit through a dielectric waveguide with the grating structure at its end. Configurations of the slit were optimized, including the size, film material and thickness. FDTD simulations of grating geometry made with various metal films were performed as well. It was found that the peak intensity of optical power using the grating structure increased about 5 times with 30% smaller beam size than that of without-grating structure. A primary advantage of this design is that its fabrication process can be easily integrated with the conventional magnetic head [9].

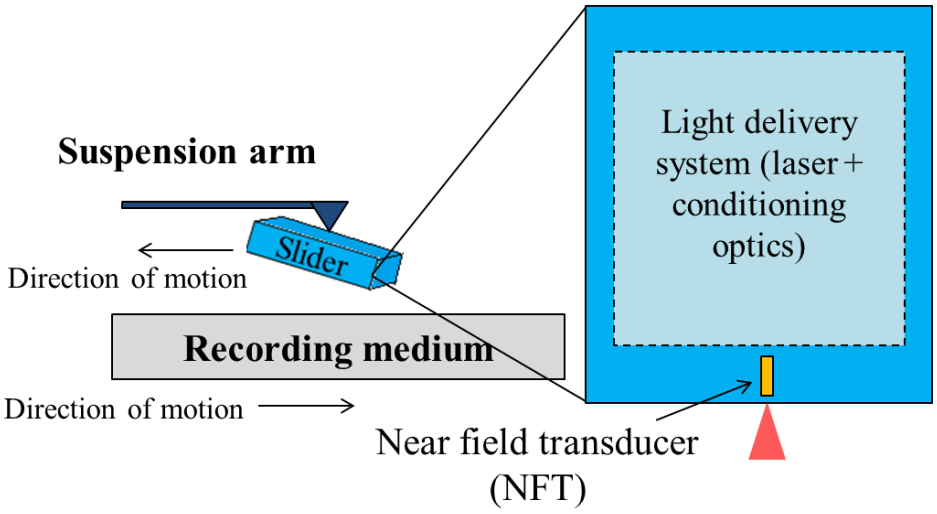

Figure 1: A HAMR head is mounted on the back of the slider, held by a suspension arm that moves in a direction of motion opposite to the recording medium. The light delivery system consists of laser, NFT, and conditioning optics that couple the two.

In 2009, Hinata *et al.* proposed a HAMR light delivery system in which coupling between an optical fiber and NFT using a triangular spot size converter (SSC) was demonstrated. The optical fiber allows flexible positioning of the laser, which sends its light into the fiber. A 45 deg. angle mirror redirects the fiber output light into the triangular SSC. The SSC is a well-known technology in optical communications that makes the fiber output spot smaller and any components connected to it more integrated. In their work, the SSC is characterized by its triangular core whose cross section becomes smaller from top to bottom while being surrounded by a cladding the entire length. In addition to efficiency in fiber spot size reduction, there is no alignment loss between SSC and NFT as they are both fabricated in one body. The entire system can be fabricated by standard photolithography techniques. Results show that the triangular SCC reduced fiber spot size by nearly a factor of 2 [10].

More recently in 2016, Krishnamurthy *et al.* presented an overall efficiency optimization of the light delivery system and in particular the waveguide-NFT-media coupling efficiency. Through the use of a multi-layer graded refractive-index (GRIN) cladding layer, they showed that a high refractive index waveguide can improve waveguide-to-plasmon mode conversion and waveguide-media-stack impedance matching, both which are essential for maximize power delivered to the NFT. The multilayer GRIN cladding layer acts as a collimating lens with a high numerical aperture and allows a power transfer efficiency of ~11.5% between the waveguide and media via a taper-based NFT [11].

The above-mentioned methods of HAMR light delivery are just a sample of the various coupling schemes that have been proposed over the years examining aspects such as reducing beam spot size and integrating with existing fabrication techniques. However, literature has been scarce on the standard for the coupling efficiency between laser and NFT and in many cases the

light delivery system require laser sources to output 30-80 mW of optical power [11]. It is known that laser diodes can convert the electrical power needed to pump them to output optical power with efficiencies as high as 70% [12]. With this "wall-plug" efficiency and the fact that a 2.5" laptop HDD may only need 700 mW for operation [13], 80 mW of HAMR laser optical power will require 114 mW of electrical power which makes up ~16% of the HDD total power consumption. We propose to make feasible a laser outputting only 1 mW for HAMR, which will drop the power consumption to less than 1% of the total. However, total power consumption varies greatly with size. For example, 3.5" desktop HDDs can consume 6.5-9 W during operation [13]. Our calculations give an idea of the most noticeable improvement in power budget that can be achieved.

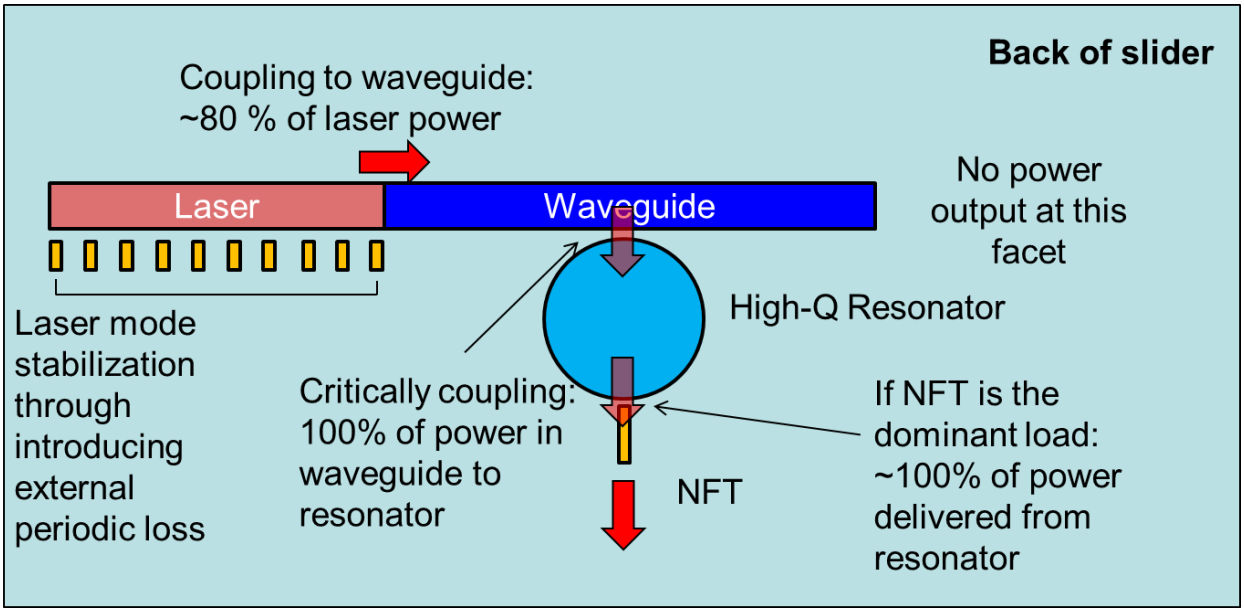

Figure 2: Schematic of our proposed HAMR light delivery system consisting of mode stabilized laser, waveguide, high-Q resonator, and NFT located on the back of the slider.

Although reductions in HDD total power consumption may be minimal depending on drive size, the level of integration our system provides will benefit all HDDs. A schematic of our

proposed system is shown in Figure 2. For our approach, we use a mode stabilized bar laser achieved through a periodic array of external metallic nanostructures is butt coupled to a waveguide. A dielectric resonator critically couples with the waveguide such that all of the light in the waveguide transfers to the resonator. Under this condition, no light should be reflected back into the waveguide and cause unwanted feedback into the laser. A NFT is placed in the near field of the resonator. If the quality factor of the resonator make the NFT to be the dominant loss, then power in the resonator should primarily leave through the NFT. This is akin to a straw sucking out liquid from a container, with NFT being the straw and resonator containing the liquid that is light.

Traditionally, advances in integration in other technologies have brought numerous benefits. For example, in the world of microprocessors integration has led to tremendous increases in computational power and decreases in cost and power consumption [14]. Integration of CMOS (Complementary metal-oxide-semiconductor) and MEMS (Microelectricalmechnical Systems) technologies improves the performance of MEMS devices, allowing for smaller packages and lower instrumentation cost [15]. In the area of photonic integrated circuits (PICs), the monolithic integration of many optical components into a single photonic substrate and device has provided benefits for optical transmissions systems such as packaging consolidation, increased system density, reduced power consumption, reduction in fiber couplings, and improved reliability [16]. Examining the benefits that integration brings to these technologies, we observe that lowering system cost and complexity seem to be common themes. We believe the level of integration that our system offers will similarly benefit HAMR.

1.3 Laser Mode Selection Schemes

The semiconductor laser serves as the foundation of the HAMR light delivery system. Therefore, it is paramount that its performance be optimized. In particular, it is important to enforce single mode operation as multimode operation introduces fluctuations in power. For HAMR, these fluctuations may cause magnetic recording jitter and thus data to be written unreliably. To understand the source of these fluctuations, first note that all lasers have some degree of noise. Their output spectra depend strongly on case temperature and injection current. For example, the wavelength of GaAs based laser shifts slowly with temperature at ~0.06 nm/^{o}C but may sometimes take discrete jumps as large as 0.3 nm/^{o}C. These large shifts occur when the laser switches from one mode to another in a phenomenon known as mode hopping. During this event, the laser's output intensity fluctuates depending on the spacing between adjacent modes. Besides HAMR, mode hopping have been a problem in a variety of applications from video disc systems, where it causes variation in the location of the data to be written and quality of picture derived from disk, to telecommunications, where switching from one mode to another affects the maximum data transmission rate [17].

One way to achieve wavelength stability and mitigate mode hopping is to build the laser cavity such that only a single mode is resonant and all other modes are unfavorable. A distributed feedback (DFB) laser enforces a single mode by including a periodic grating structure inside its cavity, often on top of the gain region. The gratings act as a distributed reflector in the wavelength of the lasing spectrum range, and only one mode is favored in terms of losses. The downside to DFB lasers is that to integrate the grating structure with the laser gain region requires time-consuming regrowth techniques. An alternative is to place these gratings laterally to both sides of the gain region which may not require regrowth but may deliver lower power

[18]. Typical output powers are in the tens of milliwatts, and linewidth is a few hundred MHz, exhibiting high wavelength stability [19].

Another structure that employs periodic gratings is the distributed Bragg reflector (DBR) laser. Compared to DFB, the distinguishing difference between the two is the location of the grating within the epitaxial structure. DBR uses a surface grating that is outside of the gain medium. The grating structure provides wave-length dependent feedback to define emission wavelength. Using a specific number of layers, it can provide maximum reflection for a given wavelength [20]. These layers high index contrast and reflectivity whereas the gratings in DFB are low index contrast and reflectivity. Although DBR does not require regrowth for the gratings that DFB needs, both types of structures rely on sophisticated semiconductor fabrication techniques of etching, lithography, and chemical vapor deposition [18]. In terms of cost, DBR and DFB are similarly priced [21]. However, they are at least 2-3 times more expensive than traditional Fabry-Perot (non-mode stabilized) lasers [22].

In recent years, a concept known as parity-time (PT) symmetry have been implemented in coupled ring lasers to enforce single mode operation. First introduced within the context of mathematical physics [23], it has attracted increasing attention since it was shown that the eigenvalues of non-Hermitian Hamiltonians $\widehat{H}^* \neq \widehat{H}$ can be entirely real if they respect PT symmetry, $PT\widehat{H} = \widehat{H}PT$ [24]. The Hamiltonian H is an operator used in quantum mechanics to specify the energy levels and time evolution of a system [25]. H is described as "Hermitian" because it has several special properties, with one of them being that the operator will always have real eigenvalues [26]. In the physical world, this guarantees that the energy spectrum is real and that time evolution is unitary (the probability of finding a particle *somewhere* is one and it cannot just "vanish") [27]. A non-Hermitian Hamiltonian with complex $\widehat{H}$ not equal to its

complex conjugate $\widehat{H}^*$ will normally lead to complex energy eigenvalues and be non-unitary in time evolution [28]. However if there is symmetry with H in space reflection and time reversal, respectively represented by operators P and T, then the eigenvalues of H will be physically meaningful even if H is non-Hermitian.

One way PT symmetry translates to a photonics arrangement is to have an open system with balanced gain and loss. Hodaei *et al.* experimentally characterized the behavior of active coupled microring resonators designed using this concept. Two ring lasers are evanescently coupled to each other side by side where one provides gain and the other is subjected to loss. They examined the coupling strength through the laser emission spectra and found that by properly adjusting the coupling strength and gain-loss contrast, an inherently multi-moded laser can be forced to operate in single-longitudinal resonance [29]. It is this idea that loss can be deliberately introduced into a laser to cause one mode to be highly favored over all others inside the gain medium that will be further explored in Chapter 3.

1.4 Near Field Transducer (NFT) Designs

In addition to the laser, the other main component in the light delivery system is the NFT, responsible for reducing the laser spot size below the diffraction limit to the tens of nanometers and fulfilling the high storage density requirements of HAMR. The NFT is essentially a nanoplasmonic structure, and these types of structures have found uses in a variety of applications such as label-free biomedical sensing [30], nano-optical tweezers [31], surfaced enhanced Raman spectroscopy (SERS) [32], plasmonic photovoltaic devices [33], and photothermal cancer cell therapy [34]. Although this thesis will not focus on the optimization of

this structure, several leading NFT designs that maximize its coupling efficiency to the recording media, shown in Figure 3, will be presented in this section for completeness.

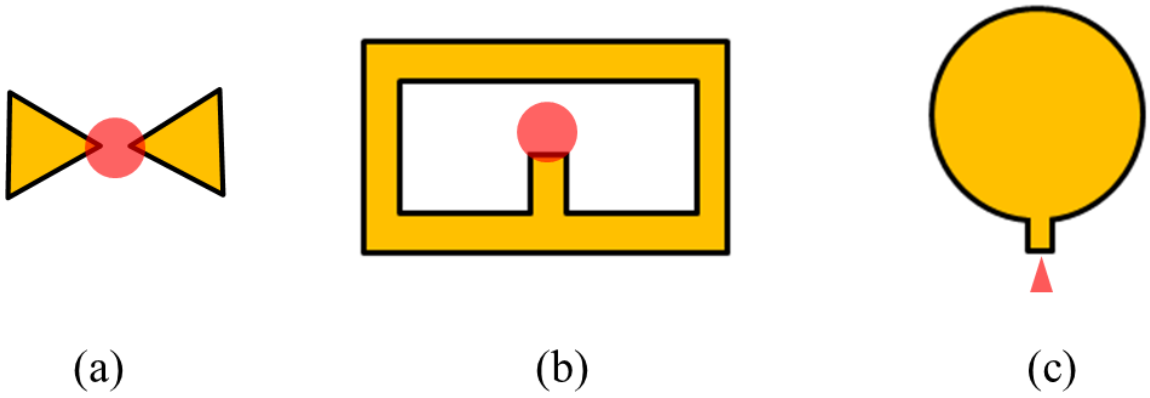

Figure 3: Various popular NFT designs with heat spot shown in red: (a) bowtie antenna, (b) C-shape aperture, and (c) lollipop design

Many NFT designs are based on localized surface plasmon (LSP) resonance, which are oscillations of surface charges bounded to a finite structure such as a metal-dielectric interface [35]. One NFT design uses a circular aperture in an opaque metallic film though power transmission efficiency is far from ideal. Thus, other aperture shapes have been proposed to further increase coupling efficiency to the recording medium such as the triangle, C- and L-shape, and bowtie apertures with the C-shape aperture design shown theoretically to demonstrate some of the highest NFT coupling efficiencies [6].

Ikkawi *et al.* performed a detailed study using finite element simulations on the optimization of C-shape aperture parameters, focusing on its throughput, near-field intensity distribution and polarization effect. The power throughput was found to be an order of magnitude higher than L-shaped apertures. In addition, while bowtie antennas demonstrated optimum focusing it did not show the highest transmission efficiency compared to C-shaped

apertures. With an element size of 70nm, the C-shaped aperture yielded a few microwatts of power into a spot with full width at half maximum of 95nm [36].

In addition to apertures, NFTs can also be based on antennas. One of the earliest is the bowtie antenna which was initially demonstrated at microwave frequencies but has been shown later to also operate at near infrared and visible wavelengths. By choosing the dimensions of the antenna appropriately, any charge accumulated on its surface can oscillate at the local surface plasmon resonant frequency, a phenomenon that can be stimulated by incident light. One of the main challenges facing the bowtie antenna is that its resonance characteristics change drastically when placed in proximity to a metallic recording medium such as that used in HAMR. Other antenna designs that have been investigated include nanowires and the beaked triangle antenna [6].

Challener *et al.* demonstrated a NFT for HAMR with efficient optical energy transfer that combines the best characteristics of the C aperture and bow tie antenna into the "lollipop" transducer [37]. One of these enhancements is building a sharp tip to take advantage of the lightning rod effect in which charges accumulate at the sharpest areas of an object to produce the strongest electric field. Compared to LSP, no resonance is involved in this phenomenon [35]. Drawing inspiration from the bowtie antenna, the electric field can also be enhanced in a narrow gap between 2 resonant nanoparticles. The first step to completing the lollipop NFT is to build a planar solid immersion mirror (PSIM) which is a parabolically shaped waveguide with a NA much larger than 1 that can focus incident light to about a quarter of its wavelength. However, HAMR requires even smaller spots so a peg is placed at the focus of the PSIM, forming a "lollipop". An electric field is generated at its tip due to the lightning rod effect, and energy is coupled into the medium directly below the peg. A plasmonic layer is placed underneath the

medium to generate the same kind of response on the electric field as a gap would between 2 nanoparticles. Therefore, coupling to the medium is further enhanced by the additional confinement of the electric field [37].

While optical transmission efficiency of the NFT is important for HAMR, there is also a need to study the thermal behavior of the NFT as unwanted self-heating is detrimental to its functionality. Often, the metals typically used for NFTs operate well as plasmonic materials in the optical wavelength range. However, such materials are inherently lossy and generate heat in the metals themselves, raising their temperature by several hundred degrees. This temperature rise may lead to an expansion of the NFT and its subsequent failure due to thermal stress [38]. Since the working of HAMR hinges on the functionality of the NFT, we will address the thermal issue as well as discuss how various NFT designs may be incorporated into our light delivery system in Chapter 7.

One important area that this work does not address is the NFT coupling behavior to the recording media as it involves a problem of impedance matching [39]. However, we can make some reasonable assumptions about the NFT such that the results presented are still relevant. We expect a temperature rise in the NFT of several hundred degrees [37]. For concreteness, we pick 300 K which is similar to the value found in [40]. Assuming that media needs 300 μW for recording [11] and NFT to media coupling efficiency is 5% [39], there will be 6 mW in the NFT. The thermal resistance of the NFT needs to be 300 K/6 mW = 5 x 10^4 K/W or less for the above scenario to be possible. We confirm this thermal resistance value for our NFT in Section 5.4.

1.5 Dielectric Resonators

In this section we discuss the workings of dielectric resonators (DRs) and will explain how we can use one to couple the laser to the NFT in Chapter 5. The DR consists of a high refraction index material as core surrounded by a low refraction index material as cladding. Optical waves are confined inside the resonator because of the abrupt change in the refraction index between core and cladding, and they continuously reflect off the insides of the core. A distinguishing characteristic of the resonator is its Q, or quality factor:

$$Q = \frac{f_c}{\Delta f} \quad (1.5.1)$$

where f_c is the central frequency and Δf is the bandwidth taken at full width half maximum (FWHM), as shown in Figure 4.

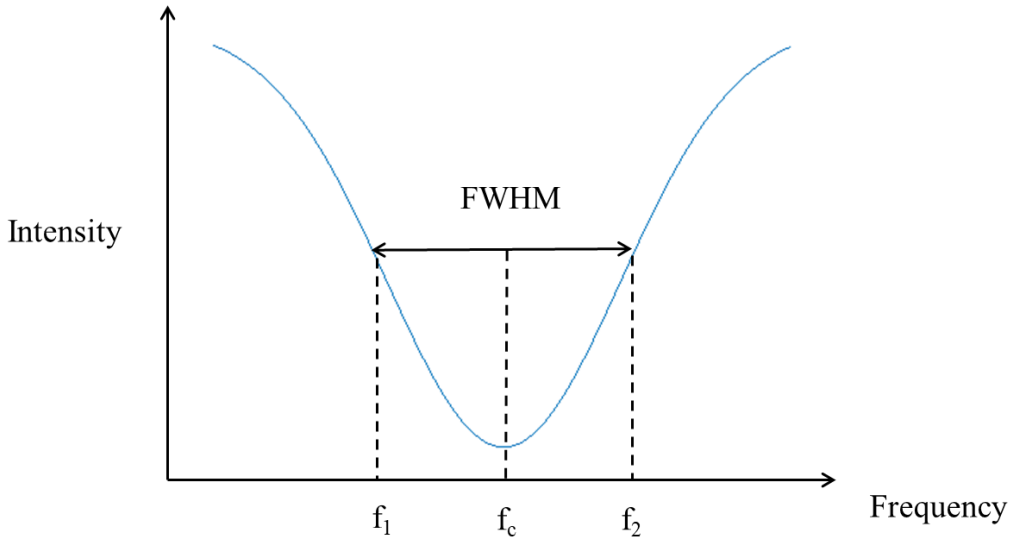

Figure 4: In a generic plot of intensity (for example, waveguide output transmission in the presence of a coupled resonator) vs. frequency, $\Delta \boldsymbol{f} = \boldsymbol{f_2} - \boldsymbol{f_1}$ and $\boldsymbol{Q} = \frac{\boldsymbol{f_c}}{\Delta \boldsymbol{f}}$. Note that f_1 and f_2 is taken at FWHM.

The DR was first invented as a high-Q element for use in filters and oscillators. A higher Q indicates a lower rate of energy loss, making it ideal as an energy storage device [41]. In reality, a practical DR will always have some external loss due to radiation or dissipation in a surrounding metal shield, and any such losses will reduce the Q of the DR cavity. Note here that there is a distinction in Q of "unloaded" vs. "loaded". The former means that the DR is in isolation from the rest of the system while in the latter the DR is connected to the system. In the rest of this thesis, any figures cited for Q will be loaded unless otherwise stated.

Wang *et al.* found that a cylindrical shape with thickness greater than diameter as most advantageous for DR among several of their theoretically explored geometries. With this shape, the lowest frequency resonant mode is the transverse electric (TE) mode, which has a circular field distribution [42]. Although they were envisioning the DR for applications in circuits, the cylindrical shape can also be easily fabricated for use in photonics applications.

Soltani *et al.* investigated a DR for chip-scale silicon photonics. They demonstrated an ultra-high Q microdisk resonator in a silicon-on-insulator (SOI) platform and characterized the Q to be near $3x10^6$ which corresponds to a propagation loss of 0.16dB/cm [43]. In their work, they were interested in coupling the resonator to a nearby waveguide in which 100% transmission of energy from waveguide to resonator was theoretically possible. Key challenges in realizing such a system were the reduction of scattering and absorption loss induced by sidewall roughness and engineering the waveguide-resonator system to achieve critical coupling. This concept of critical coupling is an important aspect in our work as well and will be explored in Chapter 2.

A DR that is not high in Q also has its own applications. For example with a low Q, the DR has a high rate of energy radiation. In such a scenario, the DR becomes an antenna which is

praised for its high efficiency, low loss, wide bandwidth, compact size, and 3D modeling flexibility. Many applications associated with wireless communications for DR antennas exist in commercial and defense sectors [41].

It is even possible for a DR to operate simultaneously as a high-Q resonant cavity and low-Q radiating element. Hady *et al.* achieved this feat by enclosing their DR in a rectangular cavity that acts as a shield for the resonating TE mode but transparent to radiating transverse magnetic (TM) mode. The high-Q mode is coupled to a microstrip line while the low-Q mode is coupled to a coaxial probe with capacitive plate [44].

For our application, we require the use of a high-Q DR. With a high-Q, it is difficult for energy to escape from the DR. However, if we can setup the NFT as the only outlet for energy to leave the DR, then a high fraction of the system energy can be coupled to the NFT. We have shown this concept in our HAMR light delivery system in Figure 2 and will discuss in more detail in Chapter 5.

Chapter 2: Background Theory

In this chapter, the background theory necessary to understand the work in the rest of this thesis is presented. We start with a discussion of the basic operation principles of a semiconductor laser and highlight concepts such as population inversion and gain. We then focus on the properties of the laser cavity such as the types of losses present, the degree of quantum confinement to assist in photon generation, and wave propagation framed within Maxwell's equations and approximated by a dielectric slab waveguide. We continue with an examination of mode operation in the laser and how standing waves are formed. This information will be particularly useful when we explain how we stabilize our laser modes in Chapter 3. To assist in the understanding of our proposed light delivery system for HAMR, we also present mode operation in a disk resonator via whispering gallery modes. Finally, we end the chapter with a discussion on critical coupling between a waveguide and a resonator in which theoretically 100% of the power can be transferred from the former to the latter. One can imagine that if laser light can be coupled into a waveguide, then all of that light can be sent into a critically coupled resonator.

2.1 Operation of Semiconductor Laser

The word laser is an acronym for *light amplification by stimulated emission of radiation*, which is a concise summary of how the device works. A semiconductor laser consists of a gain medium sandwiched by p-type and n-type materials to form a p-n junction. In waveguide terms, the p- and n-type materials can be called cladding, which optically confines light through use of materials with lower indices of refraction than that of the cavity, and the gain medium can be called the core. Because of the use of the p-n junction, a semiconductor laser is also known as a

laser diode. What distinguishes the laser from the diode is that fact that the laser has a resonant cavity which can amplify the light inside. A simple setup is the Fabry Perot laser in which light bounces back and forth between two mirrors that are placed parallel to each other, with one ideally being totally reflective and the other partially reflective to serve as the light output [45]. Such a cavity is shown in Figure 5.

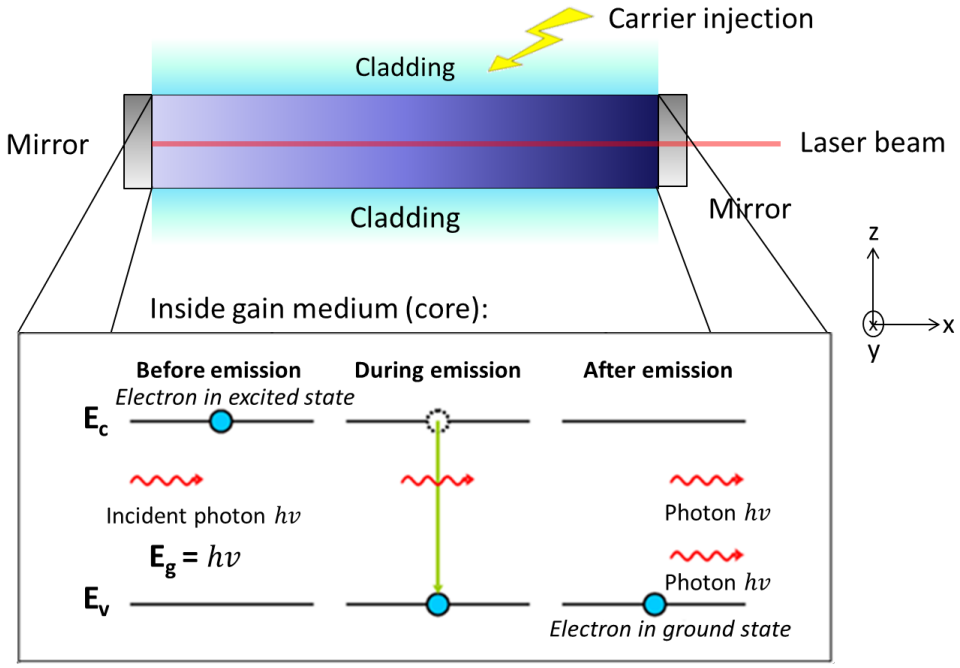

Figure 5: An electrically pumped semiconductor laser is shown. Stimulated emission occurs when an incident photon causes an electron to fall from the conductance band to the valence band. A second photon is generated with the same phase and frequency. Laser beam exists through the less reflective mirror.

For a semiconductor/diode laser, the mirrors of the resonant cavity are usually formed by cleaving the ends, and typical facet reflectivities for semiconductor materials are ~30%. Dielectric coatings can be applied to modify the reflectivities. In applications where cleaving is not possible such as those requiring monolithic integration or lasers with rounded geometries, i.e. ring lasers, the facets can also be etched though the quality will not typically be as good as those

attained by cleaving [46]. Laser cavity lengths range anywhere from 50 to 2000 μm, with commercial lasers typically ranging from 200 to 1000 μm long [47].

Our lasers are electrically pumped in which a source current injects electrons into the laser in an excited state. When an incident photon hits an electron in this state, the electron is stimulated to transition from the conduction band to the valence band where it recombines with a hole, which is the absence of an electron. A photon is emitted that has the same phase and energy as the incident photon, contributing to laser gain. These photons travel back and forth within the resonant cavity by reflecting off the end mirrors. They continue to stimulate emission of more photons to build up a large radiation field. This radiation will be monochromatic because each photon has the same energy and coherent because all photons will have the same optical phase [48]. This is also demonstrated in Figure 5.

The resulting light created from the recombination serves as a gain mechanism, with the wavelength being determined by the bandgap of the gain material [47]. When electrical pumping builds up to a point where the majority of the electrons are in the conduction band, it causes a *population inversion* and brings the laser to its *lasing threshold*. Stimulated emission will dominate over any other sources of emission and the gain balances the losses in the system. Low losses would translate to the device having higher gain at lower pump currents and therefore achieving lasing at lower operating power [45].

2.2 Laser Cavity Losses

Since the laser cavity is essentially a waveguide, light will experience attenuation, or loss, as it travels down this waveguide. This section discusses loss resulting from internally within the

cavity. In addition, since this thesis presents work on ring lasers in Chapter 4, we will also discuss bending loss in this section.

Losses from within the cavity are aptly named internal loss, but it is a catch-all term describing a variety of losses such as diffraction losses at mirrors and absorption loss in the cladding regions. This section will focus on scattering loss as it is a significant contribution to internal loss and can be heavily impacted by fabrication techniques.

Scattering loss occurs because the propagating waves interact strongly with the surfaces of the waveguide. A wave traveling in the guide experiences many bounces, and the frequency of the bounces increases with higher order modes, a term referring to the integral number of wavelengths that fit within the resonant cavity. When a photon travels into a rough surface, the roughness may change its direction. Thus it will be out of phase with the rest of the photons and no longer contributing to stimulated emission. This process is shown in Figure 6a.

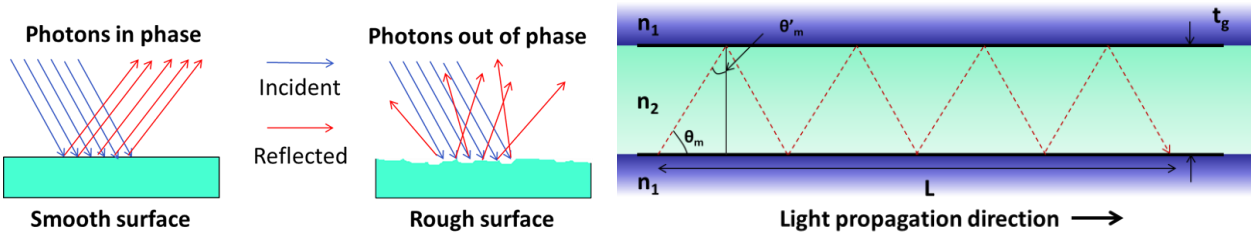

(a) (b)

Figure 6: (a) Process in which surface roughness can increase scattering loss. (b) Light propagating down a waveguide of length L and scattering each time it bounces off a side wall. The cladding and core refraction indices are represented by n_1 and n_2 respectively, and their difference results in total internal reflection. The waveguide width is t_g and propagating wave has reflection angle $\boldsymbol{\theta_m}$.

Scattering loss can be quantitatively defined if light is assumed to travel in a fashion as shown in Figure 6b. In a waveguide of length L, the number of reflections N_R off each surface can be calculated by [49]:

$$N_R = \frac{L}{2t_g cot\theta_m} \quad (2.2.1)$$

where t_g is the waveguide thickness and θ_m is the angle of reflection for an incident ray off the waveguide sidewall as shown in Figure 6b. Due to the differences in refraction indices between the core and cladding, the light wave should be entirely confined within the waveguide by total internal reflection. Snell's Law explains the relationship between the material refraction indices and the angle of the incident light:

$$n_1 sin\theta_i = n_2 sin\theta_t \quad (2.2.2)$$

The incident and transmitted angles are represented respectively by θ_i and θ_t. Figure 7a shows a light wave incident on the interface between core and cladding.

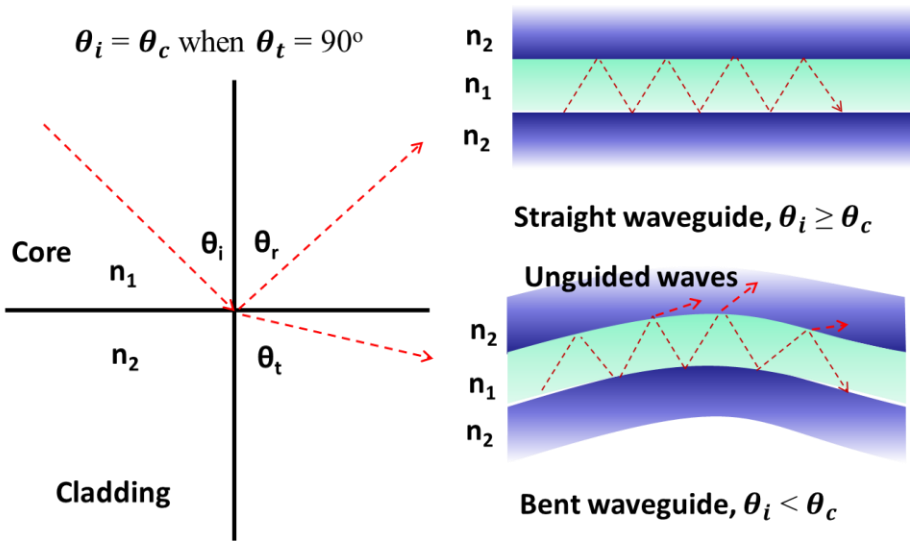

(a) (b)

Figure 7: (a) Light incident upon interface between core and cladding. Total internal reflection occurs when the incident angle is greater than or equal to the critical angle. (b) Loss arises in bent waveguides as they may cause the incident angle to dip below the critical angle.

When the transmitted angle is greater than or equal to 90^o, the incident angle at which this occurs is called the critical angle, causing total internal reflection.

Bending loss is due to propagating waves hitting the sidewall of the waveguide at angles less than the critical angle for total internal reflection, as shown in Figure 7b. Suppose in a straight waveguide that the index contrast between the core and cladding regions are chosen such that the angle of an incident wave hitting the sidewall is equal to or greater than the critical angle. If a bend is introduced to the waveguide, the wave will be incident at a sharper angle. As the bending radius decreases, this angle will drop below the critical angle and loss occurs as part of the wave is transmitted.

Since minimizing sources of optical loss can reduce extra heat dissipation in the laser, it is desirable to eliminate scattering and bending loss as much as possible. Scattering loss can be

reduced by improving sidewall smoothness while bending loss can mostly be avoided above a certain minimal radius. At the lasing threshold, the gain must balance the loss. Higher losses lead to higher thresholds, resulting in increased heat dissipation.

2.3 Degree of Quantum Confinement

The current threshold of a laser has a large impact on its operation, and if it is too high the device may overheat before being able to lase. One way to lower the current threshold is to exploit quantum effects in the gain region, in particular quantum confinement of electron-hole pairs such that they recombine more easily. Thus, fewer carriers are needed as input for stimulated emission and the current threshold is lowered. The laser used in this thesis employs InAs quantum dots (QDs) embedded in the gain region, and in this section we will set up the analytical framework necessary to understand the advantages of QD lasers.

We first examine the behavior of a single electron by finding the energy levels it can occupy and its wave function. An electron can be represented a wave function φ which is itself a function of position and time. Note that φ multiplied by its complex conjugate φ^* gives us the possibility of finding a particle at that position at time *t*. The wave function can be obtained by solving Schrödinger's equation:

$$-\frac{\hbar^2}{2m}\nabla^2\varphi + V\varphi = -\frac{\hbar}{j}\frac{d\varphi}{dt} \quad (2.3.1)$$

where $\hbar$ is Planck's constant, *m* is the mass, and *V* is the potential experienced by the electron. It is often difficult to find solutions to Schrödinger's equation for realistic potential fields. However, to illustrate the theory, we can use the problem of a particle in a potential well with boundaries having infinite potential, shown in Figure 8.

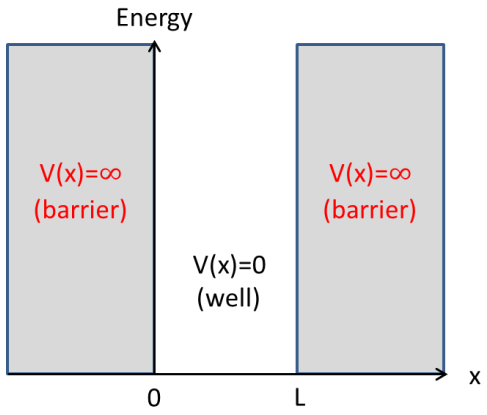

Figure 8: A potential well with zero potential inside and infinite potential outside.

The well is zero potential inside and surrounded by infinite potential barriers. Let us simplify Schrödinger's equation to be time independent and only varying in the x direction in position:

$$\frac{d^2\varphi(x)}{dx^2} + \frac{2m}{\hbar^2}\big(E - V(x)\big)\varphi(x) = 0 \quad (2.3.2)$$

where E represents the energy physically but mathematically is a separation constant resulting from making the equation independent from time. Solving eq. (2.3.2) for E with boundary conditions $V(x) = 0$ when $0 < x < L$ and $V(x) = \infty$ when $x < 0$ or $x > L$ results in:

$$E = \frac{n^2\pi^2\hbar^2}{2mL^2} \quad (2.3.3)$$

where n is the energy level number. This term along with π comes from satisfying the conditions of the wave function such that the particle cannot exist anywhere outside the well. Then since we know we have 100% chance of finding the particle in the well, we can integrate the product $\varphi^*\varphi$ from $x = 0$ to $x = L$ and set it equal to 1. This gives us the wave function [48]:

$$\varphi(x) = \sqrt{\frac{2}{L}}\sin\frac{n\pi}{L}x \quad (2.3.4)$$

To have complete information about a system we should know all of its possible energies and wave functions. However, solving Schrödinger's equation for each particle in the system is impractical and sometimes even impossible. Fortunately, we can use a function called the density of states, *g(E)*, to find the total concentration *N* of available states in an energy range E_1 to E_2 [50]:

$$N = \int_{E_1}^{E_2} g(E)\, dE \quad (2.3.5)$$

and

$$g(E) = \frac{\Delta n}{\Delta E} = \frac{dn}{dE} \quad (2.3.6)$$

The density of states has been calculated for bulk (3D), quantum well (2D), quantum wire (1D), and quantum dot (0D) in literature ([50], [51], and [52]). Their graphical representation is shown in Figure 9.

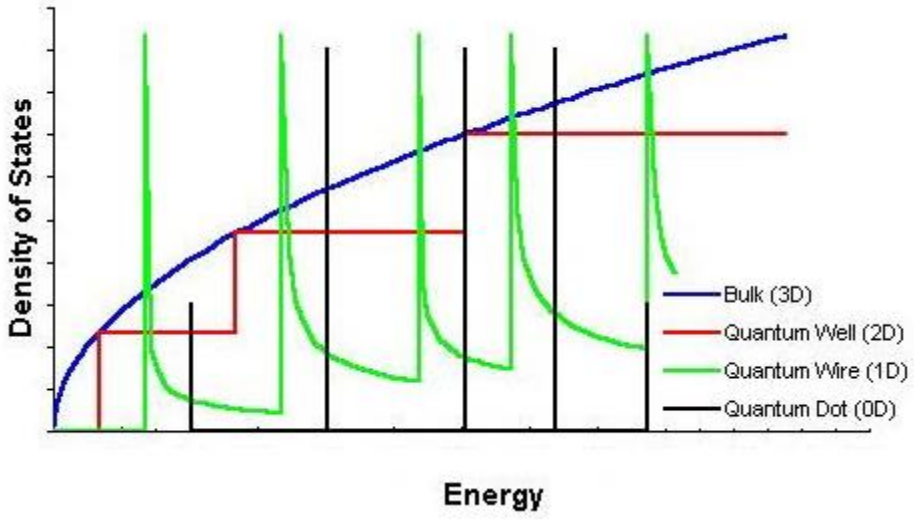

Figure 9: Density of states vs. energy calculated for bulk (3D), quantum well (2D), quantum wire (1D), and quantum dot (0D) **[53]**.

Note that as the number of translational degrees of freedom of the carriers is reduced (3D→0D), the density of states decreases from being present in a whole range of energies to just several discrete ones. When going to a lower dimensional space, the number of energy levels that can exist decreases as well. The energy levels of a quantum well structure is shown in Figure 10.

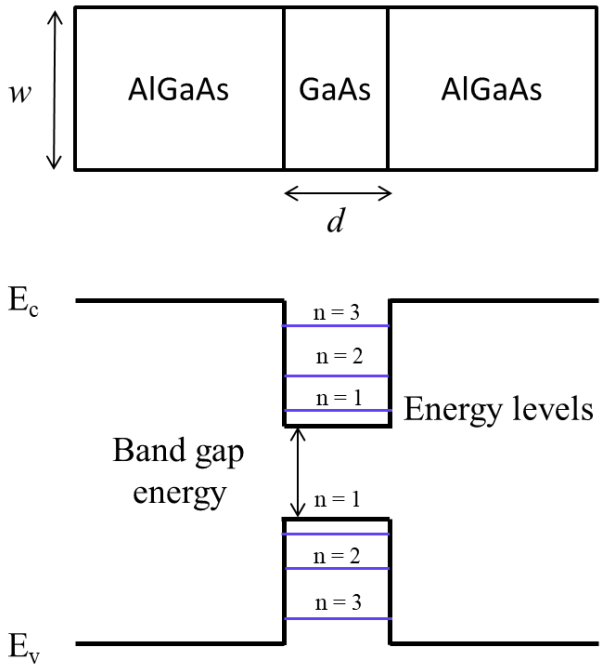

Figure 10: Energy band diagram for a GaAs/AlGaAs quantum well structure. The GaAs thickness *d* determines how many energy levels are allowed to exist within the well.

The quantum well is made by sandwiching a thin layer of a lower energy band gap material, in this case GaAs, between 2 materials of higher energy band gap such as AlGaAs. The thinner the GaAs, the fewer energy levels can exist for an electron trapped in that layer. This behavior can be approximated by an electron in a potential well with infinite potential boundaries as illustrated in Figure 8. The quantum well only provides quantum confinement by decreasing the thickness *d* of the GaAs. A quantum wire can be made if the width *w* were to decrease as well to the

magnitude of d in Figure 10. Finally, if the length of the GaAs into the page is shrunk to the magnitude of d, then a quantum dot is formed.

Compared to quantum wells and quantum wires, QDs provide a high limit on size quantization in solids and a large change of electronic properties. Thus, QDs offer exciting possibilities because they have already experimentally exhibited properties expected for zero-dimension systems. When used in the active region of carrier injection lasers, these properties strongly increase gain and improve the temperature stability of the threshold current. The δ-function like density of states and strong confinement for electron-hole recombination are the basis for improved device characteristics.

Several additional requirements must be satisfied in order for the QDs to be useful for devices. The minimum size for QDs is directly related to the conduction band offset (ΔE_c) in the material system used because at least one electron level in a QD must be available. For example assume 0.3 eV for a GaAs/AlGaAs system, the diameter of a QD in this case should not be smaller than ~4 nm. As QD size is increased, the separation between energy levels becomes comparable to the thermal energy kT so that the occupation of higher energy levels cannot be ignored. This puts an upper limit on the size of QDs, and for GaAs/AlGaAs, it is ~12 nm [52].

The main challenge in prohibiting widespread use of QDs in lasers is fabrication. While quantum wells were made possible because epitaxy allowed control at an atomic scale, higher order quantum confinement progressed more slowly because it relied on lateral processes such as patterning and etching, which have not progressed to the atomic scale as quickly [54].

2.4 Dielectric Slab Waveguide

The laser structure used in this work that will be presented in Chapter 3 is similar to a dielectric slab waveguide in that there are three layers, with the middle layer as the guiding layer and designated as layer 1. Layers 2 and 3 are the top and bottom cladding layers. They have indices of refraction n_1, n_2, and n_3 respectively. The dielectric slab waveguide can be formed by sandwiching a high-index guiding layer between 2 layers with lower indices such that $n_1 > n_2$ and $n_1 > n_3$, as shown in Figure 11. If $n_2 = n_3$, the waveguide is symmetric and it would be asymmetric otherwise [55]. Although our actual sample will not have infinite thickness (in *x*-direction) for layers with indices n_2 and n_3 as it would be in an idealized slab, their thicknesses have been chosen such that the modes will be confined to the gain region. In addition, our sample is also of finite width (in *y*-direction). However, the analysis of the dielectric slab still applies since we are only analyzing optical confinement in the *x*-direction for now.

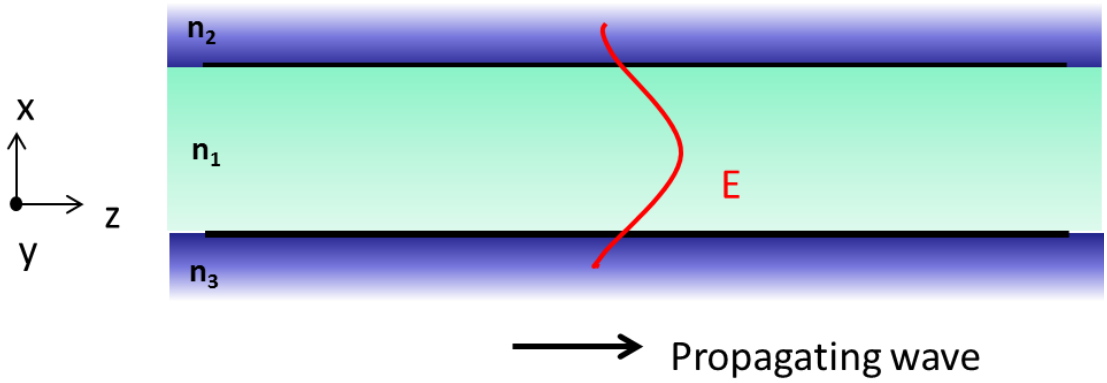

Figure 11: The y-component of the electric field is shown to propagate in a dielectric slab waveguide with a core index refraction of n_1 and cladding index of refraction n_2 and n_3. In such a waveguide, $n_1 > n_2$ and $n_1 > n_3$.

The propagation of waves is governed by Maxwell's Equations which is a collection of four equations upon which form the foundation of classical electromagnetism [56]:

$$\nabla \cdot \mathrm{D} = \rho \quad (2.4.1)$$

$$\nabla \cdot \mathrm{B} = 0 \quad (2.4.2)$$

$$\nabla \times \mathrm{E} = -\frac{\delta \mathrm{B}}{\delta t} \quad (2.4.3)$$

$$\nabla \times \mathrm{H} = \mathrm{J} + \frac{\delta \mathrm{D}}{\delta t} \quad (2.4.4)$$

where E (not be confused with the *E* that represents energy as defined in Section 2.3) is the electric field strength, H is the magnetic field strength, B is the magnetic flux density, D is the electric displacement, J is the electric current density, and ρ is the electric charge density. The four quantities E, H, B, and D are vectors in 3D space (represented by non-italicization instead of vector notation) and functions of both space and time. In analyzing the slab waveguide, we will only use a subset of these equations.

Two commonly analyzed modes in the dielectric slab waveguide are the transverse electric (TE) and transverse magnetic (TM) modes where the electric fields E and magnetic fields H are transverse to the direction of propagation respectively. In Figure 11, the field components present for TM mode are E_x, H_y, and E_z while for TE they are H_x, E_y, and H_z [56]. The modes obey the Helmholtz Equation (shown in one dimension) which can be derived from Maxwell's Equations:

$$\frac{d^2\mathrm{E}}{dx^2} + (k_0^2 n_i^2 - \beta^2)\mathrm{E} = 0 \quad (2.4.5)$$

where k_0 is the free space wave number, n_i is the index of refraction for layer *i*, and β is the longitudinal propagation constant. This equation is made under the assumption that the E field is uniform in the y-direction, and there is a z-dependence of the form $e^{j\beta z}$. Furthermore, the

relationships between the E and H fields can be derived for both modes. For TE, they are in terms of E_y:

$$H_x = -\frac{\beta}{\omega\mu_0} E_y \qquad (2.4.6)$$

$$H_z = -\frac{j}{\omega\mu_0} \frac{dE_y}{dx} \qquad (2.4.7)$$

where ω is the frequency in radians and μ_0 is the permeability of free space. For TM, the equations can be written in terms of H_y:

$$E_x = \frac{\beta}{\omega n_i^2 \varepsilon_0} H_y \qquad (2.4.8)$$

$$E_z = \frac{j}{\omega n_i^2 \varepsilon_0} \frac{dH_y}{dx} \qquad (2.4.9)$$

Here ε_0 is the permittivity of free space [56]. Inside the laser structure that will be discussed in the next chapter, the propagating modes will not be strictly TE or TM but instead a hybrid of the two.

2.5 Mode Operation in Laser

The mode *m* of a laser during operation refers to the integral number of half wavelengths λ that resonate within a cavity of length *L* such that a standing wave is formed:

$$L = m\frac{\lambda}{2} \qquad (2.5.1)$$

Figure 12 shows the formation of standing waves within a laser cavity from a ray optics approach starting from the lowest order mode, *m* = 1, also called the fundamental mode.

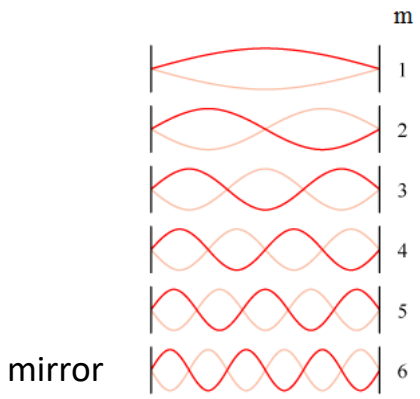

Figure 12: Standing waves forming in a cavity from lowest order mode m=1 to m=6.

The dark red is the incident wave while the light red is the reflected wave. Note that these two waves have the same frequency and amplitude while moving in opposite directions. With 2 parallel plane mirrors at the cavity ends, these waves can constructively interfere and become standing waves. The points along a standing wave where the wave has minimum amplitude are called nodes and where the wave has maximum amplitude are called antinodes. These modes explain that only specific frequencies are possible inside the cavity of a laser according to the standing wave condition. From these possible frequencies, only those that have amplification above a certain minimum, the lasing threshold, will be emitted out as light [57]. The frequency spacing Δv between adjacent modes is given by:

$$\Delta v = \frac{c}{2nL} \quad (2.5.2)$$

where c is the speed of light, n is the effective refractive index, and L is the cavity length. The frequency of the mode m is thus $\Delta v \cdot m$. During lasing, many longitudinal modes are present with the lasing mode order as high as 2000-3000.

Let us now move into a more rigorous discussion of standing waves using solutions to Maxwell's Equations (2.4.1-4). From an electromagnetic point of view, a standing wave consists of electric fields E and magnetic fields H that are 90^o out of phase, as shown in Figure 13. They do not propagate but simply oscillate in space and time [58].

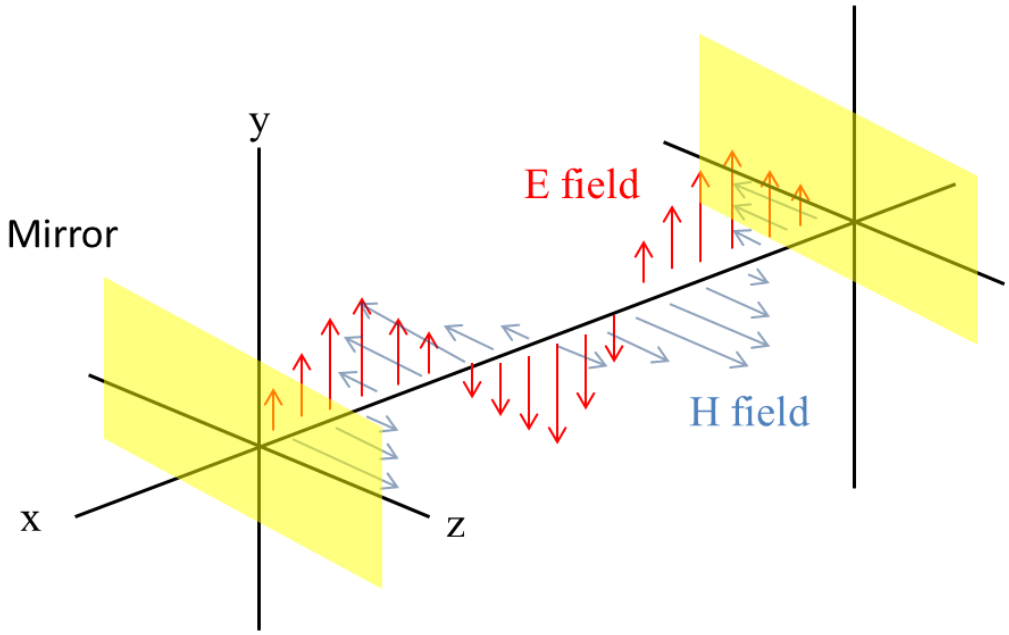

Figure 13: Formation of standing electromagnetic waves between 2 mirrors.

For two sinusoidal plane electromagnetic waves, the wave moving in +x direction can be represented by:

$$\mathrm{E}_{1y}(x,t) = \mathrm{E}_{10}\cos(k_1 x - \omega_1 t), \quad \mathrm{H}_{1z}(x,t) = \mathrm{H}_{10}\cos(k_1 x - \omega_1 t) \quad (2.5.3)$$

and the wave moving in the –x direction can be represented by:

$$\mathrm{E}_{2y}(x,t) = -\mathrm{E}_{20}\cos(k_2 x - \omega_2 t), \quad \mathrm{H}_{2z}(x,t) = \mathrm{H}_{20}\cos(k_2 x - \omega_2 t) \quad (2.5.4)$$

where k is the wave vector and ω is the frequency. Assume for simplicity that these waves have the same amplitudes with $E_{10} = E_{20} = E_0$ and $H_{10} = H_{20} = H_0$ as well as wavelengths with $k_1 = k_2 = k$ and $\omega_1 = \omega_2 = \omega$. Using superposition, the E and H fields can be written as:

$$\mathrm{E}_y(x,t) = \mathrm{E}_{1y}(x,t) + \mathrm{E}_{2y}(x,t) = \mathrm{E}_0[\cos(kx - \omega t) - \cos(kx + \omega t)] \quad (2.5.5)$$

$$\mathrm{H}_z(x,t) = \mathrm{H}_{1z}(x,t) + \mathrm{H}_{2z}(x,t) = \mathrm{H}_0[\cos(kx - \omega t) - \cos(kx + \omega t)] \quad (2.5.6)$$

Using trigonometric identities the E and H fields can be simplified to [58]:

$$\mathrm{E}_y(x,t) = 2\mathrm{E}_0 \sin(kx)\sin(\omega t) \quad (2.5.7)$$

$$\mathrm{H}_z(x,t) = 2\mathrm{H}_0 \cos(kx)\cos(\omega t) \quad (2.5.8)$$

The waves described by (2.5.7-8) are standing waves. Upon further examination, eq. (2.5.7) shows that the total E field is zero if sin kx = 0, or

$$x = \frac{n\pi}{2} = \frac{n\pi}{2\pi/\lambda} = \frac{n\lambda}{2},\ n = 1, 2, 3 \ldots \quad (2.5.9)$$

This result corresponds with the ray optics approach of Figure 12 where there is a node at every half wavelength spacing of the cavity mode. Note that if we substitute eq. (2.5.9) into eq. (2.5.8), we find that $\cos(kx) = \pm 1$ and the nodes of the E field correspond with the anti-nodes of the H field.

2.6 Mode Operation in Disk Resonator

Standing waves also occur inside disk resonators. However, because these standing waves form resonant modes around the inside of a circular cavity, they are referred to as whispering gallery modes (WGMs). First used by Lord Rayleigh in the 19th century, it describes

the acoustic phenomenon of the whispering gallery located under the dome of St. Paul's cathedral in London. It was known that a sound whispered at one end of the dome could still be heard clearly at the other end, which was a large distance away. Lord Rayleigh noted that the sound seemed to "stick" to the dome's walls and propagate only near the surface of the concave wall of the gallery [59].

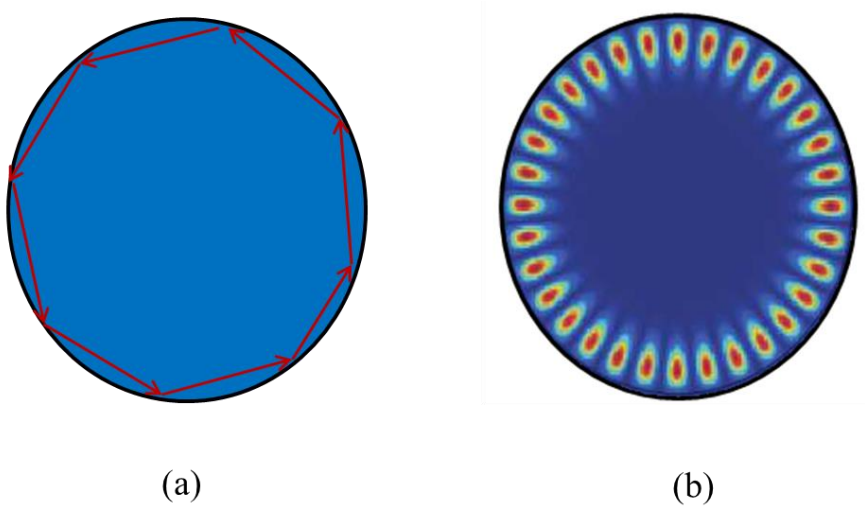

Figure 14: (a) A geometric representation of waves (red arrows) traveling inside a disk resonator and bound by total internal reflection. (b) Sample electric field distribution in a disk resonator with the color red representing the highest intensity.

For optical waves inside a resonator, the modes are guided by means of repeated total internal reflection and can continue indefinitely if we neglect any absorption, scattering, or material dispersion [60]. This is shown in Figure 14a with a geometric representation. In Figure 14b, the same modes are shown as electric field intensities.

A disk resonator can support multiple WGMs of differing order. Generally, these modes are found through finite difference methods or detected by experimental means [60]. However,

the disk resonator possesses a high degree of symmetry and therefore analytical solutions exist ([61] - [62]). Figure 15 shows the disk resonator in a cylindrical coordinate system:

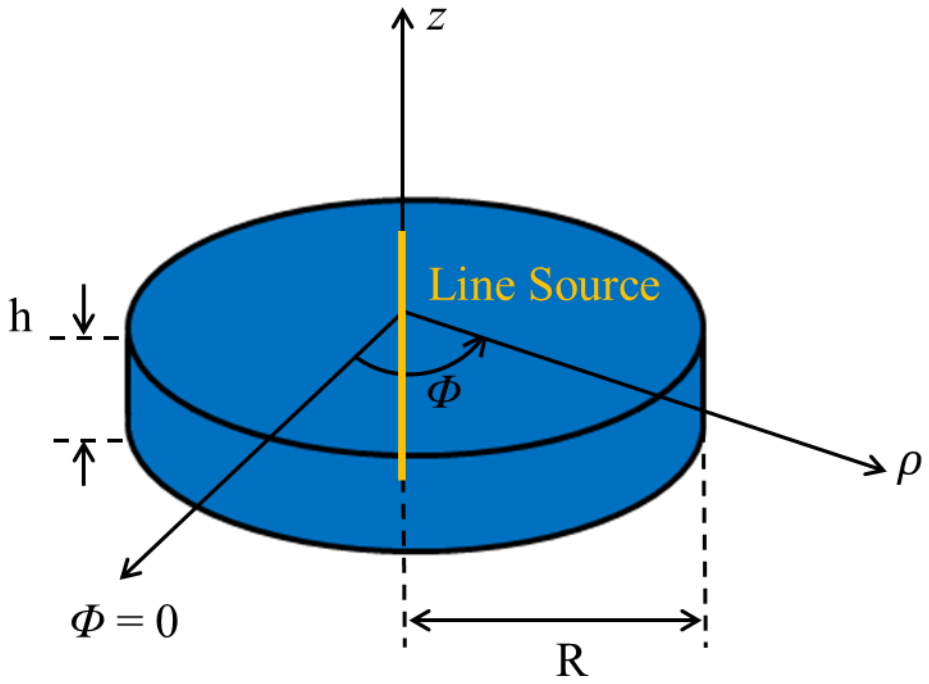

Figure 15: Disk resonator in a cylindrical coordinate system with waves (not shown) expanding from a line source.

The disk resonator is essentially a cylinder with $R >> h$. As such, when analyzing the propagation of waves inside the cavity the resonator can be considered as a slice of a circular waveguide [63]. A line source travels directly in the middle of this waveguide, and wavefronts emitted from the line source are cylindrical. The waves expand to fill a cylinder of radius R, and the wavefront crosses a cylindrical area with amplitude proportional to $A_0/\sqrt{R}$, where A_0 is the initial wave amplitude [64].

The optical solutions of the disk resonator can be grouped into TE and TM modes [62]. To solve for these modes, we first convert Maxwell's Equations to cylindrical coordinates and find eq. (2.4.5), the Helmholtz Equation, in the new coordinate system [65]:

$$\frac{1}{\rho}\frac{\delta}{\delta\rho}\left(\rho\frac{\delta\varphi}{\delta\rho}\right)+\frac{1}{\rho^2}\frac{\delta^2\varphi}{\delta\Phi^2}+\frac{\delta^2\varphi}{\delta z^2}+k^2\varphi=0 \quad (2.6.1)$$

Note that the E and H fields are shown as a generalized wave function φ. The components of the field vectors can be calculated in terms of φ [66]. We replace φ with E_z and H_z for TM and TE mode respectively. As such the other field vector components can be written in terms of E_z and H_z with dielectric slab mode approximation [61]:

$$\mathrm{H}_\rho=-\frac{j}{\mu_0\omega}\frac{1}{\rho}\frac{\delta \mathrm{E}_z}{\delta\Phi} \quad (2.6.2)$$

$$\mathrm{H}_\Phi=\frac{j}{\mu_0\omega}\frac{\delta \mathrm{E}_z}{\delta\rho} \quad (2.6.3)$$

$$\mathrm{E}_\rho=\frac{j\mu_0\omega}{k_0^2n^2}\frac{1}{\rho}\frac{\delta \mathrm{H}_z}{\delta\Phi} \quad (2.6.4)$$

$$\mathrm{E}_\Phi=-\frac{j\mu_0\omega}{k_0^2n^2}\frac{\delta \mathrm{H}_z}{\delta\rho} \quad (2.6.5)$$

For TM mode, $H_z = 0$ and $E_z = 0$ for TE mode. In Chapter 5 when we discuss our disk resonator, we gauge its performance by finding the quality factor and analyzing losses in the system.

2.7 Critical Coupling between Waveguide and Resonator

Now that we are familiar with whispering gallery modes in a disk resonator, we concern ourselves with how to couple maximum power into the resonator. One setup is to have a strip of rectangular waveguide placed near the resonator at a distance such that any light traveling through the waveguide evanescently couples into the resonator. By choosing the coupling

distance d, we can control how much power is coupled into the resonator [61]. Figure 16 shows a generic geometry for waveguide resonator coupling, according to schematic in [67]:

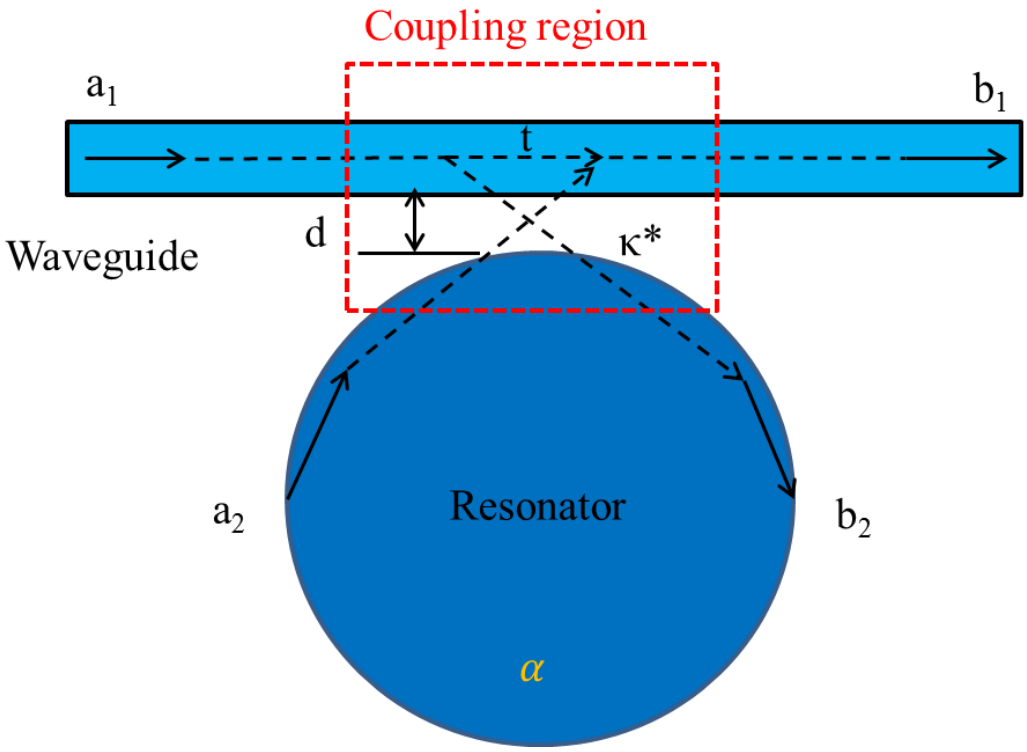

Figure 16: Generic geometry for waveguide coupling to disk resonator.

Yariv makes two simplifying assumptions that can be readily applied to our waveguide resonator system: coupling is limited to waves traveling in one direction in the waveguide with no reflections and no losses take place such that total power entering and leaving the coupling region where power exchange takes place, signified by the red dotted box, are equal. Then coupling can be described by two constants t and κ relating the E field amplitudes a_1, b_1, a_2, and b_2:

$$\begin{vmatrix} b_1 \\ b_2 \end{vmatrix} = \begin{vmatrix} t & \kappa \\ \kappa^* & -t^* \end{vmatrix} \begin{vmatrix} a_1 \\ a_2 \end{vmatrix} \quad (2.7.1)$$

Eq. (2.7.1) is supplemented by the circulation condition in the disk:

$$a_2 = b_2 \alpha e^{j\theta} \quad (2.7.2)$$

where α can be either the loss or gain in the resonator cavity and θ is the phase shift per circulation of wave propagation. The transmission factor in the input waveguide can be calculated from eq. (2.7.1-2):

$$\left|\frac{b_1}{a_1}\right|^2 = \frac{\alpha^2 + |t|^2 - 2\alpha|t|\cos\theta}{1 + \alpha^2|t|^2 - 2\alpha|t|\cos\theta^*} \quad (2.7.3)$$

If we take the incident power $|a_1|^2$ to be unity and the system is in resonance such that $\theta = m2\pi$ where *m* is an integer, then eq. (2.7.3) simplifies to:

$$|b_1|^2 = \frac{(\alpha - |t|)^2}{(1 - \alpha|t|)^2} \quad (2.7.4)$$

Two important conclusions of eq. (2.7.4) are that the transmitted power $|b_1|^2 = 0$ when $\alpha = t$, which is the condition for critical coupling and small changes in α for a given *t* result in large changes in power transmitted for a high-Q resonator [67].

Examining the wave function φ of a mode in the resonator and how it varies with time, we find that [68]:

$$\frac{\delta\varphi}{\delta t} = -j\omega_0\varphi - \frac{1}{\tau}\varphi + \eta a_1 \quad (2.7.5)$$

where ω_0 is the resonant frequency, τ is the decay rate, and η is the coupling coefficient of the forward input wave a_1. This coefficient can be calculated by means of an overlap integral [69]:

$$\eta = \frac{|\iint \varphi_{waveguide}(x,y)\varphi^*_{resonator}(x,y)dxdy|^2}{\iint \varphi_{waveguide}(x,y)\varphi^*_{waveguide}(x,y)dxdy \iint \varphi_{resonator}(x,y)\varphi^*_{resonator}(x,y)dxdy} \quad (2.7.6)$$

In reality solving the integral analytically is too cumbersome if not impossible in some cases, and results are usually obtained through simulation. Critical coupling in this case would be signified with $\eta = 100\%$.

This thesis will demonstrate critical coupling through experimental methods. A laser will send light propagating down one side of a waveguide and a power meter will be placed at the other end. Through plotting the power transmission spectra, we can get an idea of the coupling efficiency as well as the quality factor of the resonator. More details will be presented in Chapter 5. We will also demonstrate the coupling of the NFT to the resonator using COMSOL simulation in Chapter 5.

Chapter 3: Laser Behavior with Mode Stabilizing Structures (MSS)

We have shown our proposed HAMR light delivery system in Figure 2 in which we use a mode stabilized laser as the source. In this chapter, we examine the mode stabilization of GaAs/AlGaAs based InAs QD lasers via periodic arrays of adjacent metallic mode stabilizing structures (MSS). We begin with a simulation study on the interaction of a single MSS with a standing wave in a laser cavity. MSS placement in all three dimensions, which include the coupling distance, is varied to explore the evanescent coupling strength. Based on this information, we design a periodicity for our MSS array so as to influence the laser to lase at the mode most favorable to this periodicity. We then show detailed steps on the fabrication our devices and highlight the challenges presented by the need of accurately placing the MSS near the laser gain medium. Post fabrication, the lasers are characterized by obtaining their emission spectra and threshold current. These results serve as the basis on which we analyze the impact of MSS on laser behavior and reconcile experimental data with simulation. Our findings are summarized in this chapter's Conclusion section.

3.1 MSS Design Rationales

The rationale behind using MSS to stabilize a laser mode is that it makes certain modes lossier than others, and the laser will pick the least lossy mode during lasing. In this section we explore a coupling scheme that is different from conventional coupling of parallel waveguides. We begin with the analysis of a single MSS which can be thought of as a NFT coupling to the laser. However, we find that it is not feasible to couple a NFT directly to the laser and thus the

idea of the MSS to stabilize the laser mode is born. Shown in Figure 17, the NFT couples directly to a light containing cavity, be it laser, waveguide, or resonator.

To understand how the coupling works, we first take a look at the mode structure present in each device. Figure 18a shows a cross section for a rectangular NFT as seen from the side that couples NFT, with the mode that is most stable for HAMR derived from the simulation results of Chabalko in [70].

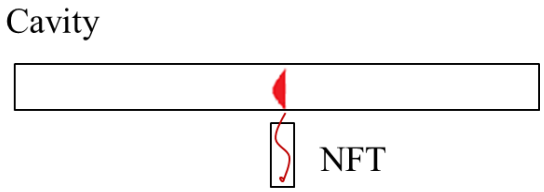

Figure 17: A NFT evanescently couples to a light containing cavity.

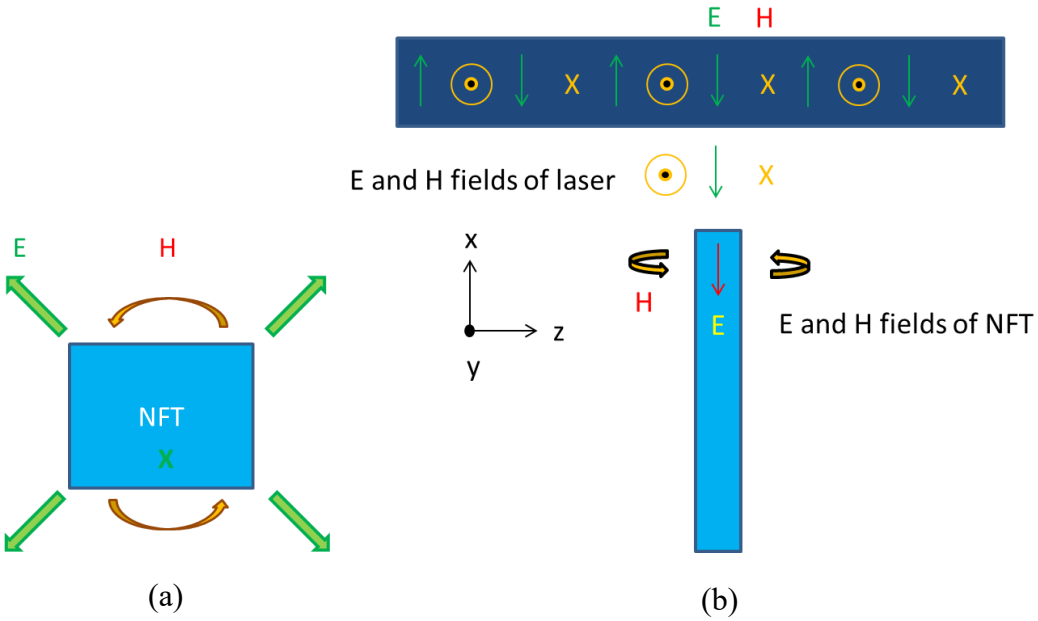

Figure 18: (a) E and H field of a rectangular NFT cross section, from the side that couples to a light containing cavity. (b) E and H fields of the laser can be coupled to those of the NFT.

A circular magnetic field is present as well as electric fields that radiates out and propagate into the page. Examining the E and H fields of the cavity shown in Figure 18b, we see that the E and H fields alternate with each other, with themselves alternating in direction. In the figure, E fields (E_x) oscillate up and down while the H fields (H_y) oscillate in and out of the page. If the NFT is placed in proximity, this H field can couple to the circular H field of the NFT and the E field couples to the NFT E field that propagates down its length. This coupling is expected to excite a wave to be launched down the NFT. The coupling efficiency is expressed analytically in eq. (2.7.6) but we will obtain it here using COMSOL simulation, building the model as shown in Figure 19:

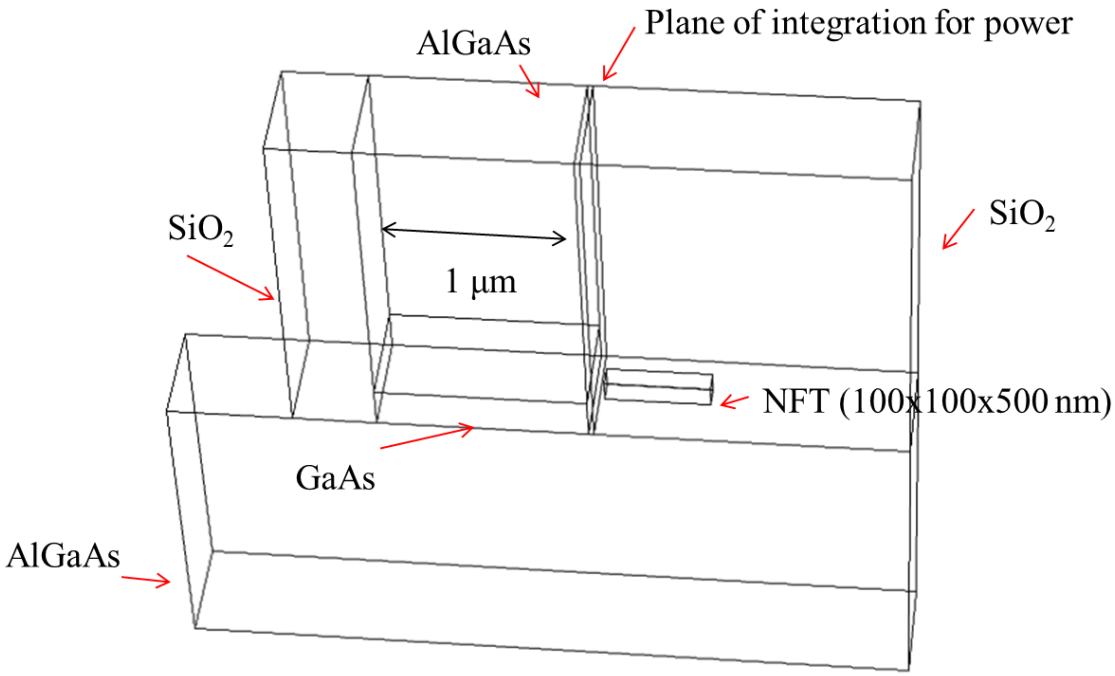

Figure 19: COMSOL model of a cross section of our laser with gold NFT placed next to gain medium.

In this model, we have a 200 nm thick GaAs gain region sandwiched by 1500 nm of AlGaAs on the top and bottom. The laser ridge is 1μm wide, and it is bounded on both sides by SiO_2

cladding. The NFT, made of Au and of size 100 by 100 by 500 nm, is placed next to the gain medium. A detailed description of the laser structure and the fabrication steps to achieve it are provided in Section 3.2.

We launch a wave simultaneously from the front and back end of the GaAs gain region such that a standing wave is formed inside the cavity. The E field profile for 50 nm coupling distance is shown in Figure 20. Note that the waveguide center, where the NFT is placed, does not exactly align to the E field maximum.

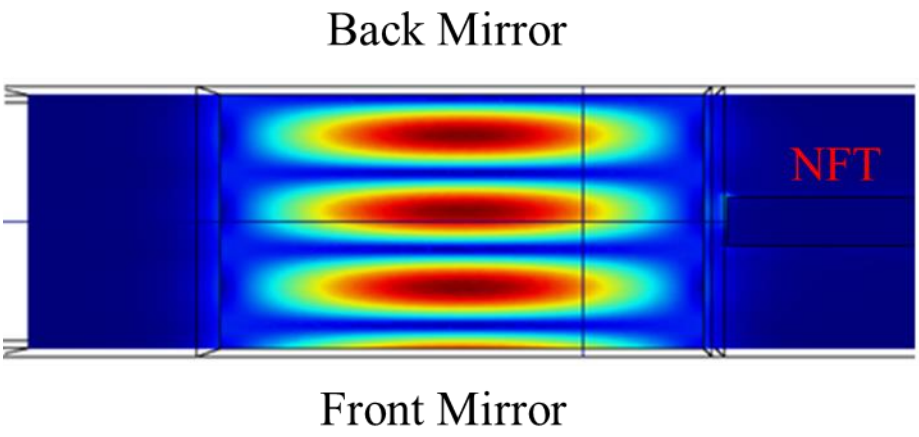

Figure 20: Top view of E field profile of standing wave in cavity. The NFT, although placed halfway between the front and back mirrors, do not align with the E field maximum.

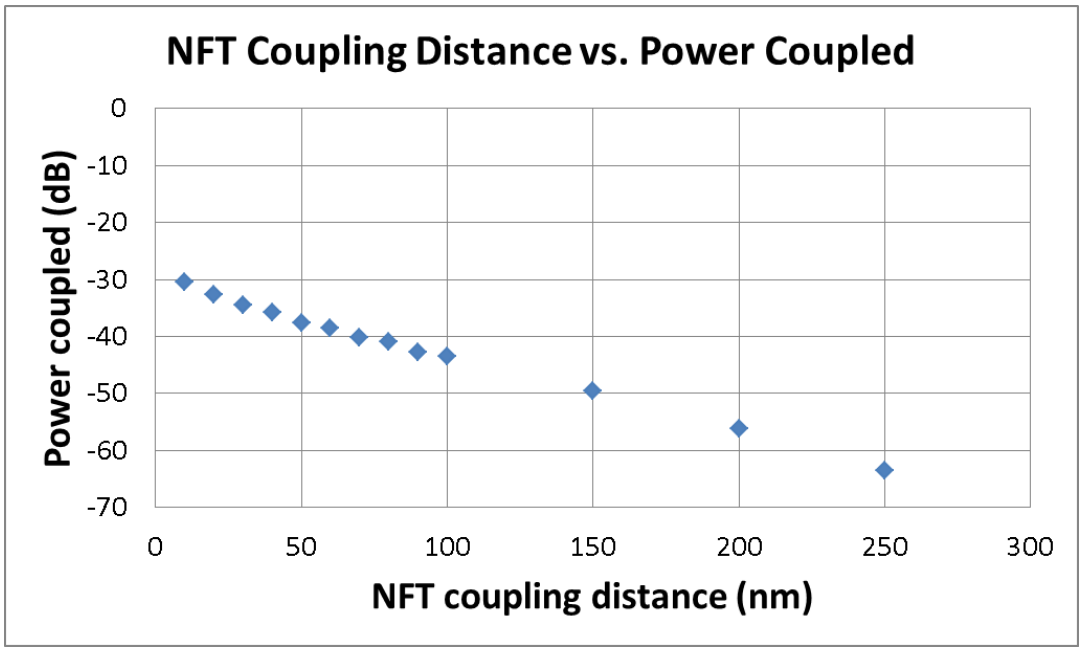

Figure 21: A plot of NFT coupling distance vs. power coupled.

We then vary the coupling distance from 0 to 250 nm, with the results shown in Figure 21. We note that the power coupled to the NFT drops by 10 dB in the first 50 nm and by 200 nm it has decreased by nearly 20 dB. This is also the reason why we cannot couple a NFT directly to the laser this way since the efficiency will be much too low (~0.03%). Due to fabrication constraints which will be discussed in the next section, the closest coupling distance we are confident in placing the NFT to the gain medium is 50 nm. At this distance, we vary the lateral position of the NFT relative to the node of a standing wave in the laser cavity and observe the power coupled as shown in Figure 22. When the NFT is aligned to the node, the power coupled is at a minimum. At 75 nm away from the node, the power coupled reaches a maximum. These locations correspond to the minimum and maximum of the propagating E field respectively.

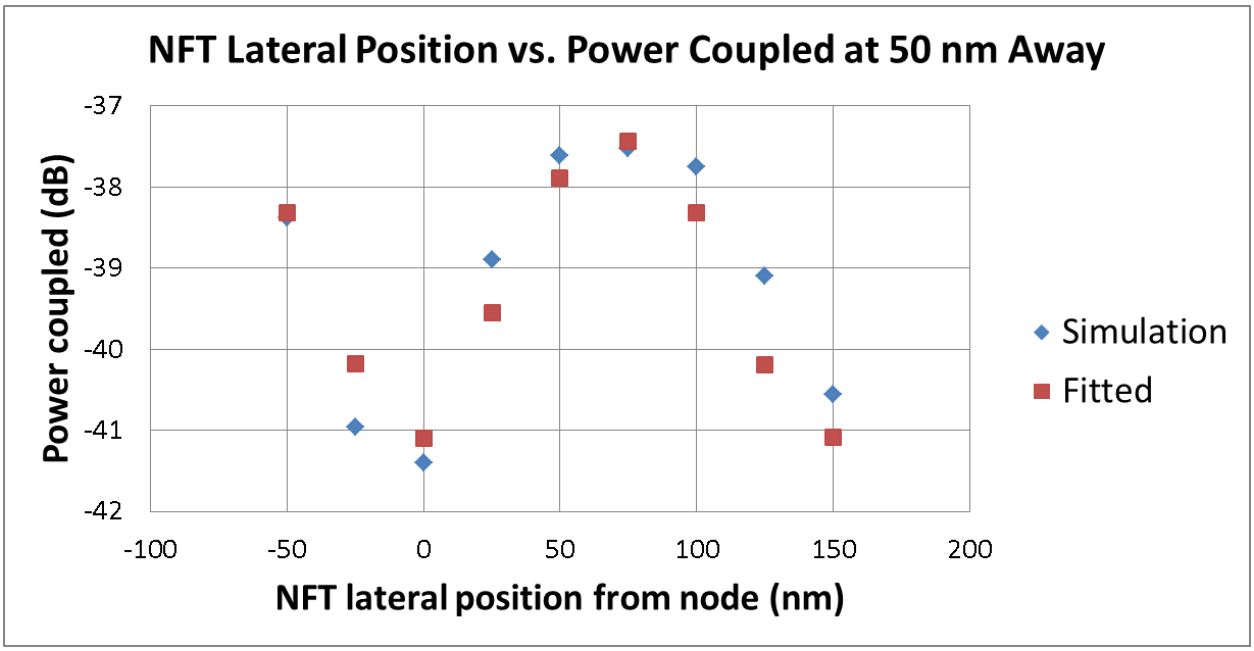

Figure 22: A plot of power coupled vs. NFT lateral position from the node (E field min) of a standing wave as reference. The NFT is placed at 50 nm away from the gain region. Simulated results are shown as blue diamond markers and the fitted results are shown as red square markers.

The simulated results are represented by blue diamond markers. We fit this data with a sinusoidal equation of the form A*cos(B*x* - C) + D:

$$1.04 \times 10^{-4} \cos(4.19 \times 10^{7} x - 26) + 2.58 \times 10^{-4} \quad (3.1.1)$$

where *x* is the lateral position of the NFT. The power coupling calculated using eq. (3.1.1) is represented by red square markers in Figure 22. We use this equation to show that for an array of MSS configured to favor a certain mode, all other cavity modes will have a stronger coupling interaction with the array and thus incur more loss. Figure 23 compares the total power coupled by an MSS array for design mode 3000 and 2 adjacent modes in each direction if a MSS is placed at every node of the E field within 50 nm of a 1000 μm laser cavity. The standing wave formed inside the cavity carries 2W. If the laser tries to shift to adjacent modes the power coupled immediately increases by ~0.3W.

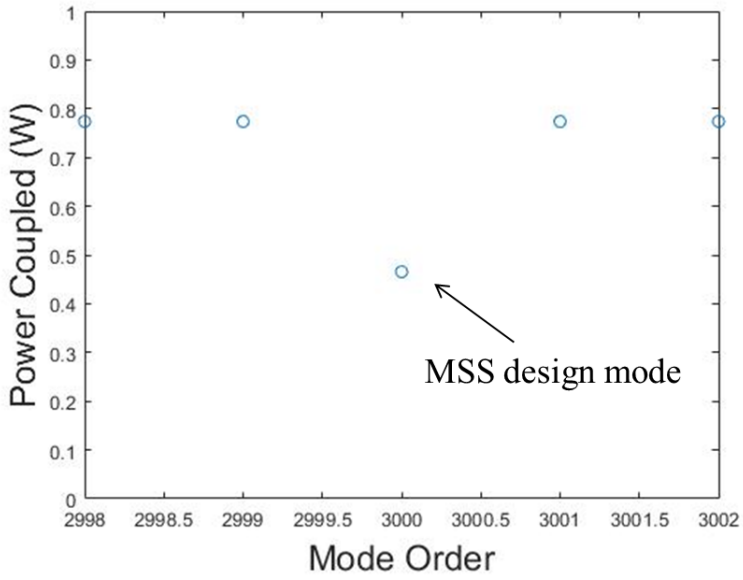

Figure 23: A plot of nearby lasing modes vs. power coupled if the MSS design mode is 3000 and the standing wave in the laser cavity is carrying 2W. Adjacent modes of the design mode immediately increase power coupled by ~0.3W with a MSS coupling distance of 50 nm.

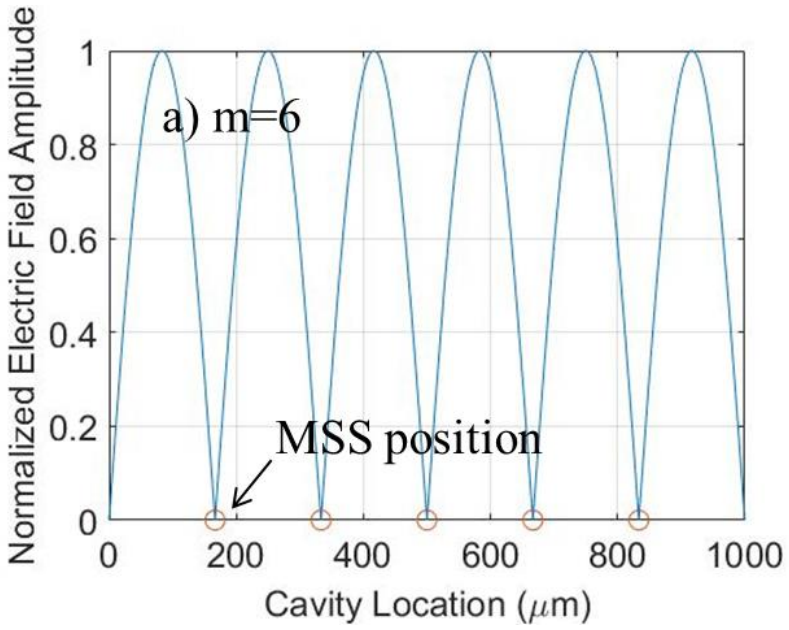

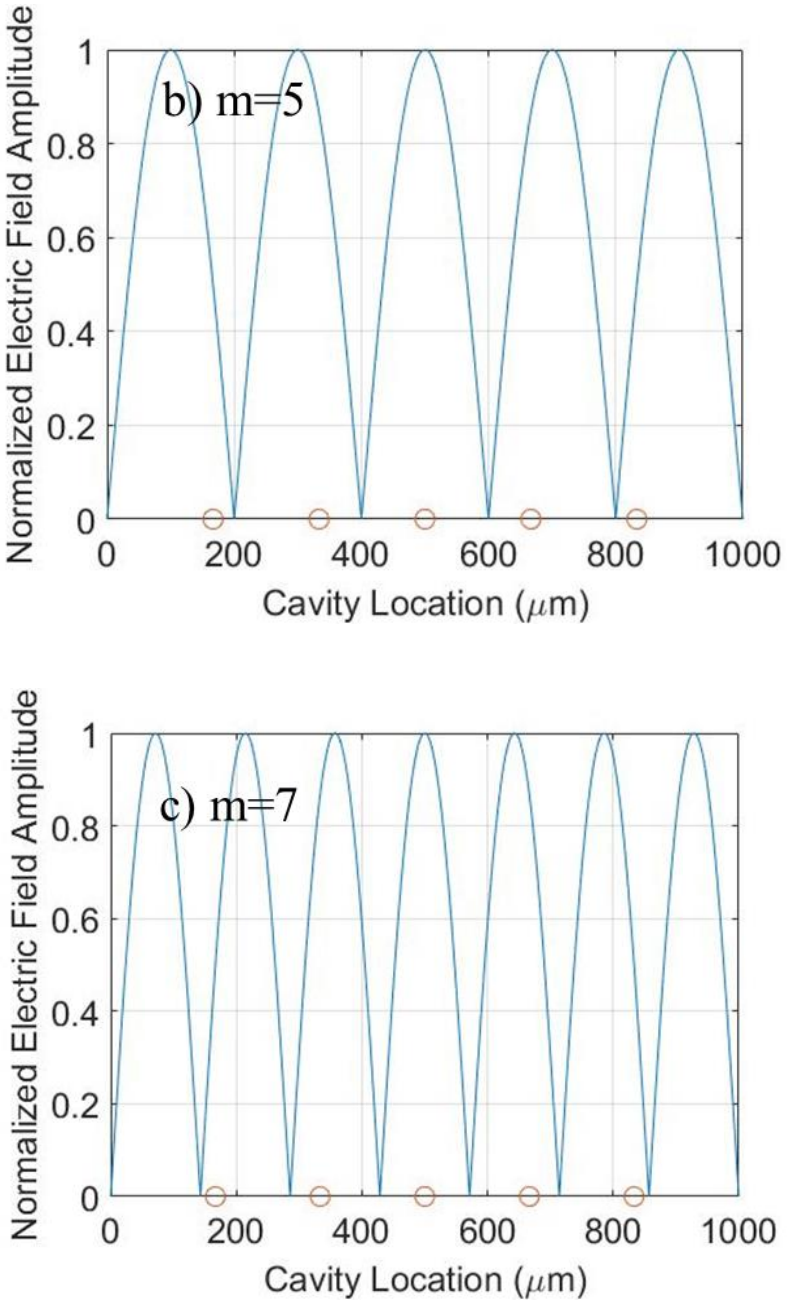

Figure 24: The normalized E field amplitude of a standing wave in a 1000 μm laser cavity is plotted against the positions of the MSS's: a) m=6, the design mode stabilized by MSS, b) m=5, if the laser tries to shift to the next lower mode, and c) m=7 if the laser tries to shift to the next higher mode. The lasing modes of a real laser will be much higher order, and these lower order modes shown are used for explanation purposes.

m	Phase Shift from E field min (radians)				
5	π/6	π/3	π/2	π/3	π/6
6	0	0	0	0	0
7	π/6	π/3	π/2	π/3	π/6

Table 1: Calculated phase shift for each MSS (from left to right in) if the design mode is m=6. The phase shift is reference from the nearest electric field minimum (node) since the coupling interaction is symmetric.

It is not immediately obvious why shifting to an adjacent mode (or modes further away) can have such an impact on the loss, or why the loss remains constant at ~14/cm for the surrounding modes of the design mode. We explain using Figure 24. The E field amplitude of a standing wave in a 1000 μm laser cavity is plotted against the positions of MSS's in an array. The design mode is set at m=6 such that a MSS is aligned to the E field min in (a). When shifting to a lower mode (b) m=5 or higher mode (c) m=7, the phase shifts introduced are identical. These shifts are referenced to the nearest E field min since the coupling interaction of the MSS is symmetric and is shown in Table 1. In our actual laser, the lasing mode will be of a much higher order, but the same principle still applies in that shifting to adjacent modes will introduce the same phase shifts.

In order to maximize the chance of our MSS array stabilizing the laser mode, we want to introduce loss comparable to that found natively in the system but not so much that the laser cannot reach threshold. To begin, we convert the coupling efficiency of a single MSS to an effective loss α in units of 1/cm. We use

$$P = P_0 e^{-\alpha z} \quad (3.1.2)$$

to determine the effective loss, where P/P_0 is the coupling efficiency and z is the length of the cavity. Another way of expressing the conversion is if we launch a wave from one end of the cavity with power P_0, then when it travels distance z only power P will be remaining. If we place a MSS at every node (making a fully dense array) of a standing wave for our design mode, there will be around 3000 total in the array which corresponds to an effective loss of 2/cm. For comparison, the internal loss is roughly 2/cm and mirror loss 12/cm for GaAs surfaces [20]. Since loss introduced by the array of MSS is far from the dominant loss in the system but is still comparable to the internal loss, we expect that aligning one to every node will have a noticeable impact on the laser but should not prevent it from lasing.

3.2 Device Fabrication

We first present the laser structure on which subsequent discussions on mode stabilization will be based on, with a cross section shown in Figure 25 before any processing:

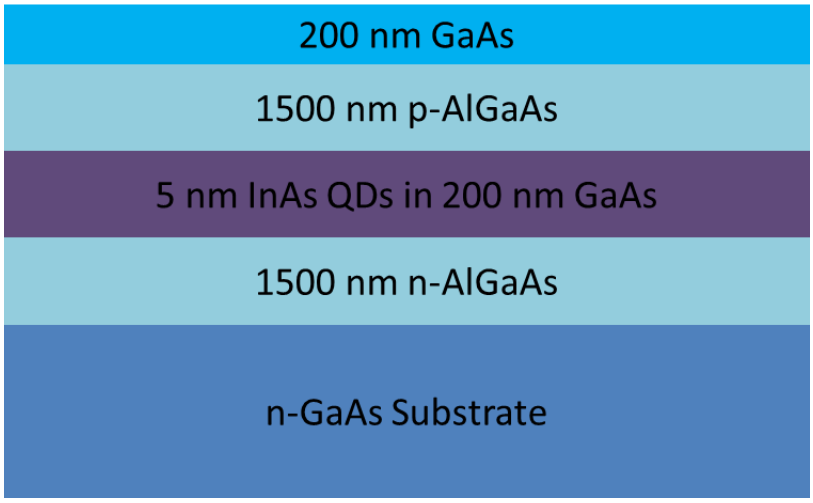

Figure 25: Cross section of our laser structure. InAs quantum dots (QDs) are embedded in the active region made of 200 nm of intrinsic GaAs, sandwiched between 1500 nm of p- and n-type AlGaAs.

Starting sample for our laser consists of 12 layers of 5 nm InAs quantum dots embedded in 200 nm of intrinsic GaAs gain region, with a few nanometers of spacing between each dot. This region is sandwiched between 1500 nm layers of p- and n-type AlGaAs. A 200 nm layer of p-GaAs covers the top p-AlGaAs layer and the entire structure is on n-GaAs substrate.

As the first step, AZ4110 photoresist (PR) is spun at 4000 RPM and exposed in a Karl Suss MA6 contact aligner to define a ridge pattern. The ridge provides additional optical confinement from sidewalls. A tolerance of 1 μm is set on each side of the contacts. The ridge then under goes reactive ion etching (RIE) in a Plasma-Therm Versaline inductively coupled plasma (ICP) system with the PR serving as the etch mask. The ridge height is ~2.3 μm to ensure that the active region is exposed so as to increase light output. Figure 26 shows a scanning electron microscope (SEM) image of ICP RIE:

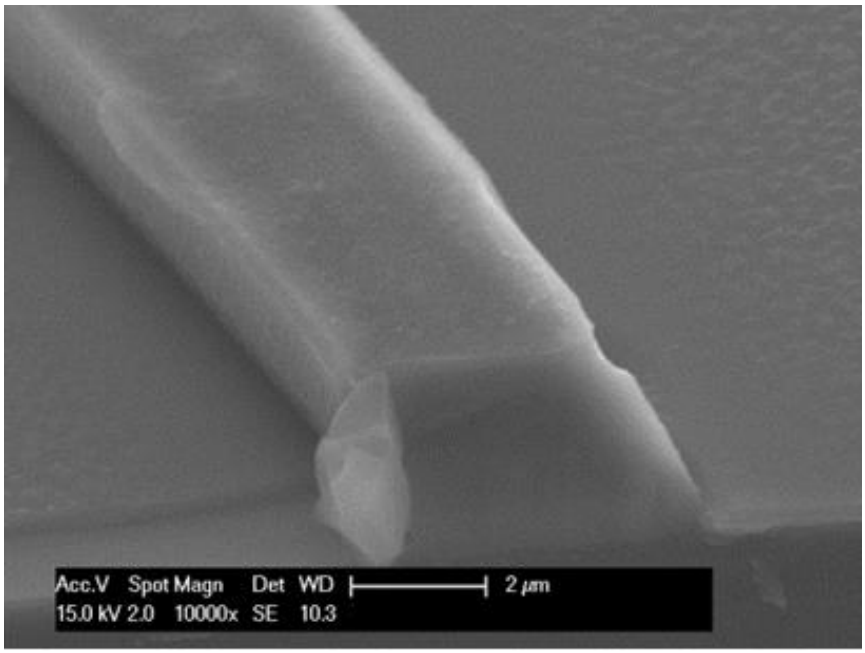

Figure 26: SEM image of GaAs ridge after undergoing chlorine based ICP RIE.

Horst *et al*. showed that the operating characteristics of straight cavity (bar) lasers with ICP etched mirrors are comparable to that of lasers with cleaved mirrors. The slope efficiency, in this case defined as the change in output optical power versus the change in drive current, for lasers with cleaved mirrors was only 10% higher than those with etched mirrors [46].

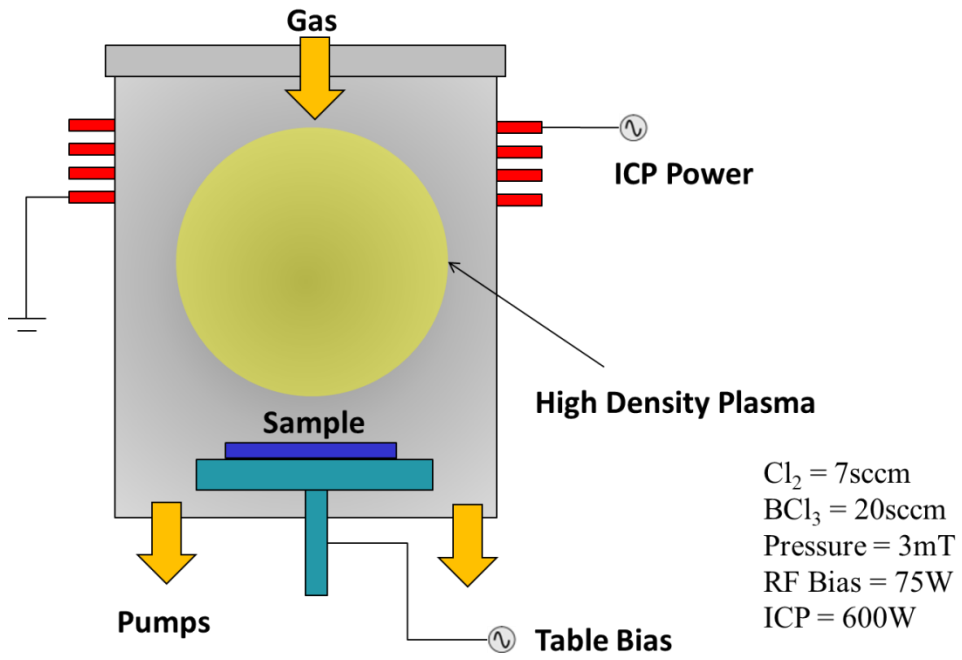

Figure 27: A schematic of our ICP etch system with run time parameters. Etching results from both physical and chemical bombardments.

The ICP system used in this work to etch the ridge sidewalls is similar to the one used in the work of Horst *et al*. A schematic is shown in Figure 27. It includes a 2 MHz ICP power supply and a 13.56 MHz bias power supply. This allows separate control of the plasma density through the top coil (ICP) and table bias through the lower electrode (bias power). When the bias power is applied to the substrate, a DC voltage develops on the substrate surface independent of whether the surface is conductive or not. This enables etching of any material. With the ICP

power determining the ion flux bombarding the sample wafer and bias power affecting the energy and directionality of these ions, one has a high degree of control over the etching process.

In this thesis, the GaAs/AlGaAs sample is secured to a 4" Si wafer using thermal grease and loaded into a Versaline ICP system. Boron trichloride (BCl3) and chlorine (Cl2) are introduced into the chamber at a rate of 20 and 7 sccm respectively. The pump is throttled to maintain a pressure of 3 mTorr. The inductive source power is 600 W and the substrate bias power is 75 W. The sample is etched for 180 seconds to a depth of 2.3 μm, corresponding to an etch rate of 0.77 μm/min for GaAs/AlGaAs. The selectivity to PR is 4 to 1.

After etching the laser ridge, we want to place the MSS array within 50-200nm on the same level as the gain medium to maximize coupling. Challenges arise in both the vertical and horizontal accurate placement of the MSS, as shown in Figure 28 and Figure 29:

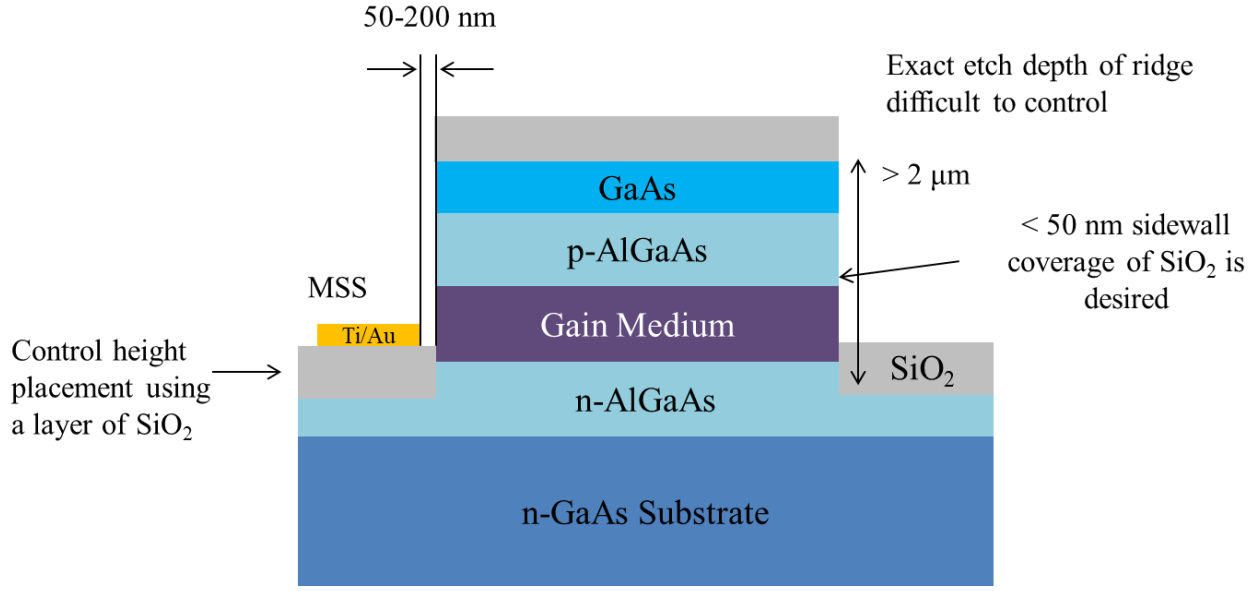

Figure 28: A diagram showing the vertical alignment challenge of placing MSS on same level as gain medium. The main concern is having sidewall coverage which affects coupling distance.

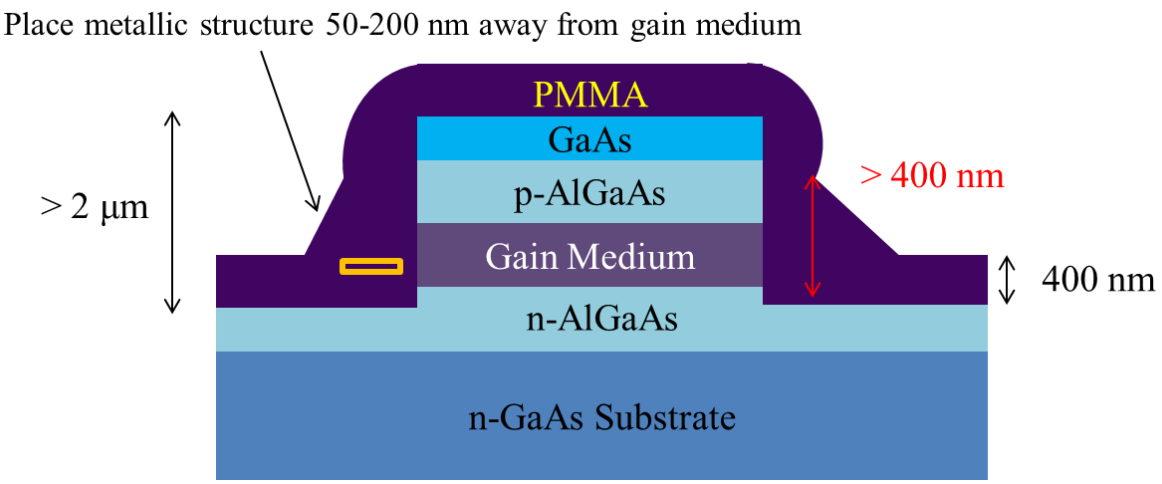

Figure 29: A diagram showing the horizontal alignment challenge of placing MSS near gain medium. Accumulation of thicker resist near bottom corner of ridge may require higher dosage than normal when writing with EBL.

In the vertical direction, we have mentioned that we must etch past the gain medium so that light emission can be observed. In addition, the Versaline can have variations in etch depth of a couple hundred nanometers from run to run. To further complicate matters, whatever method we choose to elevate the MSS must not produce sidewall coverage greater than 50 nm, since that is the minimum coupling distance.

In the horizontal direction, the challenge lies in accumulation of thicker resist near bottom corner of ridge. To define the MSS pattern we must spin resist on the sample, just as we did with the ridge. In this case, the resist used is PMMA. We spin at speeds that nominally give us 400nm in thickness. However, the resist may be much thicker within 50-200 nm of a 2 μm tall ridge. Because of the small size of the MSS, it must be defined using electron beam lithography (EBL). The dosage must be carefully calibrated to ensure the PMMA is properly exposed near the base of the ridge.

To ensure that the MSS be placed on the same level as the gain medium, we adjust its vertical placement using a layer of sputtered SiO_2. We sputter deposit this layer as opposed to using plasma enhanced chemical vapor deposition (PECVD), another common method of SiO_2 deposition, to achieve minimal sidewall coverage. The ratio of top to side coverage is 2:1 and we wet etch away the side coverage using a buffered HF solution. Figure 30a shows a SEM image of the ridge coated with sputtered oxide and (b) shows the same oxide after a 10s dip in buffered HF. In Figure 30c the oxide sidewall coverage is completely eliminated.

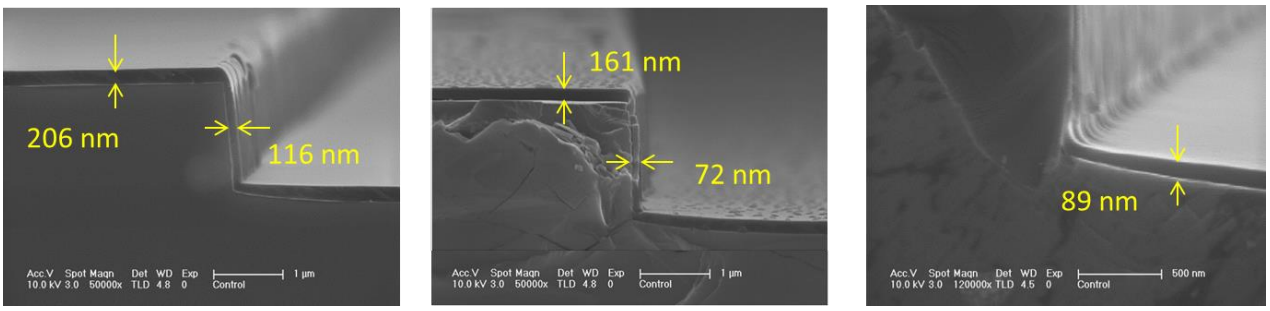

(a) (b) (c)

Figure 30: (a) Sputter deposition of oxide onto a GaAs ridge where there is a ~2:1 ratio of surface to sidewall coverage. (b) The oxide is shown after being dipped into a buffered HF solution for 10s. (c) Enough time has passed while dipped in HF so that sidewall coverage of oxide is eliminated. Nearly 100 nm of oxide still remain on the bottom.

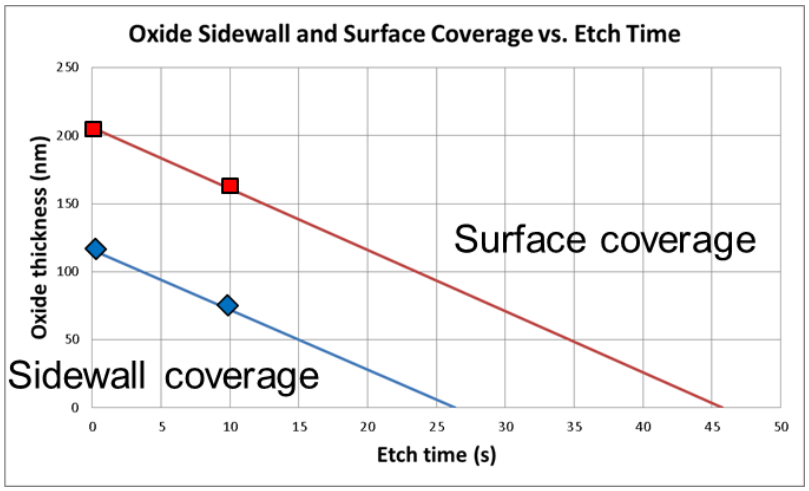

Figure 31: Plot showing oxide thickness vs. etch time. HF etch rate is ~4 nm/s.

Figure 31 plots the HF etch rate of sidewall and surface coverage. After 25s, the sidewall oxide thickness reaches 0 nm while nearly 100 nm still remain on the surface. Thus by etching sputtered oxide with HF, we can fine tune the vertical placement position of MSS.

For accurate horizontal alignment of MSS to laser, we turn to EBL. Its working principle is similar to photolithography except electrons are used instead of photons: a beam of electron is scanned across a substrate covered by an electron-sensitive material, in our case PMMA; the solubility of PMMA is changed by the energy of the beam [71]. Our EBL system is a converted SEM, a FEI Sirion 600, with its vacuum chamber and electron gun. Because it can be operated as a SEM, the beam is raster scanned over the sample in order to collect secondary electrons to form an image. However, since it is not specifically designed for lithography, its performance may be inferior to systems that are. This issue will be discussed further in Section 3.4.

Several factors contribute to the accuracy of the write pattern in EBL. One factor is the write field, which is the largest area exposed without the stage moving. Resolution increases in proportion to decreasing field size. However, a smaller field size may require move stage movement which will introduce errors in position accuracy of subsequent patterns. We choose 100 μm as our write field size and fracture our pattern in the design phase into discrete 100 μm fields. During the ridge etch step, we also etch alignment markers in each of the fields so that during EBL, the stage moves and the SEM aligns the pattern automatically. We use Nano Pattern Generation System (NPGS) as the SEM controlling software. The pattern is first designed in Cadence and then imported to DesignCad, which is fractured by NPGS.

Other factors influencing pattern writing include beam spot size and acceleration voltage, which controls how far electrons penetrate the sample. We use an acceleration voltage of 30 kV

and spot size of 1. A related parameter is the beam current, which defines how many electrons are impinging on the sample each second. A high current electron beam tends to be physically larger than a small current one. At 30 kV and spot size 1 (setting number, not actual size), we measure the beam current to be 23 pA. Once the beam current enters the sample, electrons undergo multiple elastic and inelastic scattering events. As such, the beam deposits a finite amount of energy microns away from its intended spot. This phenomenon is known as the proximity effect, which gives rise to unwanted features post development [71]. In our pattern, the minimum MSS spacing is around 300 nm and we do not observe excessive proximity effect at 30 kV.

Finally we discuss the exposure dosage, which is the amount of energy deposited per unit area in $\mu C/cm^2$. The acceleration voltage and beam current are fixed during a single exposure, and the dwell time of the beam determines the dosage. The correct dosage depends chiefly on the resist used, its thickness, and dimension of pattern being written. For 400 nm PMMA and writing dimensions of 100 to 500 nm, we calibrated the dosage to be 400 $\mu C/cm^2$.

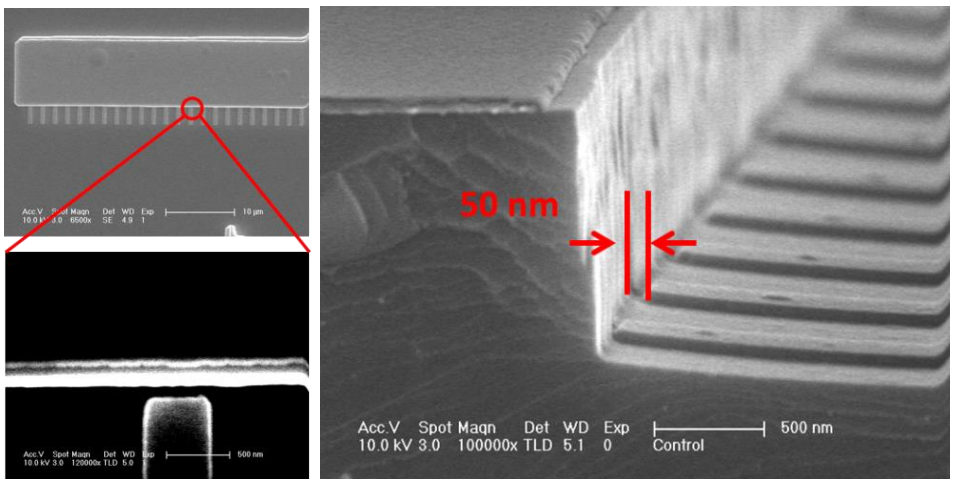

(a) (b)

Figure 32: (a) SEM images of a series of metallic structures made of Ti/Au, first a wide view and then zoomed in from the top, placed within 100nm of a 2μm tall ridge. (b) SEM image of a cross section of the ridge with nearby metallic structures. The coupling gap is about 50nm.

We demonstrate the placement of Ti/Au structures, achieved using electron beam evaporation and subsequent liftoff, within 50-100 nm of a 2 μm tall ridge. In Figure 32a, we show MSS placed in an array within 100 nm of a GaAs ridge viewed from the top. In Figure 32b, we show an MSS array next to a GaAs ridge from the side. With 400 $\mu C/cm^2$ dosage, we observe no problems with pattern writing next to relatively large steps and are able to accurately align MSS to the laser gain medium both in the vertical and horizontal direction.

The next step is to deposit another layer of oxide to cover the entire sample. This layer provides electrical insulation for the contacts as well as optical confinement for the laser cavity. Good electrical insulation only requires the oxide to have a minimum thickness. Optical confinement is more stringent in that we want to choose a thickness such that the oxide will not act as an antireflection coating for the laser end facets. Thus, we first analyze the oxide thickness for optical confinement.

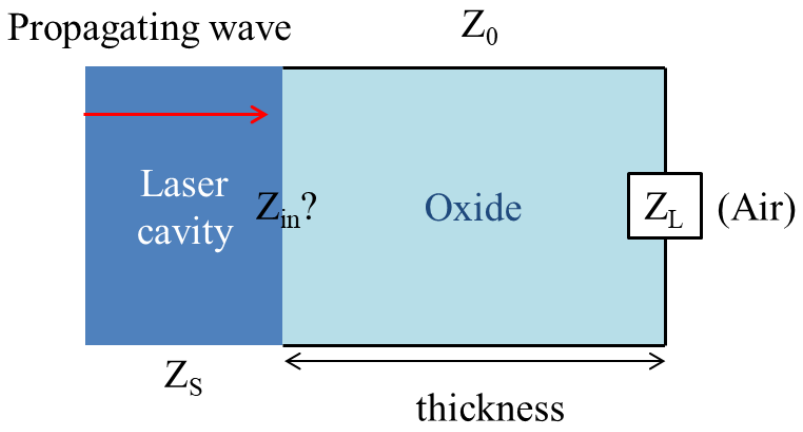

Figure 33: Using a transmission line model, we can calculate the impedance of the oxide, Z_{in}, as seen by a propagating wave in the GaAs gain region of the laser ridge with source impedance Z_S. The oxide by itself has a characteristic impedance of Z_0. The "load", Z_L, of the transmission line is that of air. We can then use this information to determine the reflection coefficient for a certain oxide thickness, which is the equivalent of transmission line length.

To calculate the reflection coefficient, we first model our system similar to that of a transmission line as shown in Figure 33. Three key parameters of a transmission line are its length L, characteristic impedance Z_0, load impedance Z_L, and equivalent input impedance Z_{in}. For our laser, Z_0 is the impedance of the oxide, Z_L is that of air and L is the oxide thickness. We want to calculate the impedance Z_{in} as seen by a propagating wave inside the GaAs gain region of the laser ridge which has a source impedance of Z_s. Using Z_{in} and Z_s we can calculate the reflection coefficient Γ:

$$\Gamma = \frac{Z_{in} - Z_S}{Z_{in} + Z_S} \quad (3.2.1)$$

The impedance Z of a material can be found by:

$$Z = \sqrt{\frac{\mu_r \mu_0}{\varepsilon_r \varepsilon_0}} \quad (3.2.2)$$

where μ_r and ε_r are the relative permeability and permittivity respectively. Note that ε_r is related to the refraction index n by:

$$n = \sqrt{\varepsilon_r} \quad (3.2.3)$$

To calculate input impedance under assumption of no loss in the oxide, we use

$$Z_{in} = Z_0 \frac{Z_L + jZ_0 \tan \beta L}{Z_0 + jZ_L \tan \beta L} \quad (3.2.4)$$

where $\beta = 2\pi/\lambda$ [72]. Note that λ is not the free space wavelength but rather the wavelength inside the material. Now for a given oxide thickness we can calculate its reflection coefficient. However, to get fractional reflection intensity we must square the absolute value of this

coefficient because it represents a fractional amplitude. We show the reflection intensity as a function of oxide thickness in Figure 34:

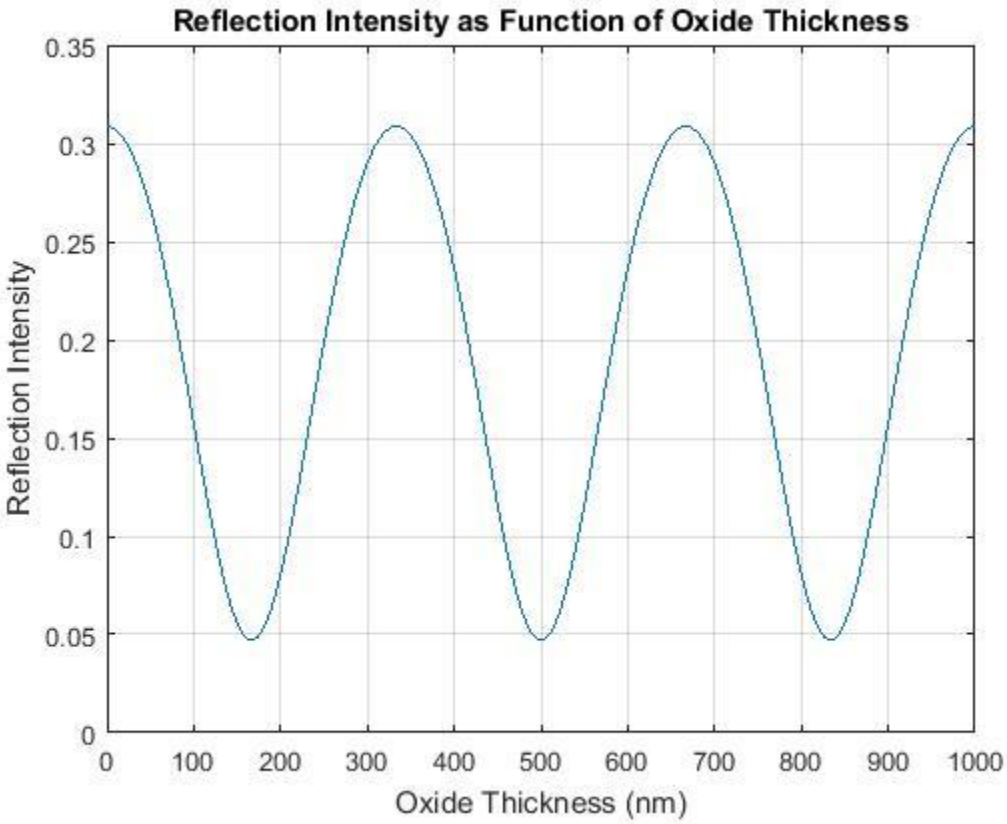

Figure 34: Plot of reflection intensity as function of oxide thickness. We note a maximum of 0.3 reflection intensity and it repeats roughly every 300 nm of oxide.

The maximum reflection intensity calculated is 0.3. We aim for mirror reflectivity of 0.25-0.3. Although this can be achieved within the first 50 nm of oxide, there is danger of incurring significant losses with the metal leads to the probe pads. The next occurrence of maximum reflectivity is between 300-400 nm of oxide. Due to previous experimental evidence for good electrical insulation, we pick the upper bound of this range and use 400 nm as the final thickness.

After the entire sample is covered in PECVD oxide, we etch a via at a rate of 36 nm/min through the oxide using RIE to expose the ridge. We then coat the sample using liftoff resist (LOR) 5B spun at 3000 RPM for 45s and a second layer of AZ4110 PR spun at 4000 RPM for 30s. We deposit Ti/Pt/Au with thickness 5/10/300 nm contacts on the top and bottom of the sample and the combined layers of LOR and PR allow us an easier time to lift off excess metal on top (bottom untouched). After deposition, we first soak the sample in a beaker of Remover PG 1165 for a few hours and use ultrasonic to lift off the excess metal.

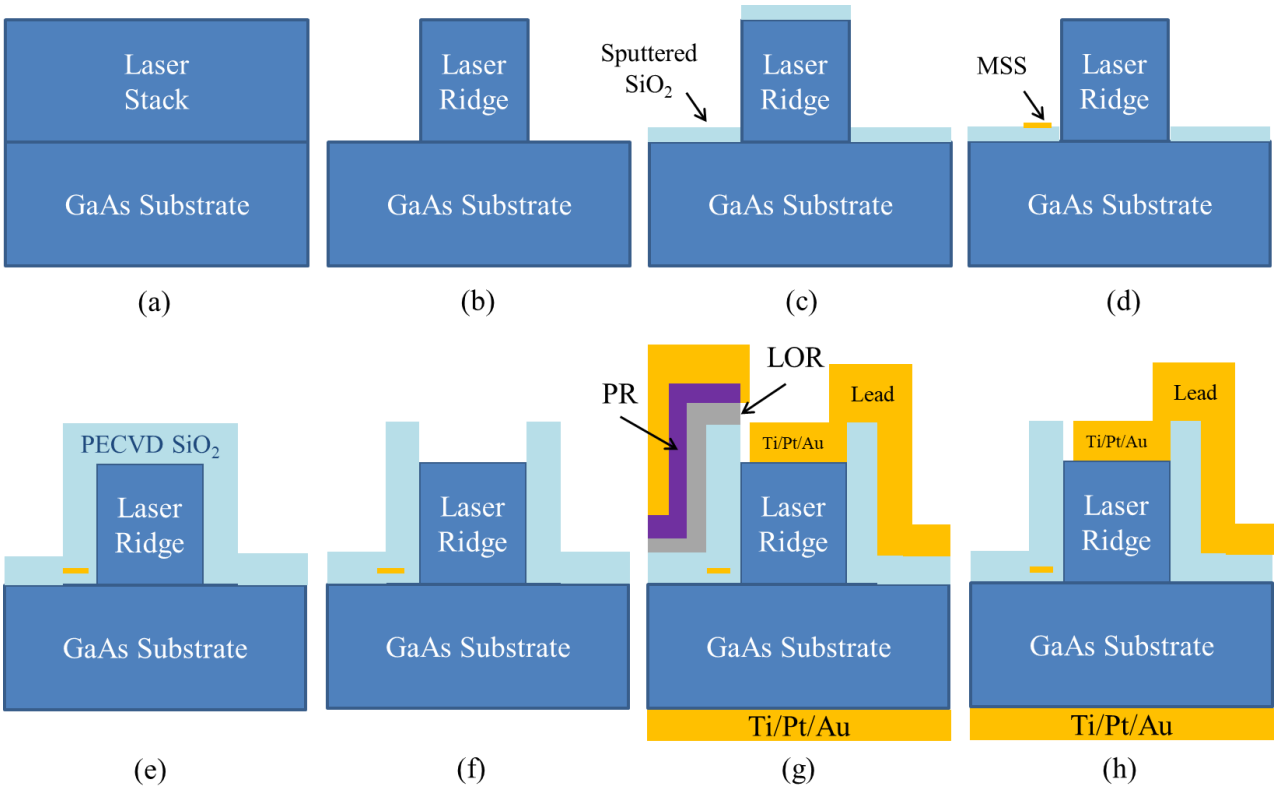

Figure 35: MSS laser process flow: (a) starting sample (b) etch of laser ridge with ICP RIE (c) Deposit sputtered oxide and etch away sidewall coverage with buffered HF (d) Evaporate MSS onto oxide (e) Deposit layer of PECVD oxide, (f) Etch via through oxide to laser ridge using RIE (g) Use layer of LOR and PR for liftoff of Ti/Pt/Au contacts on top (h) Final structure after liftoff with a lead to the probe pad.

The complete process flow is shown in Figure 35, and a completed bar laser device is shown in Figure 36. Due to the small size of the MSS, it is not visible in the Figure 36.

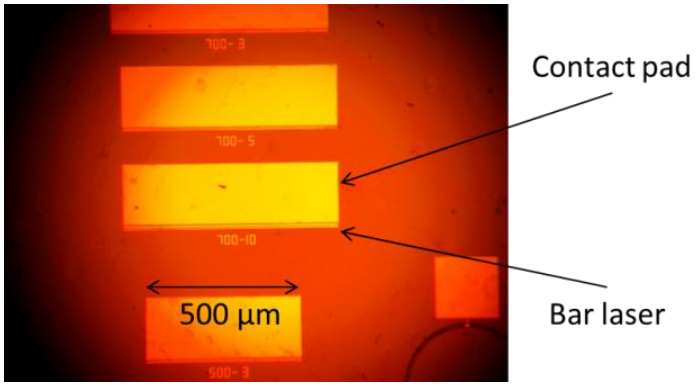

Figure 36: A series of completed bar laser devices shown along with their contact pads.

Note that Figure 36 is a top view of the same structure shown in Figure 35h, which is a cross section side view. We also note here our choice of Ti/Pt/Au as the contact to the n-GaAs substrate. It is normally only used for contact to a p-type material as in that case it can be an extremely low resistance (ohmic) contact [73]. For n-type contacts, other metal stacks can form lower contact resistances than Ti/Pt/Au, and one standard is Ge/Au/Ni [74]. However, our n-side contact is deposited on the entire backside of the chip which as an area of several mm^2, so the contact resistance should be minimized. Thus, we can still use Ti/Pt/Au to make contact with the n-GaAs substrate without a significant rise in contact resistance. This choice also simplifies the fabrication process since we do not have to switch metals for the p- and n-type contacts.

3.3 Laser Behavior Characterization

To characterize the laser operation, we employ an Agilent 33120A Function Generator modulating the voltage of a Newport Model 505B diode laser driver with 20 µs pulses and 100 µs periods. The 20 µs pulse (20% duty cycle) is chosen in an attempt to prevent the laser from

overheating. The driver outputs current at 63 mA/V. Tungsten wire probes connected to the driver makes contact directly to the top electrode and to a metal board attached to the bottom electrode such that the device can be driven in forward bias. A NIRQuest series spectrometer is used to collect light output from the laser, generating a spectrum of the light intensity in photon counts vs. the photon wavelength. We show our setup in Figure 37 and sample spectra in Figure 38.

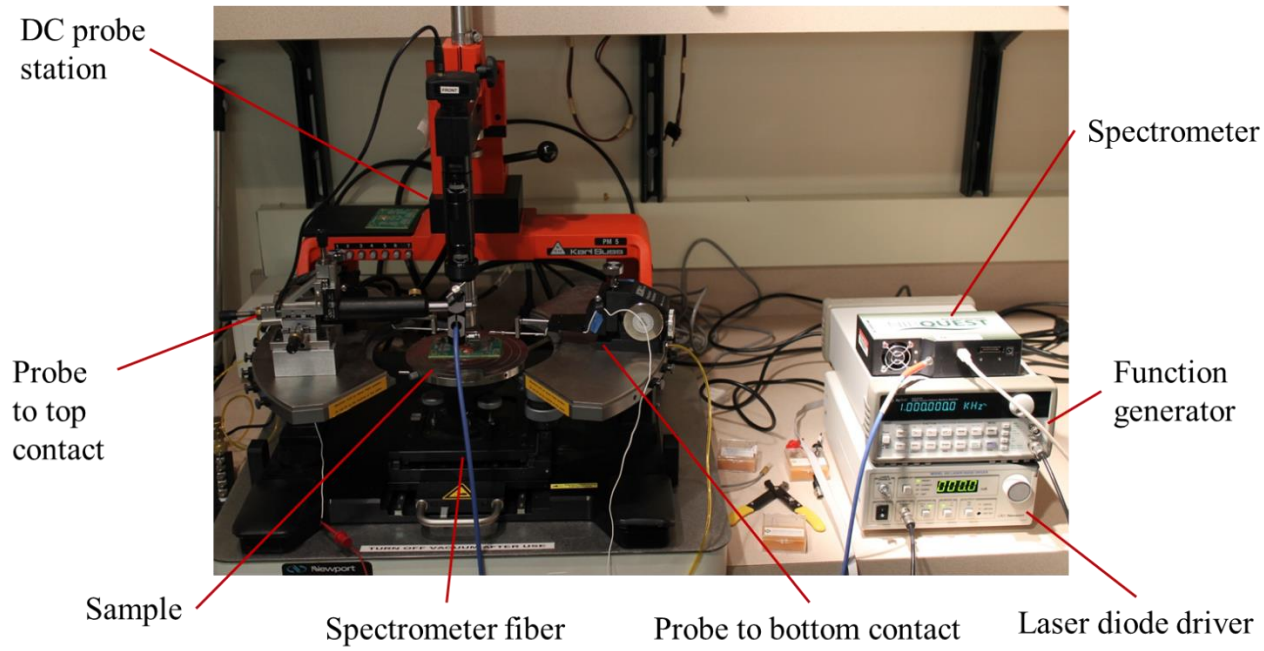

Figure 37: Our laser test setup with a function generator modulating a diode driver and collecting laser output light through a spectrometer fiber. Probes connect to the top and bottom electrodes of our sample, set on a vacuum table of a DC probe station.

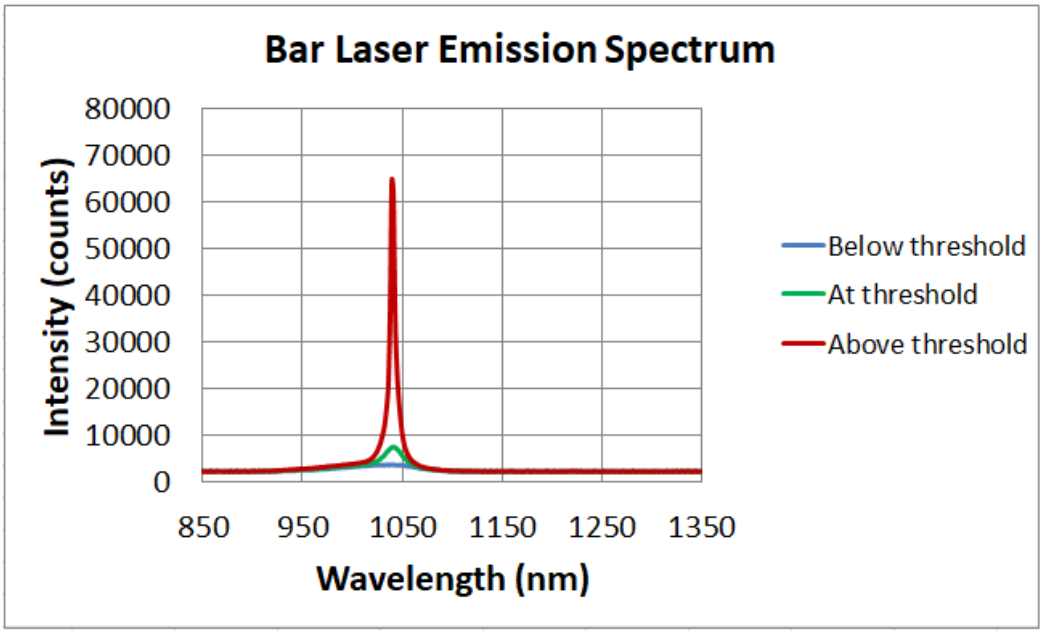

Figure 38: Emission of spectrum of a 1000μm by 5μm bar laser at below threshold, threshold, and above threshold.

The spectra are shown for a 1000 μm by 5 μm bar laser. Below threshold, the spectrum is relatively flat with some electroluminescence mostly due to spontaneous emission in the wavelength range of 1010-1070 nm. At threshold, a small sharp peak begins to form around 1035 nm which is the wavelength favored by stimulated emission. Above threshold, only light at this wavelength gets amplified and in this case achieves a six fold increase in intensity of the peak.

For our mode stabilized lasers, we are interested in the effect of MSS on threshold current and mode operation by varying the coupling distance and number of MSS in the array. We categorize our data in two groups. The first consists of lasers where we stabilize the same mode. We vary the coupling distance and place a MSS at a frequency lower than one aligning to every node of the E field. In the second group, we fix coupling distance and place a MSS at every node while attempting to stabilize different modes. We summarize this data in Table 2 and Table 3.

MSS #	Coupling Distance (nm)	I_{th} (mA)	Lasing Wavelength (nm)
0	N/A	42.91	1034
286	50	43.97	1030
286	100	43.79	1030
286	150	43.79	1030
286	200	43.85	1030
357	50	43.79	1030
357	100	43.85	1030
357	150	43.79	1030
357	200	43.47	1030
571	50	44.23	1030
571	100	44.29	1030
571	150	44.23	1030
571	200	44.10	1030

Table 2: Data for the "fixed mode group." Assuming a mode index of 3.5, a MSS is placed at every 5^{th}, 8^{th}, and 10^{th} node of the E field for a 1000 μm cavity, respectively corresponding to 571, 357, and 286 MSS. A laser with no MSS serves as a reference.

Design Wavelength (nm)	MSS #	I_{th} (mA)	Lasing Wavelength (nm)
N/A	0	44.6	1023
1000	3490	46.62	1007
1005	3473	47.67	1005
1010	3455	46.97	1010
1015	3438	45.84	1015
1020	3422	45.17	1021
1025	3405	45.05	1024
1030	3388	47.38	1005
1035	3372	47.44	1005
1040	3356	47.23	1006

Table 3: Data for lasers with MSS at fixed coupling distance of 50 nm. A MSS is placed at the node of every E field for design wavelengths ranging from 1000-1040 nm at 5 nm increments.

In the fixed mode group, we initially estimate the refraction index of GaAs to be 3.5. Using a 1000 μm cavity, we calculate the wavelength inside the cavity and sum the number of

MSS if one is placed at every 5^{th}, 8^{th}, and 10^{th} node of the E field. For each of these configurations, we vary the MSS coupling distance from 50 to 200 nm.

In the fixed distance group, we pick 50nm as the coupling distance as that is the closest distance we are confident in accurately placing the MSS using our ebeam tool. We attempt to stabilize modes with free space wavelengths ranging from 1000 to 1040 nm at 5nm increments. We place a MSS at every node of the E field. Although the overall number of MSS varies slightly between different design modes, we do not expect this difference to impact the threshold current on any significant scale. We perform a more in depth analysis in the next section.

3.4 MSS Analysis

We begin our analysis by reorganizing the data shown in Table 2 and Table 3. We first plot the number of MSS vs. the threshold current I_{th} for various coupling distances in Figure 39.

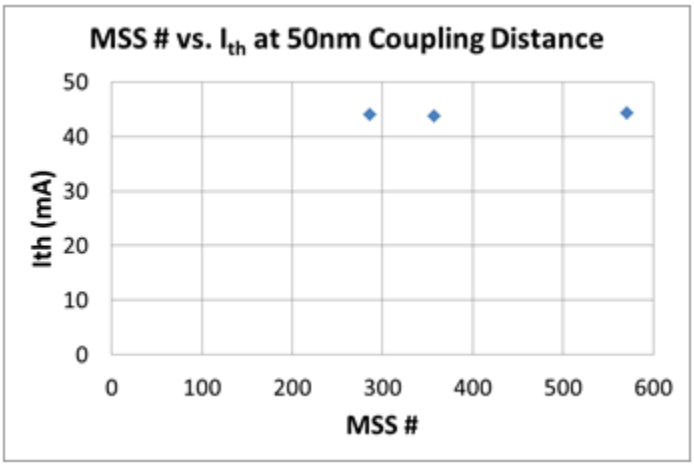

(a)

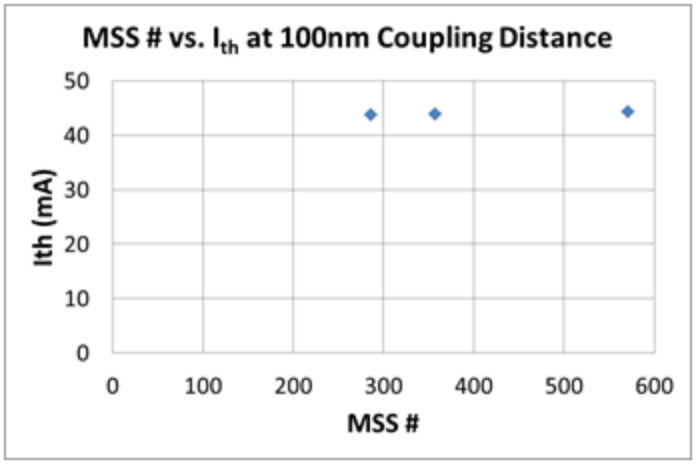
MSS # vs. I_{th} at 100nm Coupling Distance
Ith (mA)
50
40
30
20
10
0
0
100
200
300
400
500
600
MSS #

(b)

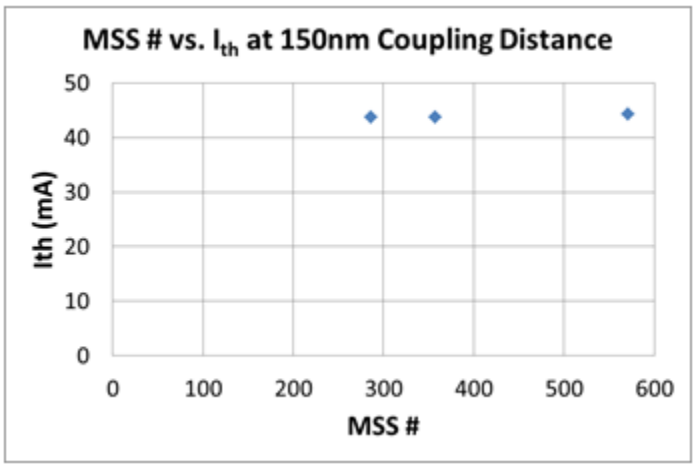
MSS # vs. I_{th} at 150nm Coupling Distance
Ith (mA)
50
40
30
20
10
0
0
100
200
300
400
500
600
MSS #

(c)

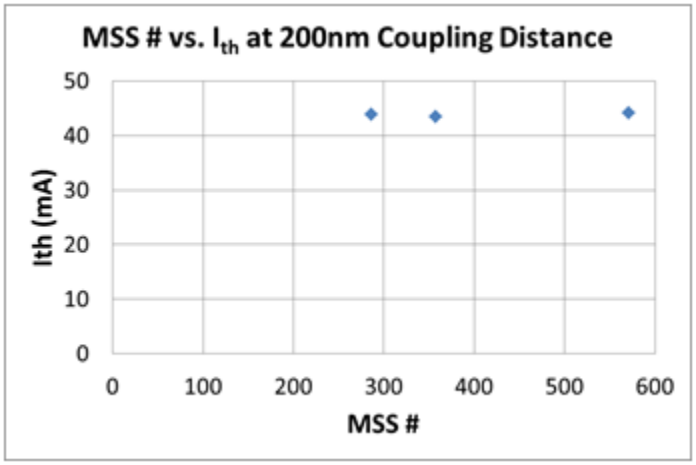
MSS # vs. I_{th} at 200nm Coupling Distance
Ith (mA)
50
40
30
20
10
0
0
100
200
300
400
500
600
MSS #

(d)

Figure 39: MSS # vs. I_{th} at coupling distances (a) 50 nm, (b) 100 nm, (c) 150 nm, and (d) 200 nm.

The coupling distances are 50, 100, 150, and 200 nm and all configurations of MSS in this set are trying to stabilize the same mode. With coupling distance and mode fixed, we examine the effect of MSS number on the threshold current while doing our best to eliminate other factors that can have an impact. We initially expected an increase in threshold current as the number of MSS's increased. This is due to the fact that MSS introduces loss into the system, and the losses in the system must be overcome for a laser to reach threshold. However, we observe no appreciable impact with increase in MSS number at any of the coupling distances 50-200 nm. At first this may appear puzzling but we must examine what is happening inside the laser in the presence of the MSS. Because a MSS will introduce loss into the system, the mode inside the laser will naturally gravitate towards one with the least coupling to MSS. This self-aligning process is a natural mechanism the laser uses to avoid loss. Thus, it is reasonable that when a mode is aligned in this way the MSS will not change the threshold current very much because there is little coupling. It is only when the laser tries to shift to a different mode that loss and thus threshold current will increase.

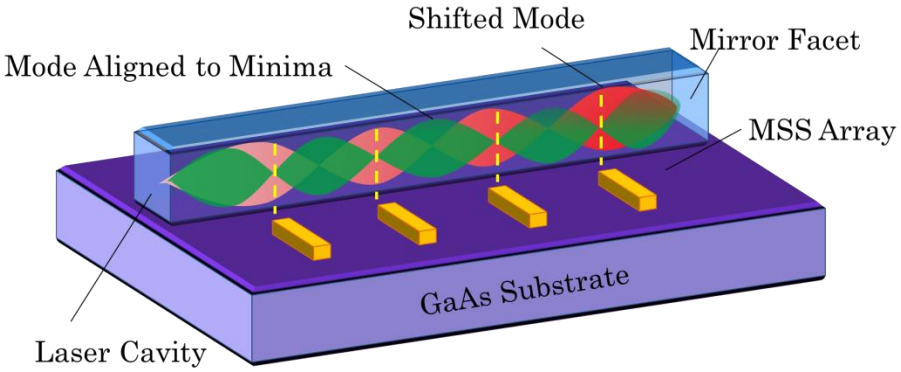

Figure 40: An array of MSS is placed next to the laser cavity. The modes present inside should self-align at the nodes to the MSS for minimum loss.

Figure 40 demonstrates the concept of mode stabilization by using the normal of the E field to represent the mode. The green ovals show the mode's preferred location with the nodes aligned to the MSS while the red ovals represent a shifted mode. The mode originally couples to the MSS at the minimum of the E field. After shifting, it will couple to the MSS at a location with coupling interaction greater than at the minimum. Recall from Figure 23 that any mode shift will incur loss greater than that of coupling to the E field minimum. Coupling at the minimum will have little impact on the threshold current.

We use the same dataset from Table 2 to examine the effect of coupling distance on threshold current. We expect the threshold current to increase as the coupling distance decreases—an increase in coupling strength will increase loss introduced into the system. Again, we do our best to avoid other factors that may impact threshold by only comparing different coupling distances with lasers having the same mode with the same number of MSS in the array.

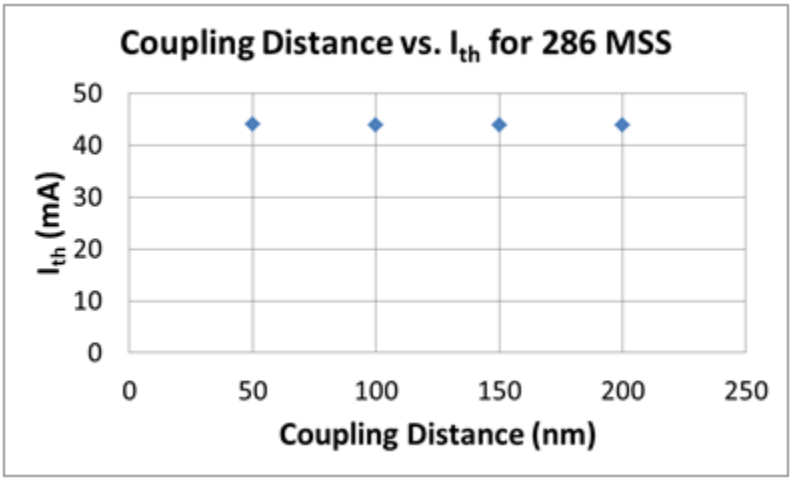

(a)

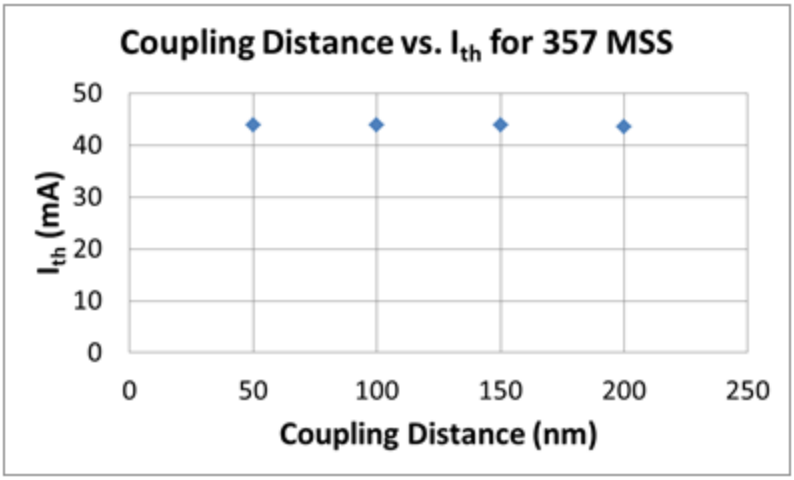

(b)

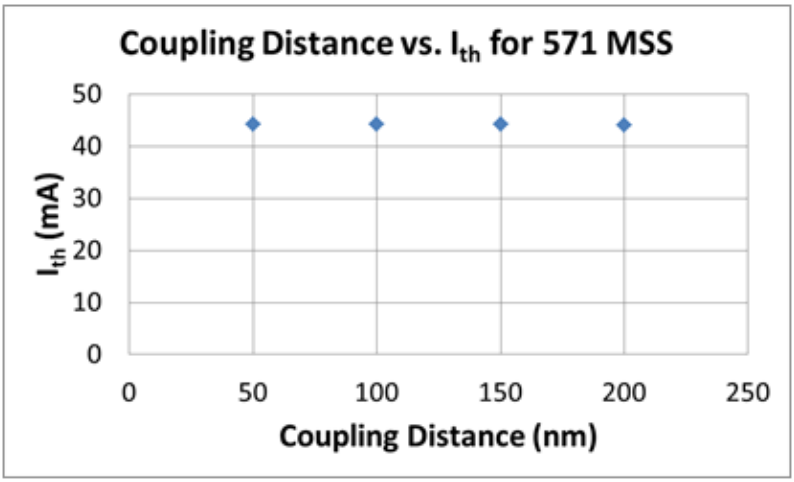

(c)

Figure 41: Coupling distance vs. I_{th} for (a) 286, (b) 357, and (c) 571 MSS.

Figure 41 shows the impact of coupling distance on threshold current for different number of MSS. For 286, 357, and 571 MSS (a MSS placed at every 10^{th}, 8^{th}, and 5^{th} node of the E field respectively), we observe no appreciable change in I_{th} at coupling distances of 50, 100, 150, and 200 nm at the same mode. It is not surprising that a coupling distance of 100-200 nm has little impact on threshold current relative to each other because Figure 21 shows that most of the coupling occurs within 50 nm of the cavity. Although coupling is stronger at 50 nm and we

suspect that threshold current did increase, current increase due to another effect has overshadowed this one.

In order to examine this effect, we turn to the data presented in Table 3 and pay close attention to the lasing mode. We then calculate how far this mode's wavelength is away from the natural lasing wavelength. Figure 42a shows a lasing spectrum for a laser with no MSS. We measure the distance away from the natural mode using the peak lasing wavelength.

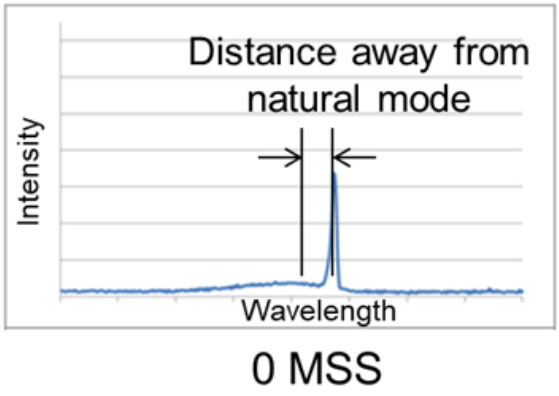

(a)

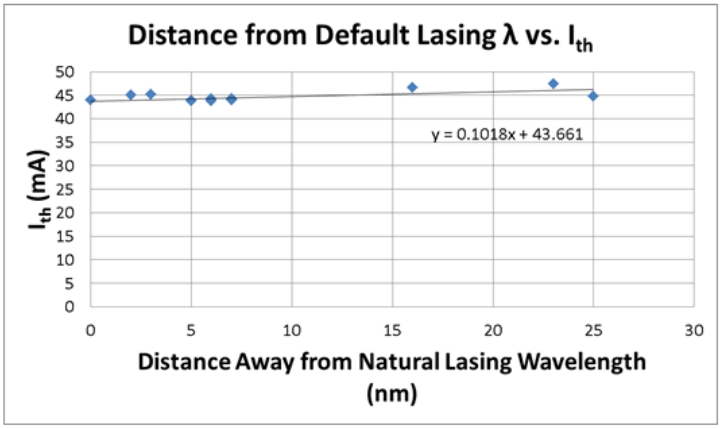

(b)

Figure 42: (a) A visual presentation of how distance from natural lasing mode is defined. (b) A plot of I_{th} as a function of distance away from lasing mode with no MSS. A linear fit is performed.

Figure 42b shows a plot of the threshold current as a function of how far the stabilized mode is away from the natural mode. Note that this mode is the final mode as we observe in our spectrometer, not the mode we originally designed for. We find that the threshold current increases at a rate of approximately 0.15 mA/nm of movement. To explain this increase in threshold current, we initially take a look at what factors in the lasing process depend on wavelength. To reach threshold, the gain must balance the loss in the system. We have discussed that MSS introduces loss. However, data in Table 3 shows two lasers, modes 1025 nm and 1030 nm, have differences of ~2 mA in I_{th} but only 20 in MSS number. That is simply too few to induce the 2 mA change just because of the coupling interaction. We examine other losses in the system which is the internal and mirror loss. Mirror loss depends on cavity length and laser facet reflectivity. The lasers are all the same length at 1000 μm and facets have been etched simultaneously in the same process step, we eliminate mirror loss.

Calculations in literature have suggested that internal loss is likely to be a major limiting factor in short cavity QD structures, and our 1000 μm lasers are at the border of this category [75]. The internal loss α_i can be represented by:

$$\alpha_i = \Gamma\alpha_a + (1 - \Gamma)\alpha_b + \alpha_s + \alpha_c \quad (3.4.1)$$

where α_a is the free carrier absorption loss in the active layer, α_b the free carrier loss in the cladding layers, α_s the scattering loss, α_c the coupling loss, and Γ the optical confinement factor. The variables α_s and α_c can be eliminated for simplicity. Between α_a and α_b, the former generally has greater loss [76]. Free carrier absorption is sometimes called intraband absorption which occurs when a photon gives up its energy to an electron already in the conduction band

[49]. Although this energy is wavelength dependent, an investigation has been carried out which shows that intraband absorption is very weak [77].

What then, can be responsible for the change in threshold current? Before we answer this question, we want to address another related issue. In Table 3, the design modes 1030-1040 nm resulted in actual modes all near 1005 nm. The 25-35 nm mode shift is significant and appears to contradict our predictions that any mode other than the one we stabilized will incur more loss. However, there is an underlying consistency in our data in the form of the mode index (refraction index). Figure 43 shows a plot of the free space wavelength vs. the intended cavity wavelength, or the mode we designed for. This dataset has natural lasing wavelength of 1023 nm, with the lasing spectrum overlaid in dotted lines on the left of the graph. The blue diamond markers represent devices which operate as we intended, outputting a free space wavelength close to our designed cavity mode. We also plot devices which lased in a completely different mode, with their intended lasing modes represented by green triangle markers and actual modes by red square markers. When we fit a line through our data points, the slope of the line represents the mode index which in this case is 3.52. This is reasonable for GaAs in the near-infrared region, which lends consistency and credibility to our data. Some markers are farther from the fitted line than others and this is most likely due to the fact that we did not know the exact mode index of our cavity when we first designed the modes—we assumed an index of 3.5. Regarding the 1030-1040 nm design modes that appeared as 1005 nm modes, the cavity modes are of course different than the ones we intended. Note that these modes fail at wavelengths much greater than 1023 nm.

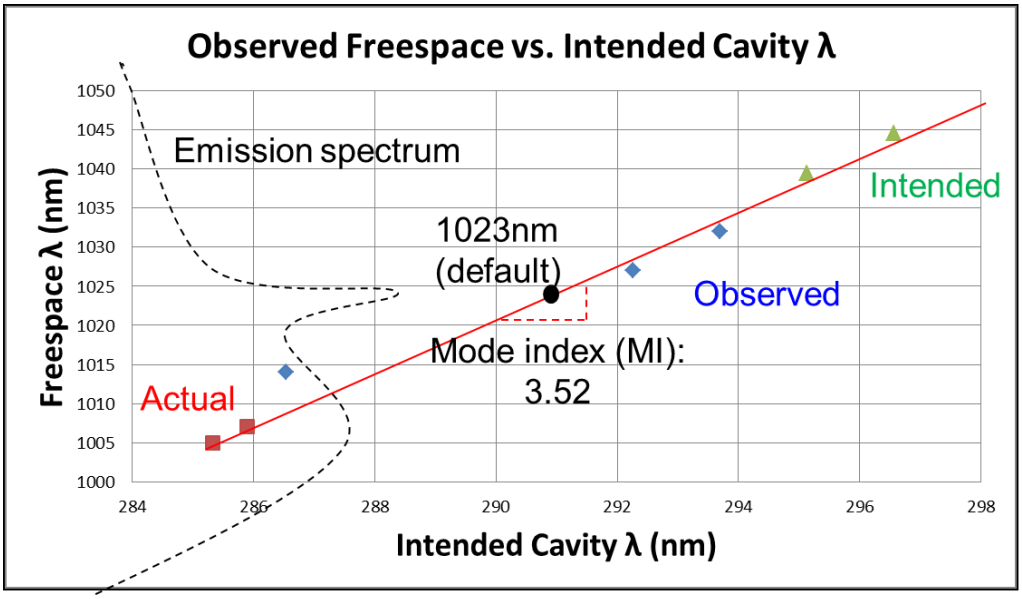

Figure 43: Plot of free space wavelength vs. intended cavity wavelength, with some lasers lasing at modes according to our expectations and others drastically different from expectations. However, the slope of the line fitted through our data points results in a mode index of 3.52, which lends consistency to our data and is realistic for GaAs in the near infrared region. The laser emission spectrum is overlaid on the left in dotted lines.

This fact is important in our upcoming analysis. For now, we summarize the findings of Figure 43 with an observation that trying to shift the mode too far away from the natural mode will result in a different intended mode. We achieve accurate mode stabilization almost 20 nm away from the original lasing mode in the shorter wavelength regime but only a few nanometers in the longer regime.

The issues of why threshold current rises with mode distance away from the natural mode and why sometimes the lasing mode is so much different than the one we designed for can be answered by comparing laser gain vs. loss in the system as shown in Figure 44.

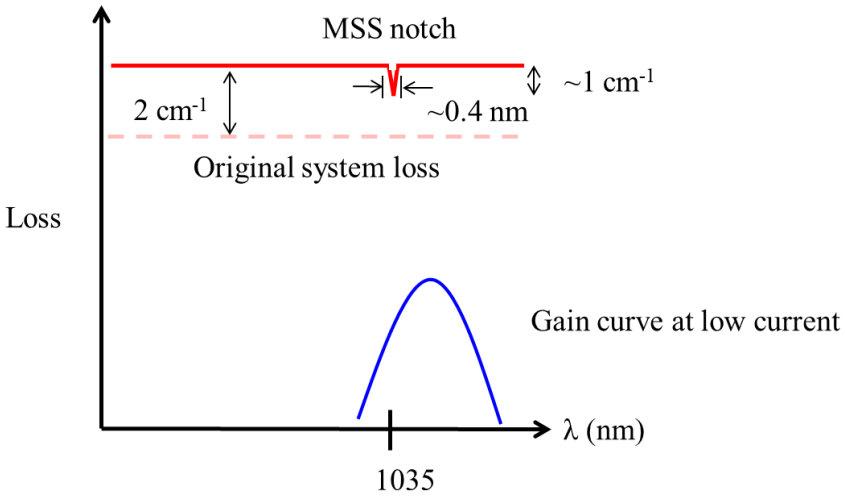

Figure 44: An illustration of gain and loss in the laser vs. wavelength. Gain is represented by the blue curve and is higher at some wavelengths than others. Loss is wavelength independent but the presence of MSS introduces a "notch" in which the design mode (1035 nm in this case) has lower loss than all other modes. Coupling to MSS also increases overall loss. Lasing occurs when gain curve intersects with loss curve.

The gain curve, represented by blue, depends very much on wavelength. Gain is higher at some wavelengths than others. It also depends on current because electrical pumping is the source of excitation for stimulated emission in our laser and greater stimulated emission leads to greater gain. We know from literature that the gain curve grows, shifts, and widens with current [78] [79].

The loss curve, on the other hand, does not normally depend on wavelength. Therefore, it is a straight line on a plot of loss vs. wavelength. However, the presence of the MSS creates a "notch" in this line because it causes one mode, our design mode, to be favored over others. The method by which this mode is favored is that it has lower loss. In Figure 44, loss is represented by a red line with a notch at 1035 nm, which is the example design mode in this case. We estimate the original loss to be 12/cm, taking into account the internal and the mirror loss. Based on our simulation results shown in Figure 22 for 50 nm coupling distance, we calculate that a

MSS placed at every node of the E field will raise overall loss by ~2/cm. Figure 24 gives an estimation of the relative losses of the design mode compared to other modes. The notch is found to be ~0.4 nm in width and ~1/cm in depth.

The width and depth of this notch can be further fine-tuned. The width is directly proportional to mode spacing, and it can be shown that this spacing can be increased by decreasing the cavity length L:

$$1 = 2L(\frac{\lambda_m - \lambda_{m+1}}{\lambda_{m+1}\lambda_m}) \quad (3.4.2)$$

where λ_m and λ_{m+1} are the wavelengths of adjacent modes. The notch depth can be increased if the coupling interaction to a MSS can be increased. This can be achieved by using a wider MSS, bringing the array closer than 50 nm to the laser cavity, and making the gain medium have higher index contrast than the cladding. We explore this last point in more detail in Section 5.1, but for now we mention that higher index contrast produces a better confined mode which increases the coupling strength to the MSS.

Lasing occurs when the gain balances the losses in the system, which means the gain curve intersecting with the loss curve. Normally, a laser reaches threshold at the peak of the gain curve because as the gain grows with current, the peak will be the first place to intersect the line that represents loss. The presence of the MSS raises overall loss but decreases loss for the mode designed to be stabilized. In theory, the peak of the gain curve should intersect with loss at the MSS notch so that the laser lases at that wavelength. However, the gain curve has a tendency to shift to lower wavelengths with increasing current [78] [79]. If the gain curve misses intersecting with the notch while shifting, the lasing mode that appears can be drastically different than the mode we intended.

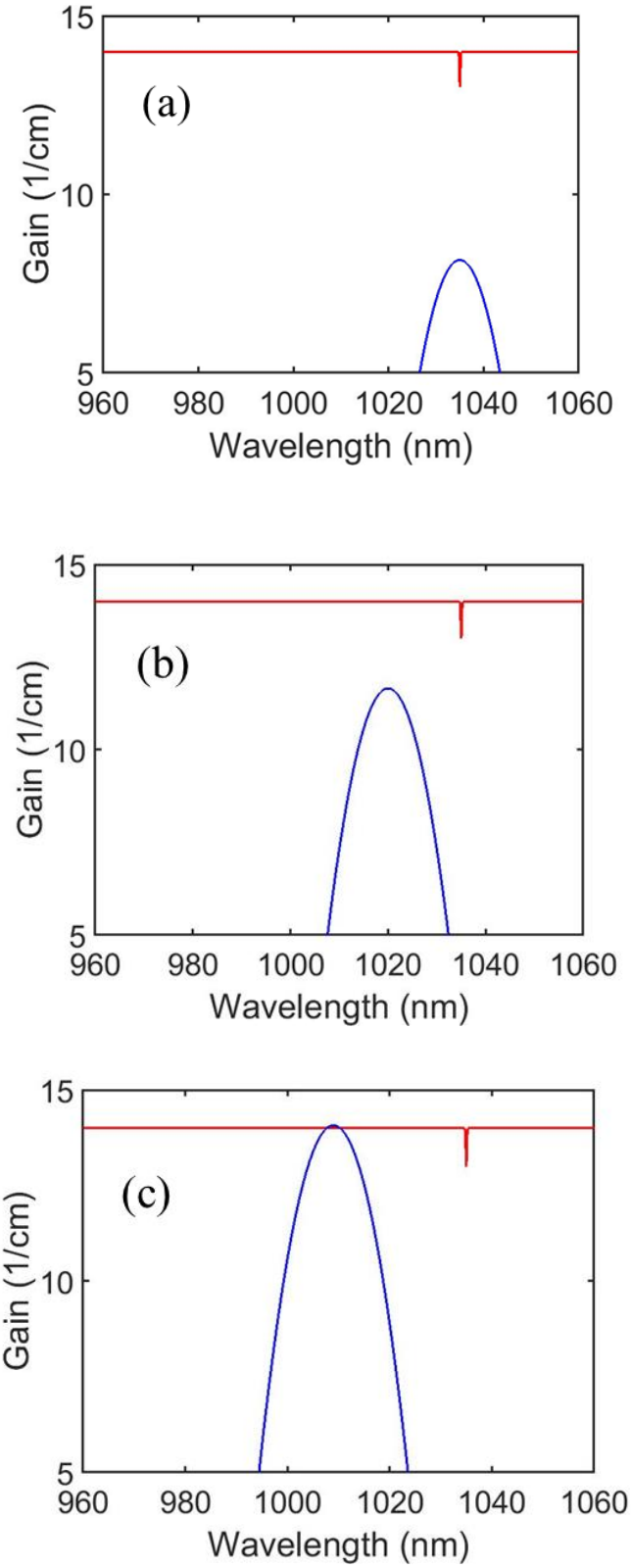

Figure 45: Gain (red) and loss (blue) curves for 1035 nm design mode at different drive currents: (a) 41 mA, (b) 44 mA, and (c) 47 mA. Lasing occurs when the two curves intersect as shown in (c), at 1005 nm.

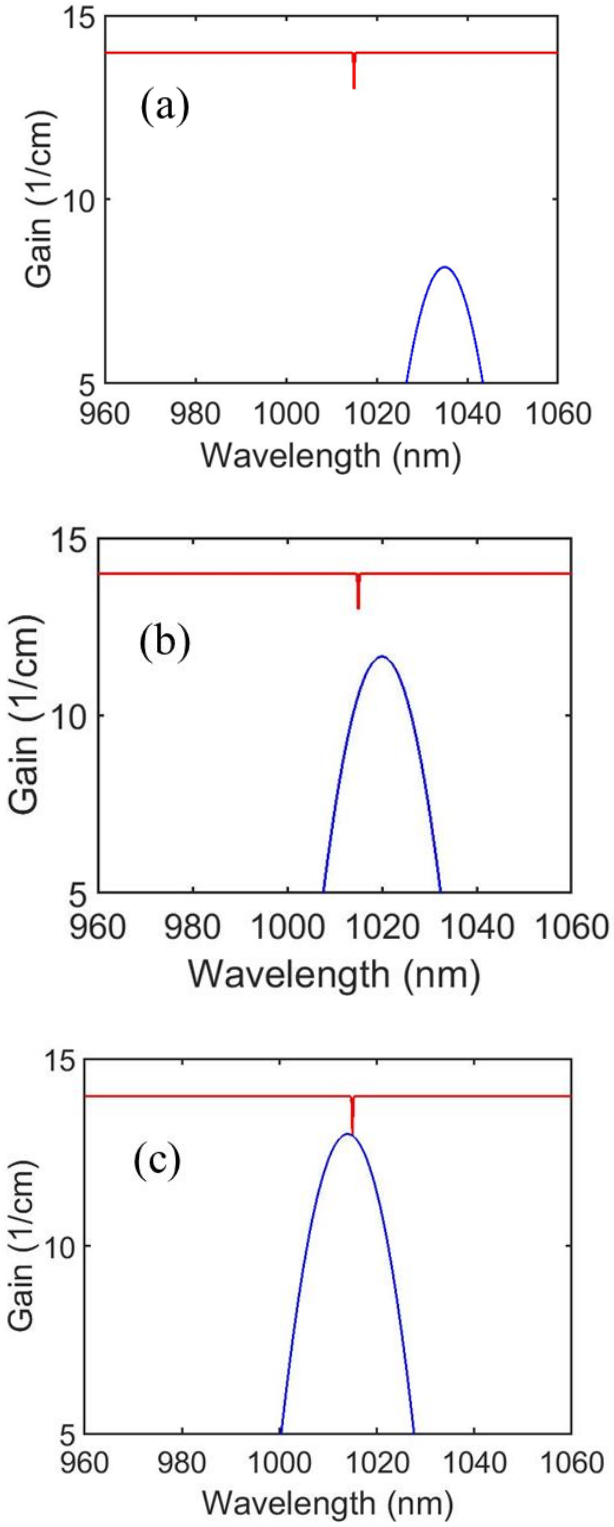

Figure 46: Gain (red) and loss (blue) curves for 1015 nm design mode at different drive currents: (a) 41 mA, (b) 44 mA, and (c) 45 mA. Gain intersects with loss at notch, outputting at the design wavelength.

Figure 45 and Figure 46 explain why some modes can be successfully stabilized while others cannot. We first construct the gain curves based parameters found in literature [78] [79]. It is known that the gain curve grows in height and widens in proportion to the natural log of current. Thus, the equations used to model gain growth take the form A*ln(I) + B where I is the current and A and B are constants:

$$Height: 53.7 \cdot \ln(I) - 53.7 \quad (3.4.3)$$

$$Width: 221 \cdot \ln(I) - 347 \quad (3.4.4)$$

The gain curve is approximated by a Gaussian function in MATLAB and changes as a function of current in accordance with the above mentioned rates. The initial starting size of the gain curve is similar to ones found in the [78] and [79]. However, we picked the initial starting position so that the gain curve will intersect with loss at 12/cm, with 44mA current and 1023 nm wavelength. The value of the peak gain is as follows:

$$Peak\ gain: 49.5 \cdot \ln(I) - 176 \quad (3.4.5)$$

Recall that 12/cm is the original loss in the system without MSS and 44 mA is approximately the lasing threshold of a laser by itself in Table 3. This way, theory can more closely match with our experimental results.

We compare 2 modes which the MSS array has been designed to stabilize, 1035 nm and 1015 nm, and examine why stabilization for the former fails but the latter succeeds. Starting at 41 mA, we continue increasing the current until the device reaches threshold. The gain curve is identical for the 2 devices and only the placement of the MSS notch in the loss curve changes with overall loss increasing by 2/cm from original loss for both. Although the 1015nm mode

technically has more MSS at 3438 compared to 1035 nm mode's 3372 MSS, the difference this makes in the overall loss is negligible.

Figure 45 shows the gain and loss curves for the 1035 nm mode. At 44 mA, the gain does not intersect the loss so the laser does not lase at the wavelength it otherwise would have. However, it is clear at this point that the gain has shifted too much and no growth can allow it to intersect with the MSS notch at 1035 nm. Therefore, it keeps shifting and growing until intersecting with loss at 1005 nm which occurs at 47 mA.

Figure 46 shows the gain curve and loss curves for the 1015 nm mode. At 44 mA, there is no lasing but the gain curve has not moved past the MSS notch as it did for the 1035 nm mode at this current level. We keep increasing the current until the growth of the gain curve allows for intersection with loss. This occurs at 45 mA. Because the gain curve intersects with the loss at the MSS notch, the laser is able to output at wavelength we design for.

We include here a brief discussion of how temperature may affect our mode stabilization scheme. The gain curve plotted above already takes into account the temperature rise due to the pump current. However, the initial temperature is assumed to be room temperature (20℃) and a HDD may operate in a range of temperatures. For example, HDDs from Seagate Technology are advertised to be able to operate between 5-50℃ [80]. According to [78], the threshold current of a laser increases at about 0.27 mA/℃ and our room temperature threshold current is 44 mA. The threshold current without MSS is then predicted to be 40 mA at 5℃ and 52 mA at 50℃. We construct plots of loss and gain for our successfully stabilized 1015 nm mode at 5℃ and 50℃ and show them in Figure 47. The loss curves have been adjusted to reflect the lasing conditions

of each temperature. We will show in Section 4.1 how increasing the temperature increases loss for the laser.

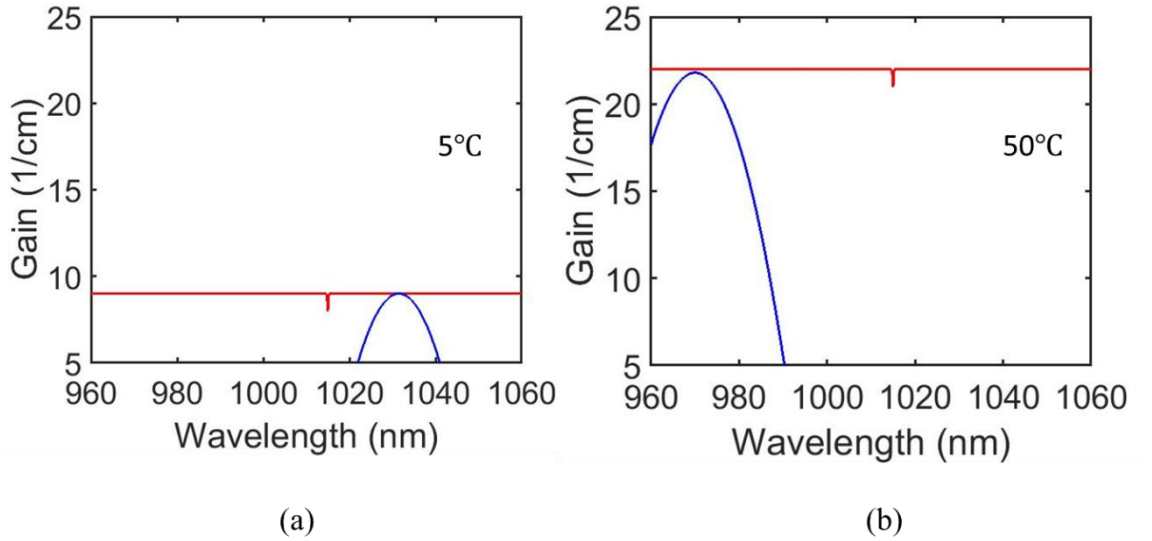

Figure 47: For the 1015 nm mode, plots of gain and loss are shown for initial temperatures of (a) 5℃ and (b) 50℃.

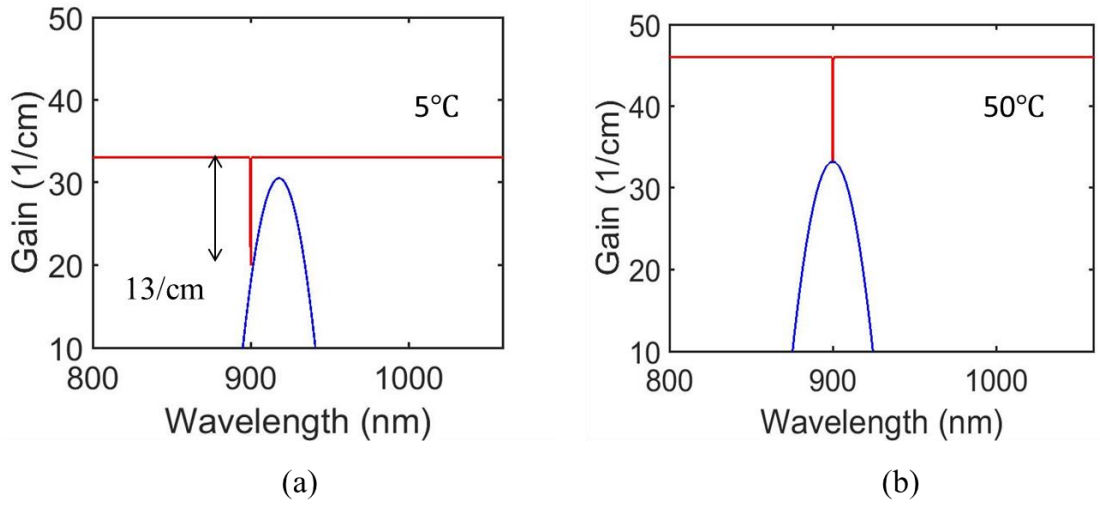

Figure 48: Example of MSS setup such that the laser mode (900 nm) can still be stabilized at (a) 5℃ and (b) 50℃. The depth of the notch curve has increased to 13/cm. The lasing wavelength is most likely unfeasible due to our spontaneous emission curve having a range of $\pm\mathbf{60}$ nm centered on 1000 nm.

At the HDD operating temperature extremes, the laser does not lase at the design mode of 1015 nm due to either the gain curve prematurely intersecting the loss curve at low temperature and overshooting the notch at high temperature. Using the same plotting methods, we find that the tolerance for the gain curve to intersect the MSS notch for the 1015 nm mode is only $\pm 5℃$. This does not fit the HDD's operating specs, and we show what it would take for our MSS laser to operate at 5℃ and 50℃ in Figure 48. We increase the depth of the notch to 13/cm which is more than an order of magnitude compared to our original 1/cm. Increasing the coupling strength to such a degree is challenging, but the working wavelength has changed to 900 nm which makes this scenario likely to be impossible. This is due to our laser's spontaneous emission curve having a range of ±60 nm centered on 1000 nm.

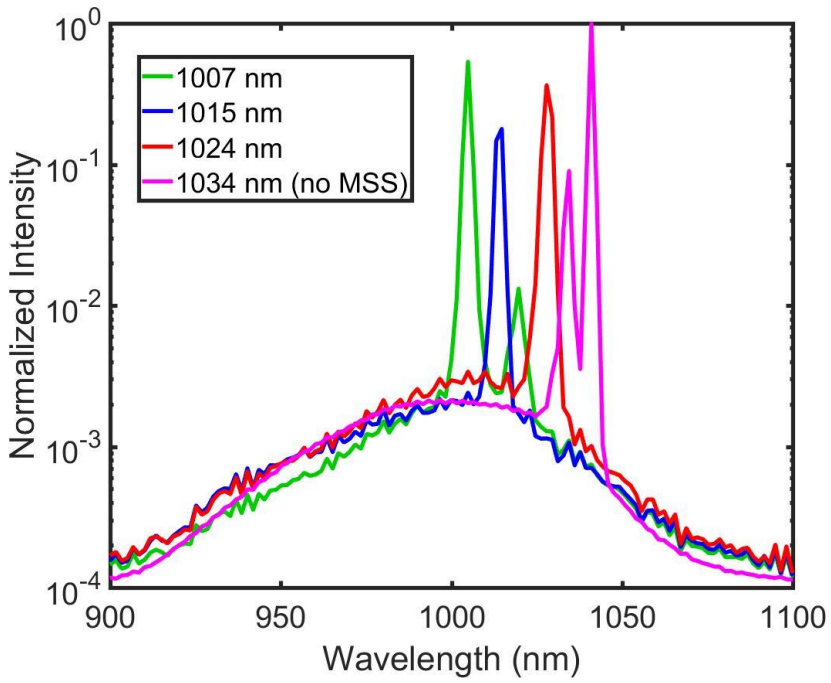

Figure 49: Comparison of emission spectra for laser with no MSS (default) and with MSS for modes 1007 nm, 1015 nm, and 1024 nm. Note the secondary peak that appears for the default laser but is eliminated for lasers with MSS. We achieve a minimum SMSR of 20 dB.

Returning to our working conditions at room temperature, although some of the modes do not lase at the wavelengths we stabilized for, nearly all lasers with MSS have eliminated the appearance of secondary modes. Recall that secondary modes are undesirable during lasing because it opens the door to mode hopping, or switching between different modes. This switching can cause fluctuations in power and leads to data being written unreliably in HAMR. Figure 49 compares the emission spectrum of various lasers. One laser without MSS lases at 1034 nm, and its emission spectrum is represented in purple. Note that there are two peaks instead of one, indicating the presence of a secondary mode. However, the rest of the spectra shown are for lasers with MSS stabilizing a particular mode. We achieve a minimum side mode suppression ratio (SMSR) of ~20 dB. Although thus is comparable with the parity time symmetry configuration of the ring resonators in [29], a SMSR of > 50 dB is considered suitable for single longitudinal mode operation of diode lasers [81].

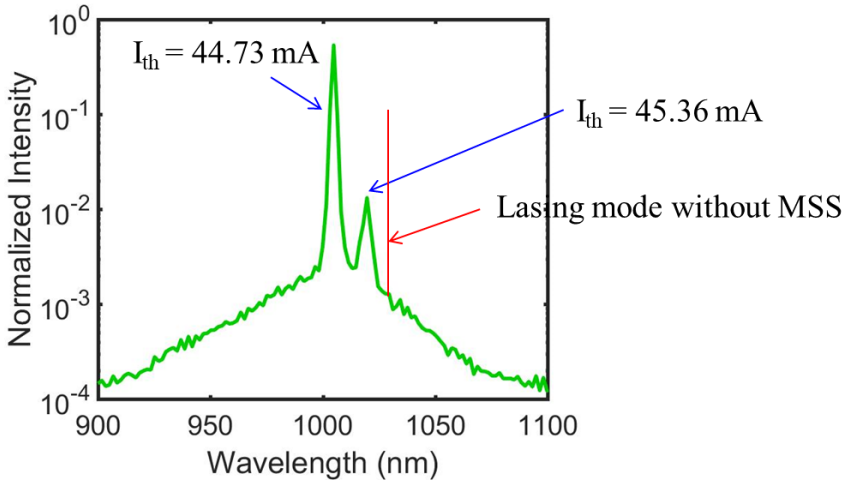

Figure 50: Emission spectrum for the 1007 nm mode. The lasing modes are labelled with the threshold current at which they first appeared. Although this laser has its mode stabilized by MSS, a secondary mode still appears at higher drive current. We speculate the gain for the first mode may have overcome that of the second, allowing it to lase.

Figure 50 shows the emission spectrum just for the intended 1007 nm mode and the threshold currents at which they appeared. The first mode lases at 44.7 mA while the second lases at 45.4 mA. The higher drive current indicates that the second mode is more lossy, requiring more gain. We speculate that as the current increases, the laser gain that balances the losses for the first mode grows such that it also balances losses for the second mode. We observe this secondary mode lases at a location close to the original lasing mode without MSS. Further studies are needed to explain this phenomenon.

3.5 Conclusion

In this chapter we demonstrate that laser mode stability may be achieved by introducing external periodic loss via an array of mode stabilizing structures (MSS) placed near the gain medium of the laser. We have devised special techniques during fabrication to accurately align the MSS with the gain medium. We examine the effect of MSS number on threshold current while holding the coupling distance and the mode being stabilized constant. We do not observe a meaningful impact on the threshold current. This is reasonable given that the MSS are aligned to the minima of the E field in the cavity which are also places having the lowest coupling interaction. We also do not observe an impact on the threshold current from variation in coupling distance 50-200 nm. Our explanation is that current increase due to mode shifting has overshadowed any observable effects relating to the coupling distance. Based on parameters extracted from literature [78] [79], we construct gain and loss curves to demonstrate why we are able to stabilize some modes but not others. We achieve a SMSR of 20 dB due to the relatively weak interaction of the MSS, so it is not as strong as the standard SMSR of 50 dB for single mode operation. However, our process of mode stabilization avoids the complex layer regrowth

methods used by DFB and DBR lasers and serves as a platform for additional monolithic integration, which we demonstrate with the waveguide-resonator-NFT system in Chapter 5.

Chapter 4: Laser Optimization

After achieving a mode stabilized laser, we explore laser optimization in the areas of device geometry and heat sinking. Optimization in these areas should improve laser performance such that it can serve as a stable light source for our high efficiency NFT coupling system. In device geometry, we compare the standard 'bar' laser against the 'ring' laser in terms of threshold current density J_{th}, with a lower J_{th} signifying less device heating. Any heat that is produced can be alleviated with proper heat sinking of the laser. Given the fact that our current laser can only operate under pulsed conditions, our goal is to decrease device heat generation and increase its dissipation using proper heat sinking such that the laser will operate in continuous-wave (CW) mode. CW operation will make our laser more suitable for use in HAMR.

4.1 Ring vs. Bar Lasers

In Chapter 3 we stabilized the mode of a bar-shaped laser, but in reality the same method of using a periodic array of metallic nanostructures to affect laser mode operation can be applied to any geometry. In HAMR, primary motivations for exploring other geometries include lessening heat generation and minimizing device dimensions due to space constraints. Traditionally, the HAMR light delivery system uses an edge emitting laser on top of the slider where it is actively aligned to a coupling structure [8]. Figure 1 from Section 1.2 shows that our laser will be instead mounted onto the backside of a slider, and this area for commercially available 'femto' sliders is in the range of 700-800 μm^2 [82]. This means that any laser used for HAMR light delivery as envisions in this thesis must be able to fit into this area. Limiting the length of bar lasers may cause a rise in J_{th} and overall local heating due to smaller device size. Ring lasers, on the other hand, offer longer path length in the same area of space. However, a

potential downside is that ring lasers introduce bending loss which raises threshold current. In this section we perform a comparison of the 2 geometries in terms of J_{th} to determine which one experiences less local heating.

Both ring and bar laser in this study have the same structure and have been patterned simultaneously using the fabrication steps described in Section 3.2 excluding the placement of MSS. Figure 51 shows a cross section.

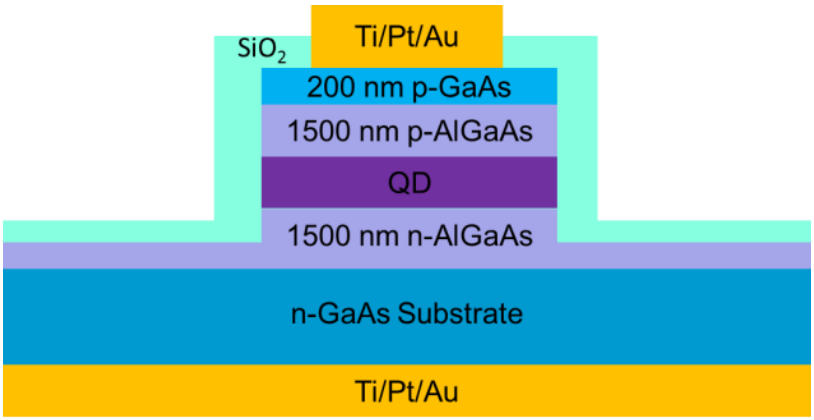

Figure 51: Cross section of ring/bar laser. InAs QDs have been embedded in the gain region.

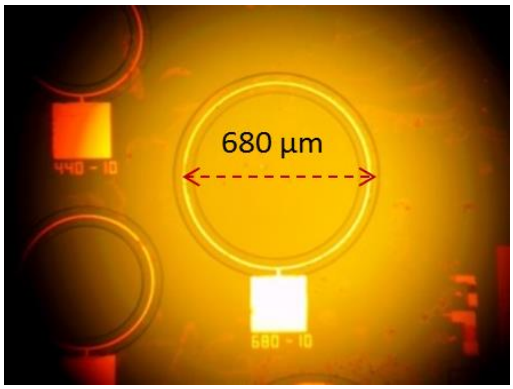

Figure 52: Top view of completed ring laser with 680 µm diameter.

A completed ring laser device is shown in Figure 52 in the top view. A square pad located on the bottom is added for the purpose of making electrical contact with probes, but the pad can fit inside the ring if the device were located on an actual slider. Using the setup shown in Figure 37, we obtain emission spectra. Figure 53a presents the spectrum of a 440 μm diameter, 10 μm wide laser during operation. The output light vs. drive current characteristic for the same device is shown in Figure 53b.

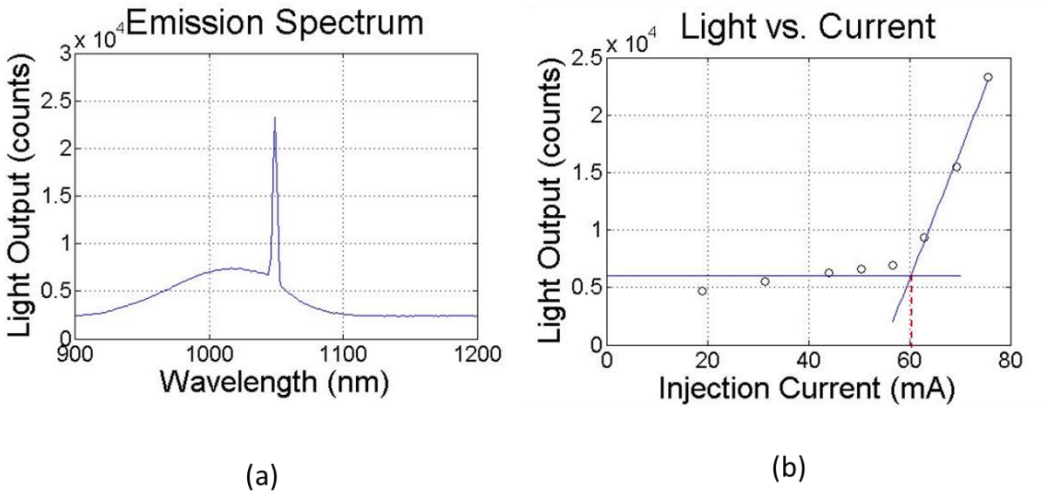

Figure 53: (a) Spectrum plot for a 440 μm diameter, 10 μm wide ring when it is lasing. The lasing wavelength is 1050 nm and the drive current shown here is 76 mA. (b) Light intensity in photon counts vs. drive current is shown for the same device. The threshold current is extracted to be 60 mA, shown by the red dashed line.

Ring lasers of radii ranging from 50-380 μm were measured and the light vs. current characteristic recorded. As a comparison, the same was done for bar lasers of length 500-2500 μm. All devices measured had a constant width of 10 μm. From these plots, the threshold current can be extracted for each device and converted into a current density. We then plot J_{th} as a function of ring radius and bar length, and observe their individual behavior in the scatter data in

Figure 54. We develop a model to calculate J_{th} based on device dimensions, examining in particular the impact of bending loss for ring lasers on their J_{th}.

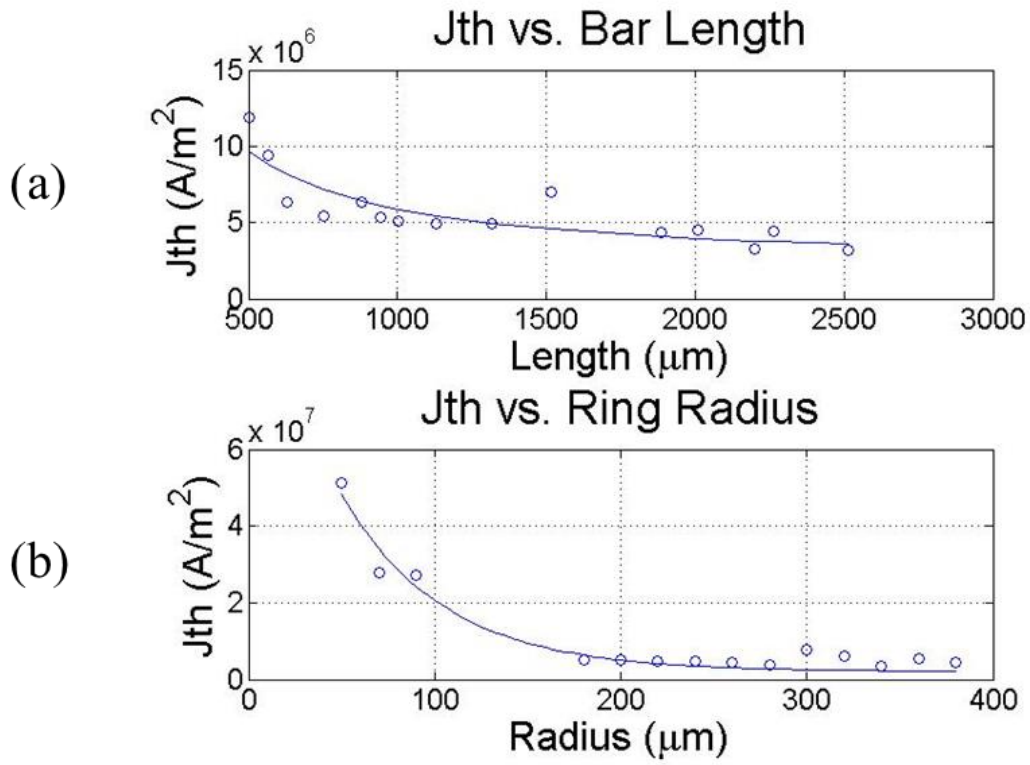

Figure 54: Scatter plot shows experimental data of J_{th} vs. length for bar lasers (a) and radius for ring lasers (b). Solid line shows the fitted result using eq. (4.1.2) and (4.1.4) below.

We follow the premise that the threshold current density is a measure of how much heating per unit area the device will experience in order to lase so a lower J_{th} is desired. Thus, we begin our discussion of the bending loss by first revisiting the relationship between J_{th} and bar length L for straight cavity lasers [83]:

$$J_{th} = J_0 + \frac{1}{A}\left[\alpha_i + \frac{1}{2L} ln\left(\frac{1}{R_F R_R}\right)\right] \quad (4.1.1)$$

Here J_0 is the transparency current density, A is a constant with units of cm/A, α_i is the internal loss in cm^{-1}, and R_F and R_R are respectively the front and rear mirror reflectivity. Typical GaAs based lasers have $R_F = R_R = 0.32$ for uncoated facets [45], and so we will assume this value for our mirror reflectivity in the following calculations. Of course, one can increase the mirror reflectivity with coatings but this will add more complexity to the laser fabrication process.

Examining eq. (4.1.1), we rearrange the terms such that it will be in the form of a linear equation with the independent variable *1/L*:

$$J_{th} = \frac{1}{2A} ln\left(\frac{1}{R_F R_R}\right) \cdot \frac{1}{L} + k \quad (4.1.2)$$

where $k = J_0 + \alpha_i/A$. Thus, we use our experimental data on bar lasers to plot *1/L* vs. J_{th}, as shown in Figure 55. We extrapolate the y-intercept to obtain a value of 207 A/cm^2 for *k*. Note that the three quantities included in *k* are all material parameters independent of device geometry. This allows us to substitute *k* into our calculations for ring lasers. In our formulation, we lump J_0 and α_i together, fitting for *A* separately.

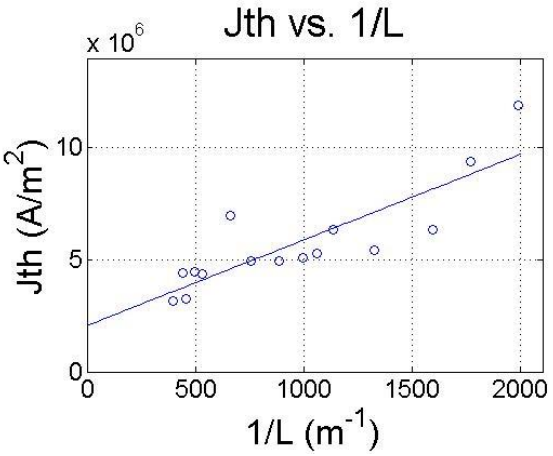

Figure 55: A plot of the J_{th} vs. 1/L for bar lasers. Y-intercept is extrapolated and equated to $k=J_0+\alpha_i/A$.

Upon further examination of eq. (4.1.1), we note that the quantities in the brackets describe the losses in the system. For bar lasers, they consist of internal and mirror loss. For rings, mirror loss must be replaced by bending loss since our ring lasers do not have output facets. Thus, eq. (4.1.1) is rewritten as:

$$J_{th} = J_0 + \frac{1}{A}[\alpha_i + \alpha_B] \qquad (4.1.3)$$

where α_B is the bending loss. Alternatively, eq. (4.1.3) can also be rewritten to include k from earlier:

$$J_{th} = k + \frac{\alpha_B}{A} \qquad (4.1.4)$$

It has been shown that, α_B increases exponentially with decreasing radius [84]:

$$\alpha_B = C_1 e^{-C_2 R} \qquad (4.1.5)$$

where C_1 (Nepers/m) and C_2 (m^{-1}) are constants and R is the ring radius. Substituting eq. (4.1.5) into (4.1.4) will result in an expression relating ring radius to threshold current density. It is now evident that we have three parameters to fit: C_1, C_2, and A with the latter constrained to be the same for both bar and ring lasers. Thus, we simultaneously fit A to eq. (4.1.2) and (4.1.4) to experimental J_{th} respectively for bar and ring lasers.

When fitted this way, our result for A is 0.015 cm/A and the fit is shown in Figure 54. To rationalize this result, we can use the laser rate equations to show [85]:

$$A = \frac{g' \tau \Gamma}{de} \qquad (4.1.6)$$

where g' is the differential gain in units of cm^2, τ is the carrier lifetime, Γ is the optical confinement factor, d is the thickness of the active region, and e is the electric charge. For our

ring lasers, the active region is 200 nm in thickness. Of particular interest then are the constants g', τ, and Γ. Kamath *et al.* experimentally measured a differential gain value of 1.7×10^{-14} cm^2 for a GaAs based quantum dot laser [86]. Reference [87] shows that the carrier lifetime for quantum dot based devices can be as low as 0.4 ns. Bhattacharya states in [88] that typical values for the optical confinement factor of quantum dot lasers are around 0.01. Using these values in eq. (4.1.6) results in A on the order of 10^{-2}-10^{-1} cm/A. Our value of 0.015 cm/A falls within this range.

Next we examine J_0 and what we can infer about it from our fitted value of k in eq. (4.1.2). Reported values of J_0 for quantum dot lasers range from 50-100 A/cm^2 [89]. Internal loss values typically range from 2-15 cm^{-1} [83], and those of quantum dot lasers are expected to be on the low end of this range or even lower due to the additional dimension of quantum confinement. Substituting an internal loss value from literature and our value for A into the second term of k, α_i/A, we find that it is at least as large as the first term of k, which is J_0. Since we fitted k to be 207 A/cm^2, the contribution of J_0 must be half or less, therefore resulting in it falling within literature range of values of 50-100 A/cm^2.

Finally, we examine our fitted values of C_1 and C_2 which are related to the bending loss in eq. (4.1.5) to see whether they are reasonable. Austin *et al.* provides experimental data on the insertion loss of two 90^o bends as a function of radius of curvature in GaAs/AlGaAs waveguides [90]. They report in units of dB/90^o bend which we convert to cm^{-1} for comparison. Because the insertion loss in [90] is the sum of the bending loss and the inherent loss present in a straight waveguide, we modify eq. (4.1.5) by adding another constant C_3:

$$\alpha_B = C_1 e^{-C_2 R} + C_3 \quad (4.1.7)$$

We then use eq. (4.1.7) to fit to this data to obtain the constants C_1, C_2 and C_3, which are 8.6×10^4 Nepers/m, 1.7×10^4 m^{-1}, and 2.4×10^3 Nepers/m, respectively. When fitting eq. (4.1.4), which incorporates the bending loss, to our own experimental data we obtain 3.8×10^4 Nepers/m and 2.1×10^4 m^{-1} for C_1 and C_2, which are comparable to that of Austin *et al*. We summarize our findings in Table 4.

A comparison of the data fit for J_{th} vs. device size using the numerical results of Table 4 is shown in Figure 56 in which the maximum length taken by the device refers to length for bar lasers and diameter for ring lasers. This way, we can compare both types of devices in terms of their footprints. Figure 56a shows that for ring lasers J_{th} increases dramatically only when the diameter decreases below ~300 μm. According to eq. (4.1.3), the bending loss must have become significantly higher to have such a noticeable impact on J_{th} since that is the only parameter in the equation to depend on diameter.

Table 4: Numerical results for fitted parameters of bending loss.

Parameter	Quantity	Units
k	207	A/cm^2
A	0.015	cm/A
C_1	3.8×10^4	Nepers/m
C_2	2.1×10^4	m^{-1}
C_1^*	8.6×10^4	Nepers/m
C_2^*	1.7×10^4	m^{-1}
C_3^*	2.4×10^3	Nepers/m

*Parameters resulting from fit to Figure 3 in [90]

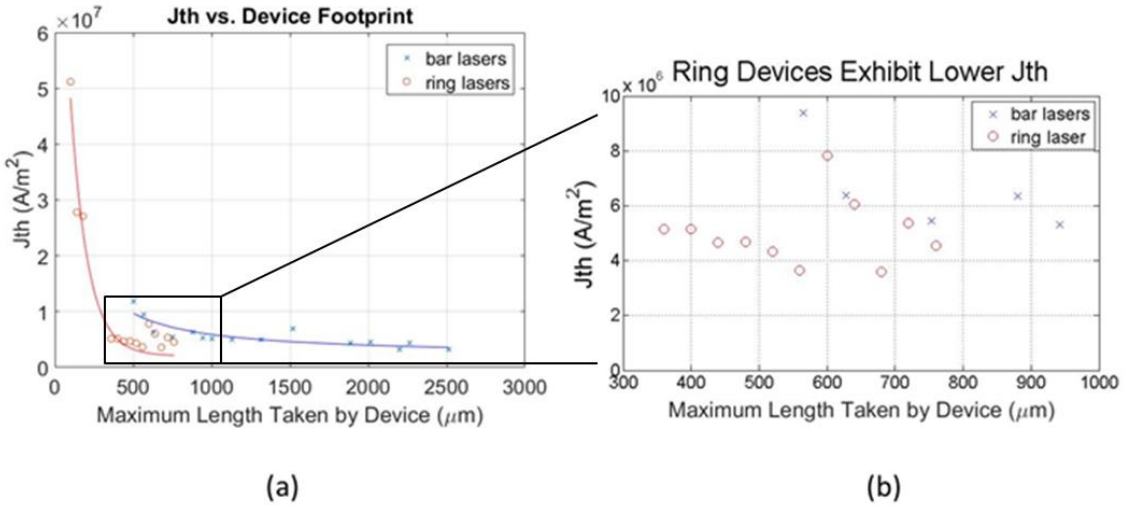

Figure 56: (a) Scatter plot shows experimental data of J_{th} vs. length for bar lasers and diameter for ring lasers. The length and diameter are treated as the maximum length of the footprint for their respective devices. The lines represent fitted results. (b) Ring lasers exhibit lower J_{th} than bar lasers for the footprint range of 300 to 760 μm.

Note that for ring lasers of diameter above ~300 μm, J_{th} is below that for bar lasers of similar length (and smaller, as suggested in Figure 56a) which is shown more clearly in Figure 56b. Given the space constraints on the HAMR slider, the lowest J_{th} that can be achieved for a laser will be with the ring geometry, leading to more efficient operating conditions with less expected thermal load on the slider.

The thermal load can be estimated using eq. (4.1.1) because several variables in this equation depend on temperature: the transparent current density J_0, the constant A, and the internal loss α_i. According to data found in Tansu *et al.*, J_0 is linearly dependent on temperature [91]. We fit the data found in Figure 7 of the paper to determine a slope and y-intercept for the linear expression of J_0 as a function of temperature. For the constant A, which is really the slope of the gain curve as a function of current density, we use data found in Figure 3 of Asada *et al.* [92]. Here we use the injection carrier density to approximate the current density and extract

slopes from the peak gain from temperature ranging from 100-400K. We scale the values such that at room temperature A = 0.015 cm/A, which match our fitted result in this section. We find the constant A to have an exponentially decreasing relationship with temperature. To examine effect of temperature on internal loss, we use data from Figure 14 from Zou *et al.* [93]. Again, we find a linear relationship and extract a slope and y-intercept. Combining these results allow us to calculate and plot temperature rise (from room temperature at 300K) as a function of threshold current density J_{th} in Figure 57 with the values scaled so that they match our laser.

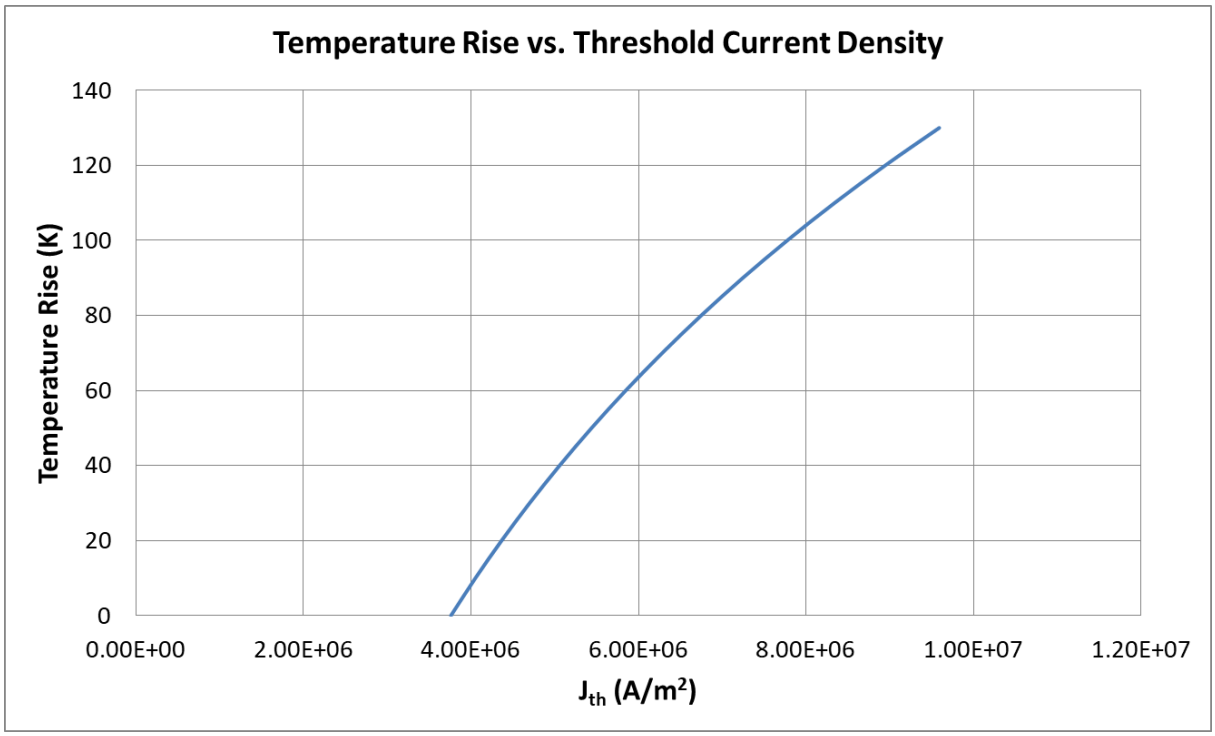

Figure 57: Plot of estimated temperature rise as function of threshold current density J_{th}. Temperature rise is referenced to room temperature at 300K.

In the device footprint range of 300 to 760 μm, we observe that J_{th} ranges from 4×10^6 to 6×10^6 A/m^2 for ring lasers and 6×10^6 to 8×10^6 A/m^2 for bar lasers. For thermal load, the plot of Figure 56 suggests that bar lasers will experience a temperature rise of 60-100K from

room temperature while ring lasers will only experience a temperature rise of at most 60K. Since slider temperature can already increase by more than 60K during the write process [94], it is desirable to eliminate additional heat from the laser as much as possible.

The analysis presented in this section indicates that given the space constraints of mounting a laser to the backside of a HAMR slider which only may be 700 by 300 um^2 [82], a laser with a ring geometry is more preferable to one with a bar geometry. For rings of diameter between 300 and 760 μm, the threshold current density is lower than bar lasers of the same footprint or smaller. Below 300 μm diameter, the bending losses of a ring laser increases exponentially according to eq. (4.1.5) and therefore drastically increases J_{th}. The threshold current density should be kept low to decrease device heating. If using a ring laser with diameter from 300 to 760 μm, the temperature rise is not expected to increase by more than 60K whereas a bar laser with length in this range will experience a temperature rise of 60-100K. Thus, the ring geometry is recommended over the bar for designing a laser to be mounted on the back of a HAMR slider with space constraints due to lower temperature rise.

4.2 Heat Sinking

In HAMR, it is desirable to have an electrically pumped laser providing power continuously and at room temperature. Although CW room temperature laser operation of a variety of devices such as InP microdisk lasers in [95] and Y-junction ring lasers in [96] has already been demonstrated, the majority of these devices are optically pumped by an external laser. While CW room temperature operation of electrically pumped lasers has also been achieved [97], these injection lasers require much more efficient heat sinking than optically pumped ones, and their successful implementation still remains a challenge. In addition, the

requirements of sufficient heat sinking increase as device dimensions decrease. In this section we analyze how much heat sinking is needed such that our laser operates in CW.

Joule heating, the generation of heat by passing an electric current through a metal, provides a foundation for analyzing heat sinking of lasers for HAMR. Figure 58 shows the cross section of a ridge laser with top and bottom metal contacts. Current flows from the top (p-side) to the bottom (n-side) contact, generating heat throughout the stack.

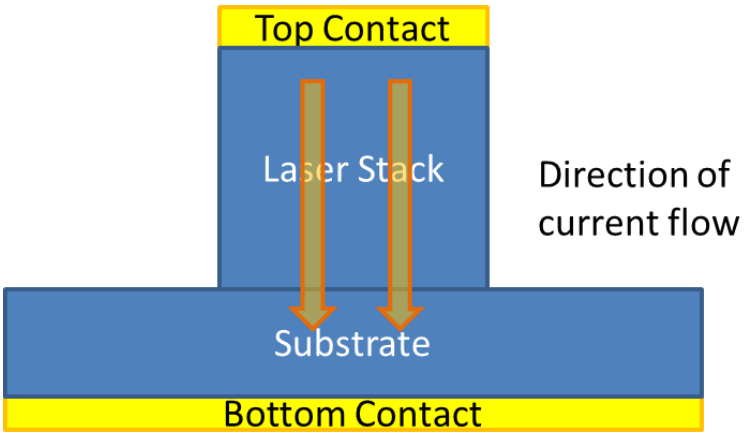

Figure 58: General structure of a ridge type laser. Current flows through the laser stack, where the gain medium is located, from the top to bottom contact.

The amount of heat produced depends on the square of the current *i*, the resistance of the laser structure *R*, and the time of current flow *t*. This is summarized in Joule's Law of Heating [98]:

$$Heat \propto i^2 \cdot R \cdot t \qquad (4.3.1)$$

We quantify the heat produced in our laser by determining the temperature rise in the device, and we recall that the peak emission wavelength of a laser tends to shift as temperature increases. A typical value for wavelength shift due to temperature for InAs QD, GaAs based lasers is 0.06 nm/K [99]. For our lasers we determined the amount of peak shift that occurred

from low drive current to current just before threshold and assumed the same shift rate. We pick the moment just before threshold due to the fact that lasing may occur slightly off peak. Figure 59 shows the shift in the peak emission wavelength for one of our lasers.

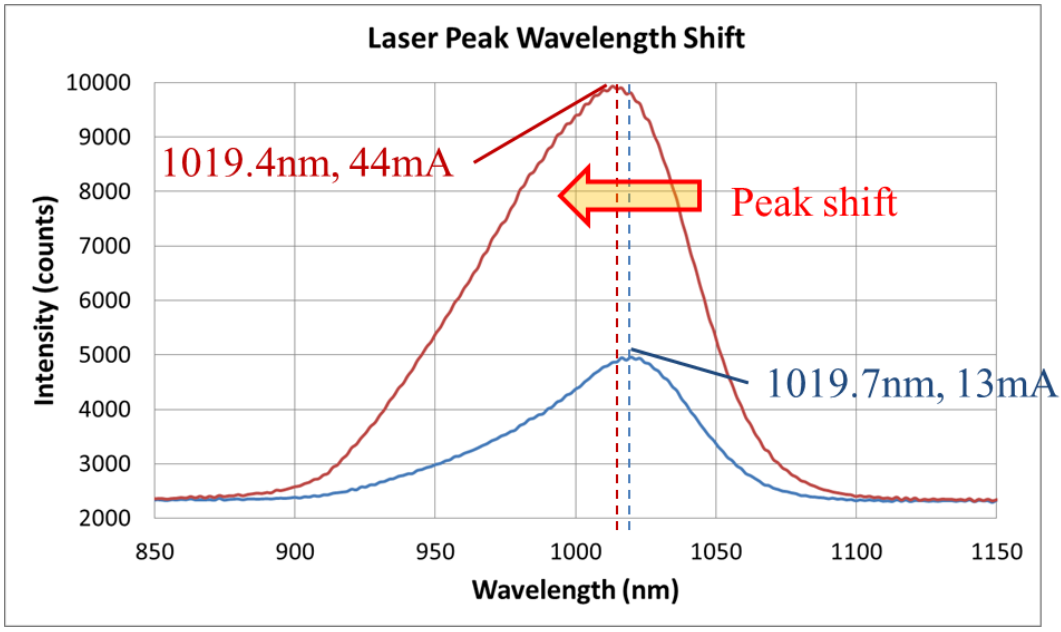

Figure 59: A 1.5 nm shift occurs in the peak wavelength of a 1000 by 5 μm bar laser as the drive current is increased from 13 mA to 44 mA which is just before threshold. At a shift rate of ~0.06 nm/K, a 0.3 nm shift means an increase in temperature of 5K. The spectrum is obtained at 20% duty cycle.

We obtain emission spectra for a 1000 by 5 μm bar laser at 20% duty cycle. At 13 mA, the peak wavelength is 1019.7 nm. Just before threshold, the peak wavelength has shifted to 1019.4 nm. A shift of 0.3 nm corresponds to a temperature rise of 5K (from room temperature).

Since we know we can achieve lasing with a temperature rise of 5K at 20% duty cycle, if we are able to increase the duty cycle to 100% and keep temperature rise the same then CW operation is possible. Avoiding additional temperature rise is important due to the fact that I_{th} increases as a function of temperature as shown in Figure 60, estimated for the laser whose

emission spectra are shown in Figure 59. The threshold current (shown in blue) is calculated using the same theory behind the plot in Figure 57.

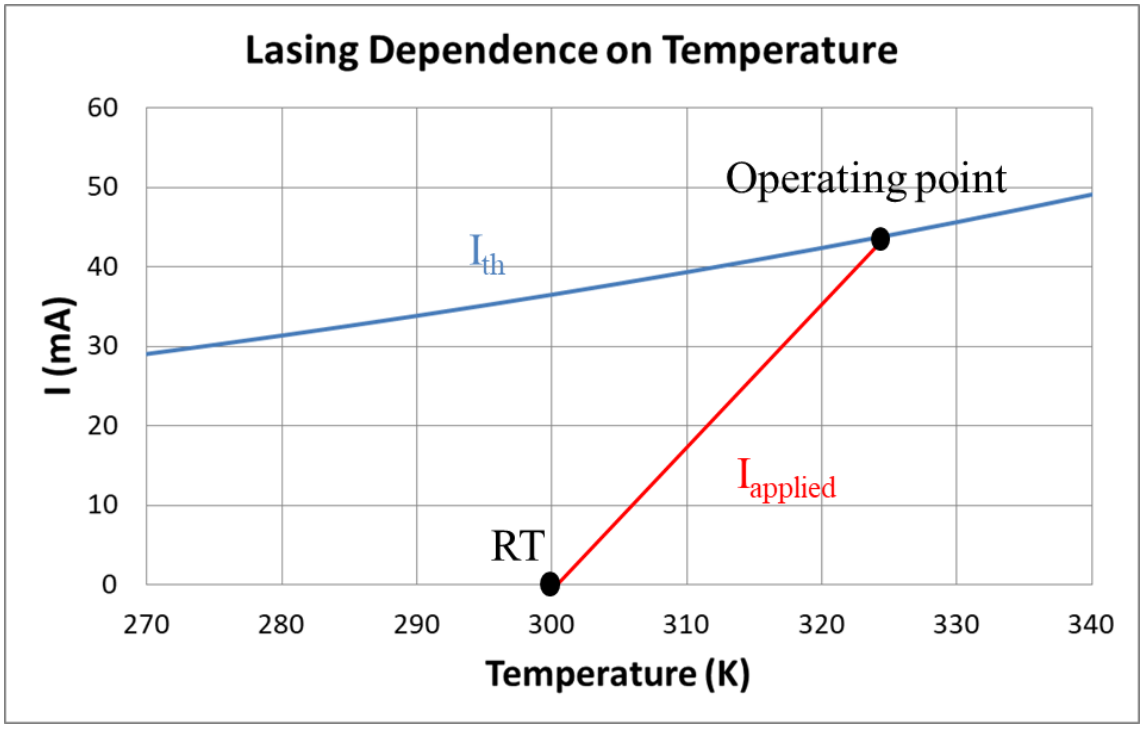

Figure 60: A plot showing the estimated dependence of I_{th} on temperature of a 1000 by 5 μm bar laser (blue). Starting at room temperature (RT), current can be applied to pump the laser (red). More current needs to be applied as the laser experiences more heating. If $I_{applied}$ intersects I_{th}, then lasing will occur and this point is labelled as the operating point. The slope of $I_{applied}$ is inversely related to the thermal resistance.

When a pump current is applied ($I_{applied}$, shown in red) with the laser initially at room temperature (RT), the current will cause temperature inside the laser to rise and in turn raise the requirements for I_{th}. If $I_{applied}$ intersects with I_{th} then we achieve lasing, and this point is labelled as the operating point. No lasing occurs otherwise. Whether $I_{applied}$ intersects with I_{th} depends on the slope of $I_{applied}$. This slope has an inverse relationship with the thermal resistance of the laser, which has units of K/W.

To calculate the thermal resistance, we need to determine the amount of power dissipated that caused the temperature rise of 5K. This can be obtained by measuring the current and voltage across the laser at threshold, and we estimate a power of 46 mW being dissipated at 20% duty cycle. This results in a thermal resistance of 5/0.046 = 109 K/W. Our metric for whether a heat sink can allow CW operation for the laser is to decrease this thermal resistance by a factor of 5 since it was obtained at 20% duty cycle. This way, the laser can still maintain a temperature change of 5K even at peak dissipated power (0.046*5 = 0.23W). If we do not keep temperature from increasing, it is likely that the laser will overheat and never reach threshold at CW.

When adding a heat sink, we have 2 options as shown in Figure 61: (1) place the heat sink on top of the laser stack (p-side) or (2) beneath the substrate (n-side).

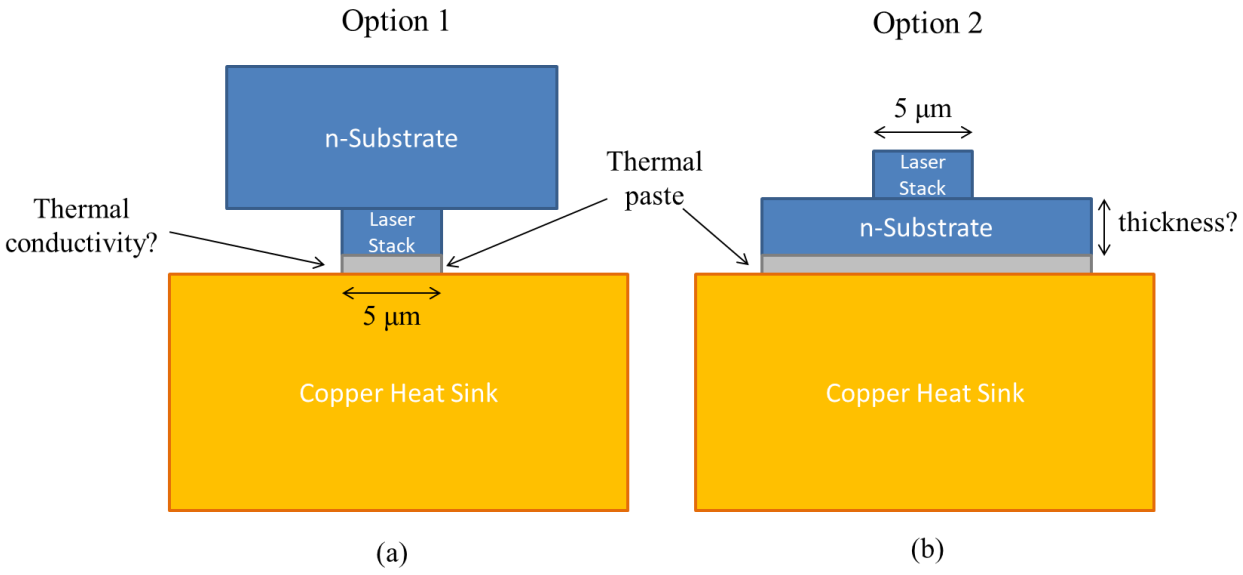

Figure 61: (a) Option 1: Laser is flipped over to contact a copper heat sink on the p-side. The primary concern is the thermal conductivity of the thermal paste needed to make contact to the heat sink. (b) Option 2: Laser makes contact with the copper heat sink from the n-side substrate. In this case, the substrate needs to be thinned down in order for the laser to make use of the heat sink.

The heat sink can be made from copper, as it is a common material to use for heat sinks and has high thermal conductivity. For both options, when the laser makes contact to the copper heat sink we will need a layer of electrically conductive thermal paste for adhesion. Thermal paste is usually applied as a "paper-thin" layer [100], and a standard A4 sheet of paper is 50 μm thick [101]. However, from practice the paste is usually about ~10 μm in thickness, so we will use this value in our simulations which are all performed in COMSOL. Additional simulation conditions are: material properties for air, copper, and GaAs have been left as the default ones provided by COMSOL; thermal insulation boundaries are placed at the left and right of the simulation region while temperature boundaries of 293K are placed at the top and bottom; and laser ridge width is constant at 5 μm. The schematic of the cross section geometry used in COMSOL is shown in Figure 62 for both options 1 and 2.

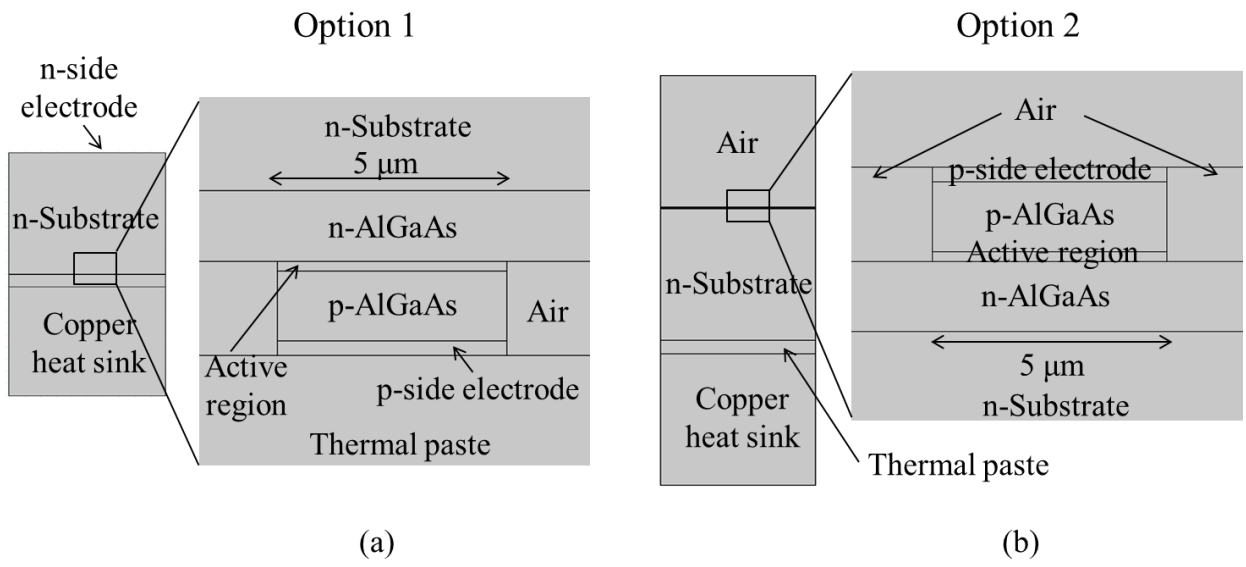

Figure 62: Schematic of the cross section geometry used in COMSOL to simulate (a) heat sink making contact with the laser from the p-side electrode and (b) heat sink making contact with the laser from the n-substrate. In (b), the n-side electrode is not visible but it is between the thermal paste and the n-substrate.

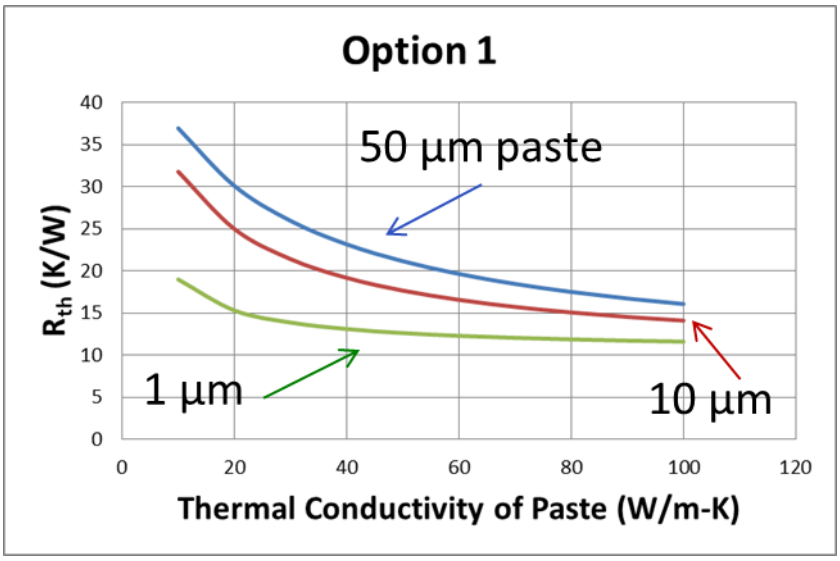

Figure 63: Option 1 is when the laser is flipped over to make contact to a copper heat sink from the p-side. The plot shows simulated results of the laser thermal resistance vs. thermal conductivity of the paste used for contact with various paste thicknesses. CW operation for the laser with a 10 µm thick paste requires 40 W/m-K or better for the paste.

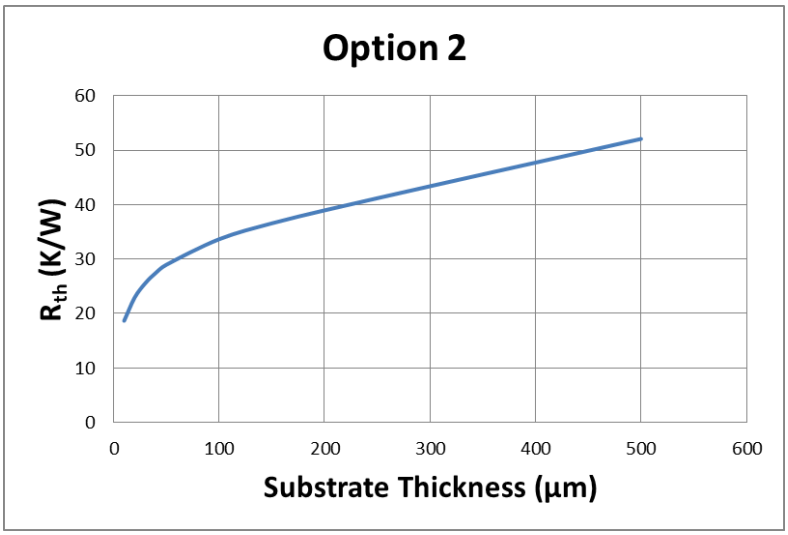

Figure 64: Option 2 is when the laser makes contact with a copper heat sink from the bottom of the substrate. It is independent of the paste thickness from 1-50 µm. Assuming that a commercially available thermal paste with the highest thermal conductivity is used, the plot shows laser stack thermal resistance vs. the substrate thickness. The substrate needs to be thinned to nearly 10 µm to allow CW operation.

We start our heat sinking analysis with option 1. In this scenario, the laser is flipped onto its p-side to make contact with a copper heat sink. The primary concern here is the thermal conductivity that is needed for the thermal paste as it exists as a layer between the laser and the heat sink. We extract the temperature change and heat dissipated in the gain medium to calculate a thermal resistance. Figure 63 shows a simulated plot of thermal resistance R_{th} of laser stack vs. the thermal conductivity of the paste for various thicknesses of the paste. We calculated before that our laser currently has thermal resistance of 109 K/W and needs to decrease by a factor of 5 for CW operation. According to Figure 63, a paste with thermal conductivity of > 40 W/m-K will be sufficient if we assume the standard 10 μm thick paste (thicker paste requires better thermal conductivity and vice-versa). Electrically conductive paste with liquid metal that exceeds 40 W/m-K is readily available on the market [102].

In option 2, the laser makes contact with the heat sink from the n-substrate. Because the substrate has relatively low thermal conductivity (< 50 W/m-K) and is much thicker than the laser stack, it needs to be thinned down using tools such as a focused ion beam (FIB) or a sanding machine for the heat sink to be effective from the n-side. Contacting from substrate also makes R_{th} independent of paste thickness from 1-50 μm. Figure 64 shows a simulated plot of thermal resistance of laser stack vs. the thickness of the substrate assuming we can get access to the best thermal paste available. We use a thermal conductivity value of 82 W/m-K from a product called "Coollaboratory Liquid Pro" found in [102]. Again the goal is to decrease the laser stack R_{th} by a factor of 5, and Figure 64 shows the substrate thickness to be near 10 μm to achieve this. Although industry has been able thin a wafer down to 10 μm in some cases, it considers 50 μm to already be "ultra-thin' and this thickness is more commonly the limit [103]. Therefore, option 2 cannot be practically implemented because of the thin substrate requirement.

It is also possible that a heat sink may not be needed by decreasing the width of the laser. It is known that a narrow ridge width can help the laser achieve better heat dissipation but at the cost of an increase in threshold current density [104]. We examine the way heat is dissipated from the laser stack as a function of ridge width using COMSOL simulation. Figure 65 shows 2 configurations where the laser is wide compared to substrate in (a) and is narrow in (b).

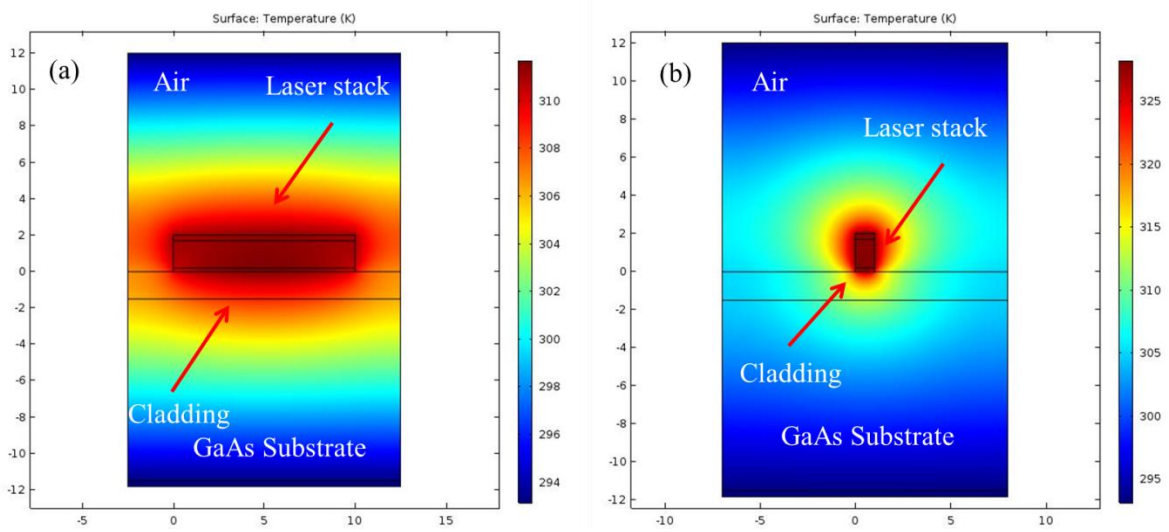

Figure 65: (a) Temperature distribution for laser stack that is wide compared to substrate. (b) Temperature distribution for laser stack that is narrow compared to substrate. Position scale is in microns.

In the simulation, the laser gain medium is treated as a stripe source, resulting in most of the heat being distributed in the laser stack itself. The heat hardly reaches the substrate unless the laser is wide in comparison, as seen in Figure 65a. When the laser is wide, heat flows uniformly into air and the substrate. We can use the thermal conductivity equation to model:

$$\frac{Q}{t} = \kappa A \frac{(T_a - T_b)}{d} \qquad (4.3.2)$$

where Q is the energy dissipated, t is time, κ is the material thermal conductivity, A is the heat sink contact area, d is the heat sink thickness, and $T_a - T_b = \Delta T$ = difference in temperature

between laser and heat sink. However, a 1 μm laser is narrow compared to the substrate, and the heat emits radially from the laser stack as shown in Figure 65b. In this case, heat can not only flow up and down but also sideways. We thus continue to perform our analysis using simulation.

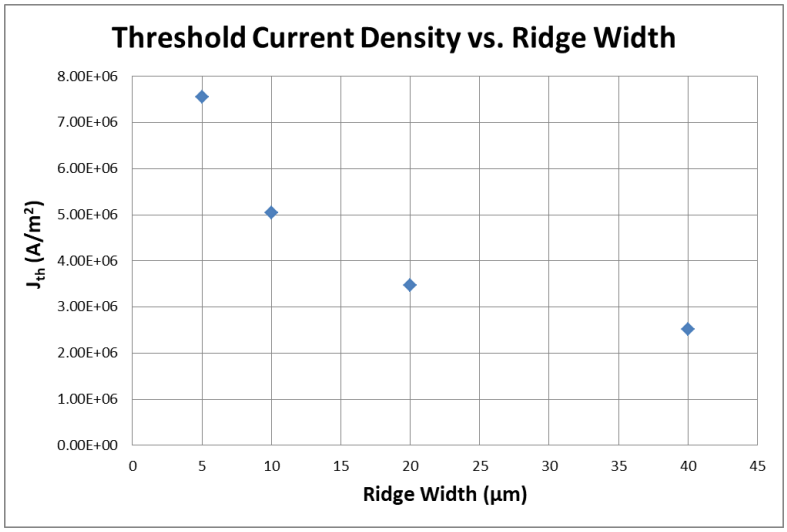

(a)

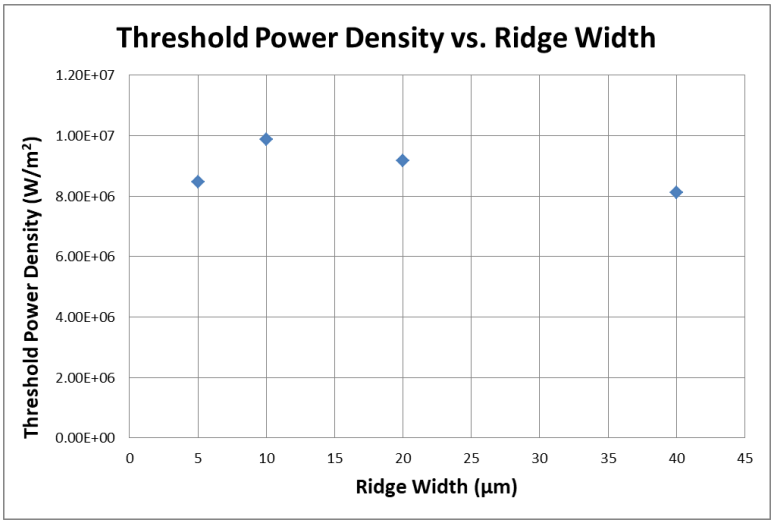

(b)

Figure 66: Experimental data for (a) threshold current density and (b) threshold power density of lasers with different ridge widths. These lasers are fabricated on the same chip and are all 1000 μm long.

In Figure 66a, we plot J_{th} vs. laser ridge width for lasers fabricated on the same chip and are all 1000 μm long. Indeed, we see a sharp increase in J_{th} when the ridge becomes narrower. However, if we plot the dissipated power density at threshold (in a slice of gain medium) vs. ridge width, then we see that there is only an increase when the width decreases from 40 to 10 μm as shown in Figure 66b. When the width decreases from 10 to 5 μm, the power density actually decreases as well. Power density may decrease even further when the ridge width is shrunk to 1 μm, but fabrication challenges have prevented us from making an actual 1 μm wide laser.

Although J_{th} may increase at 1 μm ridge width, if temperature in the gain medium does not increase past 5K, then the laser should still be able to function and not overheat itself. Using simulation, we predict a thermal resistance of 134 K/W with a 1 μm wide laser. If temperature change is 5K, then the maximum power dissipated at CW can be 40 mW, or 7.5 mW at 20% duty cycle. This translates to an allowable power density of 7.5×10^6 W/m^2. If the power density continues the same trend of decreasing as seen from 10 to 5 μm width, then a 1 μm wide laser is expected to be able to lase with a dissipated power density of 7.3×10^6 W/m^2 which is less than the allowable limit. Thus, decreasing the ridge width to 1 μm can allow the laser to operate in CW without any need for a heat sink.

In our discussion so far, we have not accounted for the heat capacity of any of the materials. It is important to know how much heat can be retained in the structure, as thermal resistance only indicates an expected temperature rise. To further redirect accumulated heat, one can integrate the copper heat sink or 1 μm wide laser with another component that can retain the heat transferred. For example, Leers *et al.* integrated high performance diamond composites with copper in their next generation heat sinks [105].While they used a conductively cooled scheme,

heat sinks can also be convectively or water cooled. Luo *et al.* combined a micro heat sink with a micro heat pipe in one efficient system made of silicon-aluminum [106]. While these heat sinks may be effective, they are quite complex, and a simpler scheme is desired for HAMR.

4.3 Conclusion

We have examined how to optimize our laser with reducing device heating by choosing the right geometry and an analysis of how to achieve CW operation. We find that that for ring lasers of diameter between 300 and 760 μm the threshold current density is significantly lower than bar lasers of the same or smaller footprint. Having lower J_{th} is advantageous because the device should experience less heating. Due to space constraints on the back of the HAMR slider, a ring geometry is recommended for the laser to minimize slider temperature rise (< 60K). For CW operation, we first find experimentally that our lasers have a thermal resistance of 109 K/W and temperature change of 5K to reach threshold at 20% duty cycle, and our goal is to decrease the value of 109 K/W by a factor of 5. We present 2 options of mounting a copper heat sink to our 5 μm wide lasers, with option 1 being flipping the laser upside down to contact from the p-side and option 2 being thinning the substrate to contact from the n-side. Option 1 requires a thermal paste between the heat sink and laser with a thermal conductivity greater than 40 W/m-K. Option 2 requires the substrate to be thinned down to near 10 μm if the thermal conductivity of the paste is the highest available on the market at 82 W/m-K. We recommend option 1 as it is difficult to thin down the substrate precisely to 10 μm in option 2. Decreasing the laser ridge width to 1 μm is a third possibility of allowing the laser to operate in CW if one has the right tools to overcome the associated fabrication challenges.

Chapter 5: Waveguide-Resonator-NFT Light Delivery System

So far we have discussed a concept for a mode stabilized laser with optimized geometry and proper heat sinking to allow a laser to operate in CW on the back of a slider. Now we need a way to deliver this power to the recording medium. Recall that HAMR requires the generated light spot size to be below the diffraction limit so we cannot just directly shine the laser light onto the medium. Instead, a near field transducer (NFT) is required to successfully reduce the laser spot size down to the tens of nanometers. The main challenge lies in efficiently coupling the laser light to the NFT. Various methods exist in literature such as the lollipop configuration mentioned in Chapter 1. However, most of these methods still require relatively high-powered lasers in the optical output range of 30-80 mW [11]. Our goal is to reduce this power requirement to as low as 1 mW so as to eliminate another potential source of heating problem in HAMR. In the system we propose, the laser is coupled to a waveguide which is critically coupled to a dielectric resonator. The resonator then evanescently couples to the NFT. If the Q of the resonator is high enough, then the NFT acts as the dominant way for light to escape the resonator and therefore enabling high coupling interaction. This chapter starts with discussing the rationale behind our system design with fabrication and testing setup following. We use a combination of optical and thermal measurements to demonstrate the coupling of light into the NFT.

5.1 System Design

Referring to our light delivery system first shown in Figure 2, we observe three points of coupling interaction: (i) laser-waveguide, (ii) waveguide-resonator, and (iii) resonator-NFT. We

calculate the efficiency of the (i) laser-waveguide coupling using simulation and show the cross section geometry in Figure 67a.

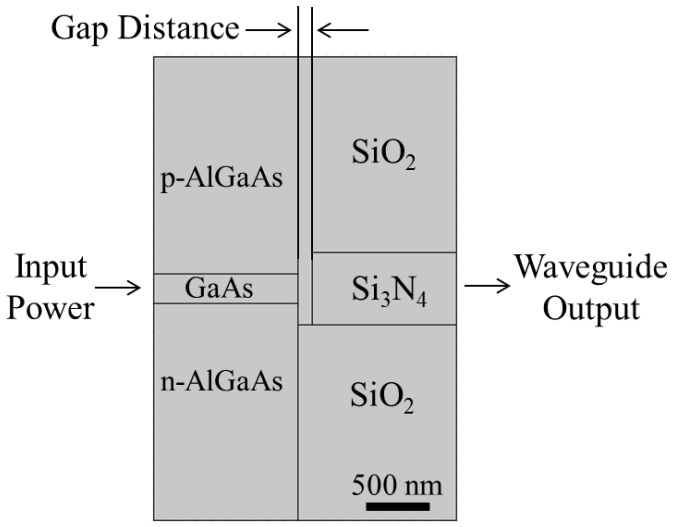

(a)

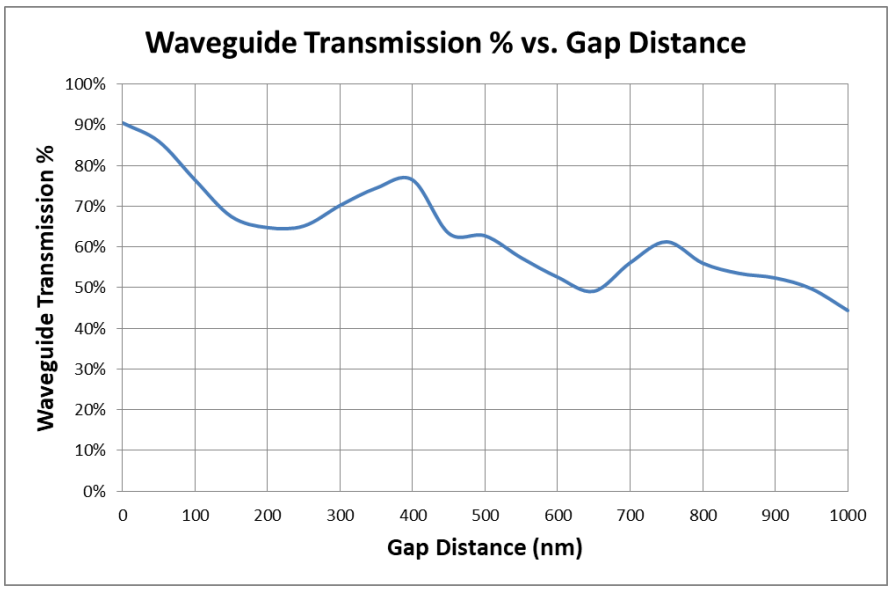

(b)

Figure 67: (a) Diagram of simulation geometry used in COMSOL for determining coupling of power from our laser to a dielectric waveguide. (b) Percentage of coupled power into the waveguide as a function of the gap distance between the waveguide and the laser.

Our laser has a GaAs gain region and AlGaAs cladding. The waveguide has Si_3N_4 core with SiO_2 cladding. A gap may exist between the laser and the waveguide due to fabrication tolerances. During simulation, a wave is launched from an input port on the left of the laser, and the transmitted power is calculated from an output port on the right of the waveguide. In Figure 67b, we plot the percentage of transmitted power vs. the gap distance. The transmission shows a periodicity of ~375 nm. If we envision a Fabry Perot cavity somewhere in our laser-waveguide, 375 nm corresponds to half a round trip so the wavelength in question is 750 nm. This means a mode index of 1.37 for a free space wavelength of 1030 nm, suggesting the periodicity is related to the SiO_2 region in between the laser and the waveguide. As for our expected coupling efficiency, we have shown that we can accurately place structures within 50 nm of the gain medium. Thus, we can couple over 80% power between the laser and the waveguide if they are coupled end to end.

For the (ii) waveguide-resonator interaction, critical coupling should allow 100% efficiency in theory between the two, as discussed in Section 2.7. We examine the (iii) resonator-NFT interaction through a combination of COMSOL simulation and calculations as we did in Chapter 3 with our laser and the MSS's. We also demonstrate through the simulations why coupling the NFT to a dielectric waveguide has much higher efficiency than coupling directly to the laser. Figure 68a shows a schematic of the simulation setup.

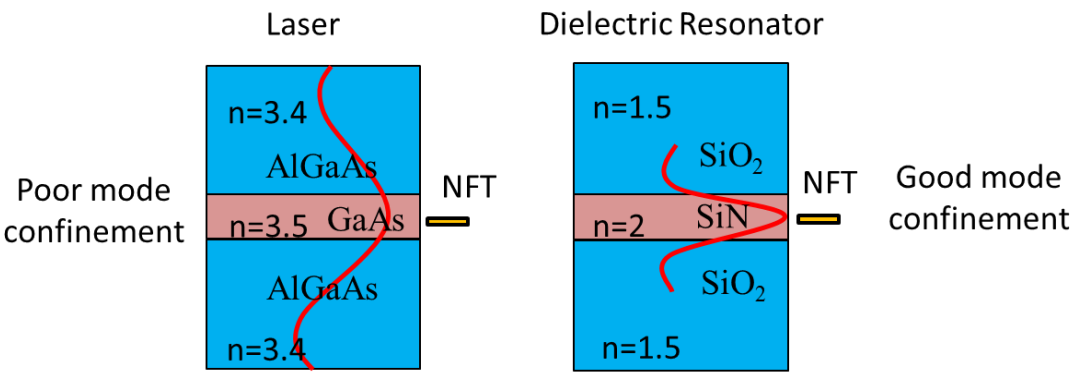

(a)

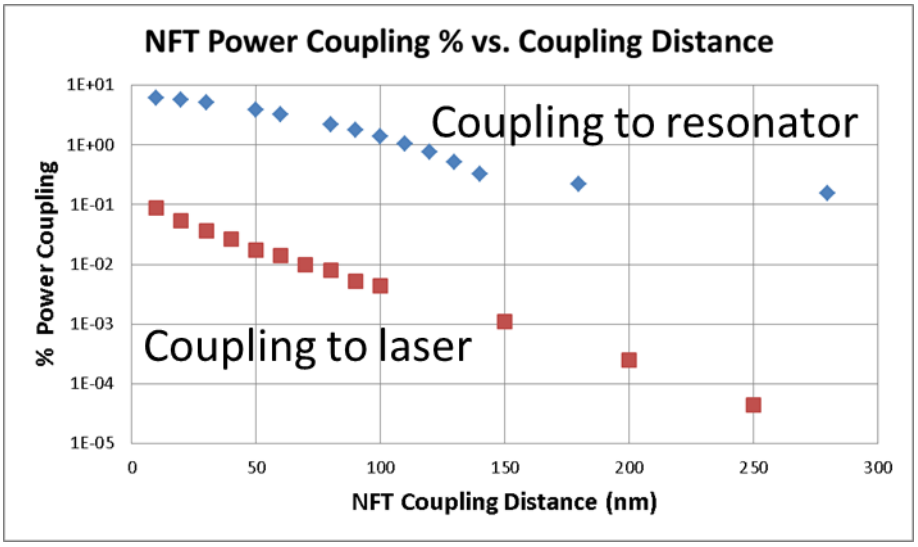

(b)

Figure 68: (a) Low index contrast in laser cladding leads to poor NFT coupling. (b) NFT coupling per pass increases from 0.01% to 5% when coupling to dielectric resonator at 50 nm away.

A NFT is placed next to the gain medium of a laser on the left and next to a resonator on the right. The key difference between the 2 scenarios is the index contrast between the core and cladding. For a laser, the difference in refraction index of GaAs core and AlGaAs cladding is 0.1 while for the resonator it is 0.5 between Si_3N_4 and SiO_2. Because of the lower index contrast in a

laser, the propagating mode is poorly confined in the gain medium. On the other hand, the higher index contrast of the resonator allow for better mode confinement. Figure 68b shows the difference index contrast makes in coupling to the NFT obtained via COMSOL. At 50 nm away, NFT coupling per pass increases from 0.01% to 5% when coupling to the resonator vs. the laser.

Although 5% coupling seems low initially, it is a "per pass" value and not the total coupling value. Using a Si_3N_4 based resonator at the wavelengths of our test laser (1500-1600 nm), we calculate the relationship between the resonator Q and the total power coupled into the NFT. The result is shown in Figure 69. The unloaded Q is shown in solid lines and the loaded Q (resonator with NFT) in dashed lines.

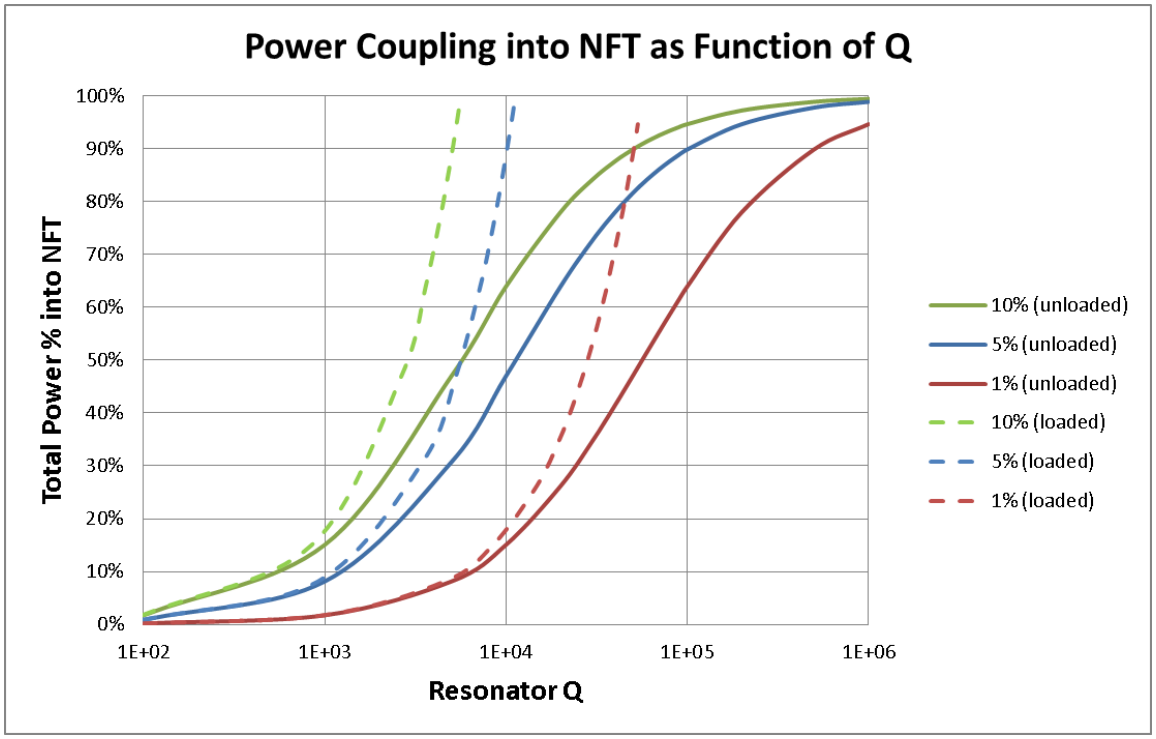

Figure 69: A semilog plot of the total power percentage coupled into the NFT as a function of resonator Q for NFT coupling efficiencies of 1%, 5% and 10% per cycle. For 5%, an unloaded Q of 1 million is required for 99% coupling, but a Q of 10^5 is enough for 90% coupling. The loaded Q seems to approach a limit of 10^5.

For our calculations, we start with a given unloaded Q and it is related to the finesse by:

$$Finesse = Q_{unloaded}\frac{FSR}{frequency} \quad (5.1.1)$$

where FSR is the free spectral range. For our resonator, we have a FSR of 2.17 THz and frequency of 195 THz. The finesse is related to the loss per cycle in the resonator ($Loss_{Res}$) by:

$$Loss_{Res} = \frac{2\pi}{Finesse} \quad (5.1.2)$$

Representing coupling to the NFT as a loss seen by the resonator ($Loss_{NFT}$), the fraction of power coupled per pass to the NFT is:

$$\%\ Power_{NFT} = \frac{Loss_{NFT}}{Loss_{Res} + Loss_{NFT}} \quad (5.1.3)$$

Note that if a certain fraction of power is sent to the NFT per pass, then the fraction of total power sent is the same. In addition, eq. (5.1.3) represents the case where the resonator is loaded with the NFT although we started our calculations with an unloaded resonator Q. The loss per cycle of this loaded resonator is $Loss_{Res} + Loss_{NFT}$. Using the sum of these losses, we then work backwards to derive a loaded Q. We revisit these equations in Section 5.3 to verify our experimental Q values.

In Figure 69, we plot the unloaded and loaded Q vs. % total power coupled to the NFT for various NFT coupling efficiencies. Higher efficiency lowers the requirement for $Q_{unloaded}$. If the NFT coupling is 5% per pass (our case), then a $Q_{unloaded}$ of 10^5 is needed for 90% coupling, while 99% coupling requires a $Q_{unloaded}$ of a million. It is possible to achieve such a high Q since there are reports in literature for Si_3N_4 based resonators with Qs greater than 10^6 [107]. In this

work, we devote our efforts to studying the coupling interaction between the resonator and NFT and not making the highest Q resonators we can. As we will show in Section 5.3, our resonator has a Q of ~10^4 and couples about 50% of its power to the NFT. This matches the loaded Q for 5% NFT coupling efficiency as shown in Figure 69.

With the individual coupling interactions analyzed, we take a look at the efficiency of the overall system and see how it can fit into HAMR. The minimum power requirement for heating the recording medium in HAMR is ~200 μW [11]. If 80% of the laser power can be delivered to the NFT and there is a maximum of 25% power transfer between NFT and media, then the initial power of the laser can be as low as 1 mW. As comparison, most other light delivery systems require laser sources with power in the range of 30-80 mW [11]. We speculate the higher source power requirement is a result of an off-chip laser being traditionally mounted on top of the HAMR slider [8]. The laser is coupled to the NFT through a series of collection and conditioning optics, which tend to limit the coupling efficiency. We overcome this challenge by using an on-chip laser positioned on the backside of the slider that is monolithically integrated with the NFT.

Our 1 mW figure can be further lowered if the laser-waveguide coupling interaction can be improved. Currently its 80% coupling efficiency is obtained via butt coupling from a bar laser. However, alternative configurations exist and one is shown in Figure 70.

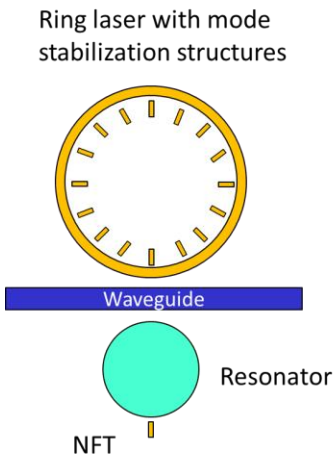

Figure 70: A ring laser with mode stabilizing structures (MSS) placed on the inside of the ring is evanescently coupled to a dielectric waveguide-resonator-NFT system.

A ring laser evanescently couples to the waveguide. MSS is placed on the inside of the ring to achieve a similar effect of mode stabilization. The evanescent coupling may approach critical coupling efficiency, thus enabling us to lower the power requirement of the source laser further.

In this work, we test our system using a Santec TSL-510 external tunable laser instead of the on-chip laser to avoid any potential malfunctions due to errors in the fabrication process. We only have access to a tunable laser at ~1500 nm, and we note that our MSS lasers operate at ~1000 nm and that the industry standard is ~800 nm. If we were not confined to our choice of equipment/materials, the best operating wavelength would be one which can deliver the most localized heat spot to the recording medium. We discuss the impact of lasing wavelength using a tapered NFT model in Section 7.2. Initial results suggest that 800 nm provides the most localized heat spot but the penalty associated with lasers at 1000 nm may still be acceptable.

Back to our tunable laser, light is fed into the waveguide via grating couplers and collected by a power meter at the output. There are many approaches to optimizing the coupling

efficiency of the grating in literature [108] [109]. Here we opt to use Lumerical, a simulation software based on the finite difference time domain (FDTD) method, to analyze our grating coupling efficiency. We show our grating parameters in Figure 71a.

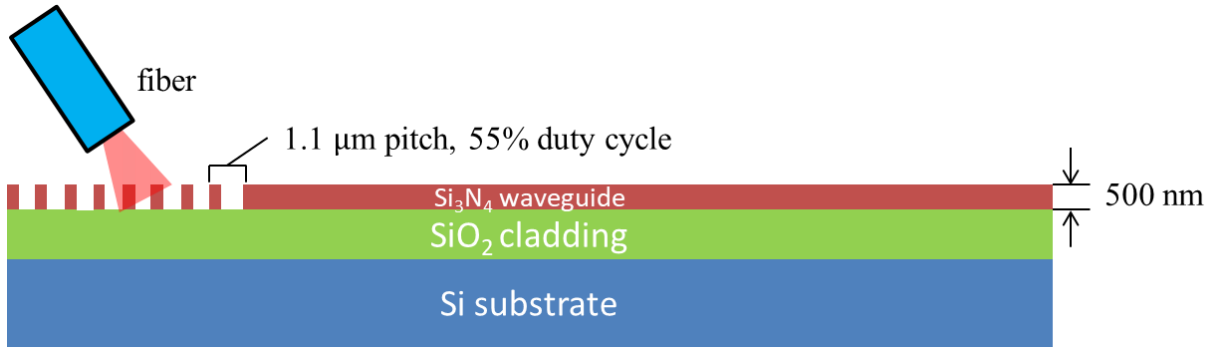

(a)

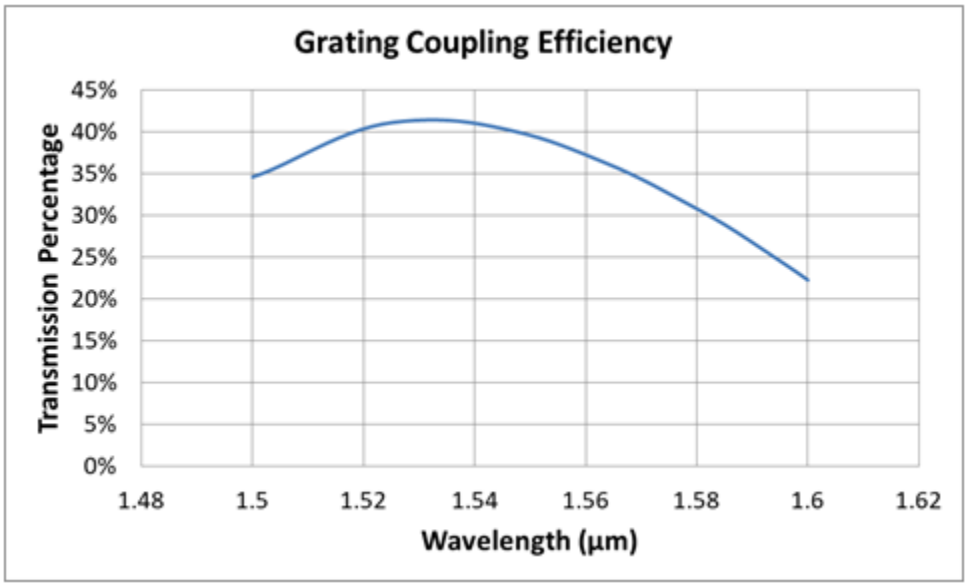

(b)

Figure 71: (a) A fiber sends light into the grating which couples into a 500nm Si_3N_4 waveguide. The grating has 1.1 µm pitch, 55% duty cycle. (b) Transmission percentage of fiber light into grating as function of wavelength. Peak transmission occurs around 1.53**µ**m at above 40%.

In our simulation, we place a fiber above a grating that feeds into a 500 nm thick Si_3N_4 waveguide on top of SiO_2 cladding and Si substrate. The 500 nm thickness is chosen such that the mode confinement in the waveguide is > 80%. Because we only have access to a tunable laser in the 1550 nm regime, we design our grating with the goal of optimizing transmission in this wavelength range. At a fiber incidence angle of 8°, we find that the grating should have a 1.1 μm pitch and 55% duty cycle. The transmission efficiency as a function of wavelength is plotted in Figure 71b. We find that peak transmission occurs around 1553 nm at above 40%. Although we simulated sending fiber light into the grating, the same coupling efficiency should apply at the grating output into the power meter fiber due to symmetry.

Once we achieve maximum laser to grating coupling, we need to design a taper length such that there is efficient mode conversion between the grating and the waveguide mode. The width of the grating is 15 μm, and an optical mode will experience significant loss when transitioning to a single mode waveguide which usually has width of ~1μm. By using a taper, we can change the shape and size of the optical mode such that there is a high coupling efficiency between cross sections of different sizes [110]. Figure 72a shows a top view of a grating and waveguide connected by a tapered structure. We use the EigenMode Expansion technique (EME) to calculate a taper length for a Si_3N_4 waveguide with SiO_2 cladding [111]. A plot of transmission efficiency vs. taper length is shown in Figure 72b. A taper length of at least 200 μm is sufficient for 90% transmission.

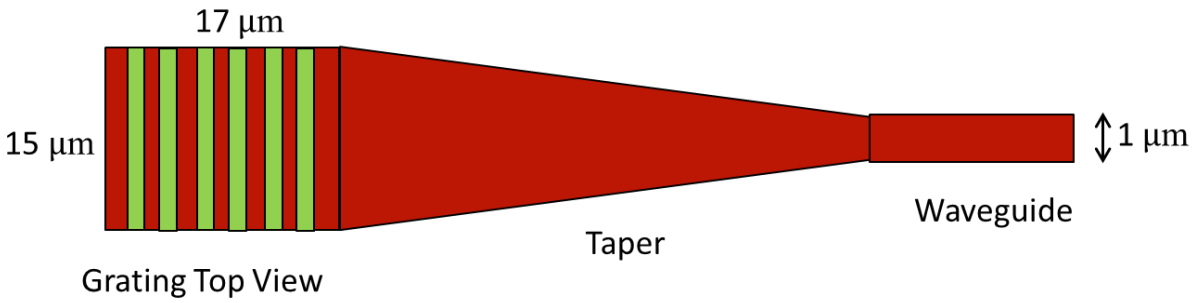

(a)

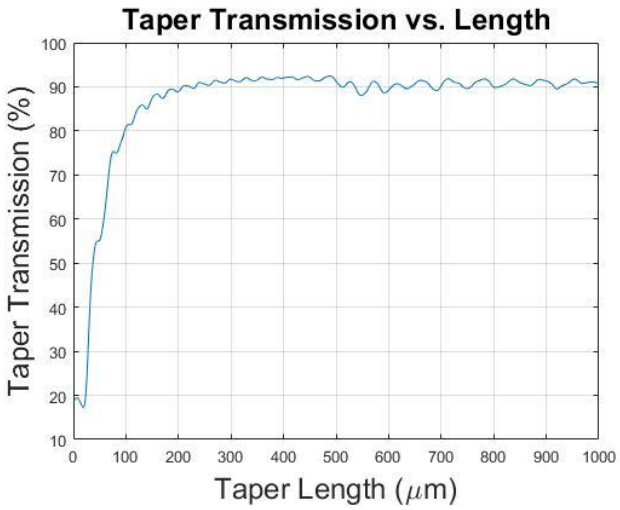

(b)

Figure 72: (a) A taper structure converting mode from a 15 **µ**m grating to a 1**µ**m waveguide. (b) A plot of taper transmission vs. length that shows 90% transmission with a taper length greater than 200 **µ**m.

Finally we design a disk radius for the resonator and a gap width between the resonator and waveguide. Because we desire to define the waveguide using photolithography, we keep its width no narrower than 1 µm. Based on this parameter, we design a disk radius and width such that there is minimal transmission at the waveguide output at the resonant wavelengths. Figure 73a shows the power distribution during critical coupling with disk radius of 11 µm and gap

width of 100 nm. We note this gap distance is only an estimate of a good starting point for fabrication of actual devices due to the fact that not all loss mechanisms can be included in simulations. Therefore, we pick a range of gap distances ±30 nm of 100 nm during fabrication. The device that exhibited critical coupling in our experiment has a gap distance of 113.7 nm. For easier reference, we label this device as nominally having an "100 nm" gap.

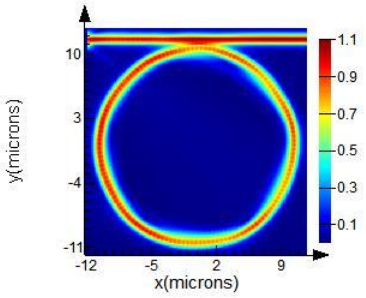

(a)

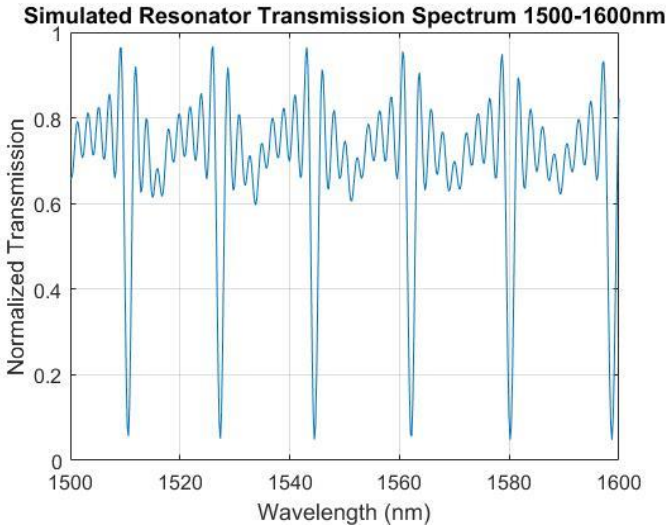

(b)

Figure 73: (a) Critical coupling observed with disk resonator radius of 11 μm and coupling gap of 100 nm, 1μm wide and 500 nm thick waveguide. (b) Six resonant modes observed between 1500 and 1600 nm. Ripple artifacts are due to fields not having fully decayed in simulation.

In Figure 73b, six resonant wavelengths can be observed between 1500-1600 nm in a plot of transmission vs. wavelength. The ripple artifacts are due to fields not having fully decayed in simulation. These resonant wavelengths correspond to mode orders 78-83 and can be calculated analytically using eq. (2.5.1) without the factor of ½. This is because the mode acts as a whispering gallery mode travelling around the circumference of the disk instead of between 2 mirrors in a Fabry Perot cavity.

5.2 Fabrication and Testing Setup

The feasibility of the waveguide-resonator-NFT system depends on the ability to place all the components on the same level as the laser gain medium. If there is misalignment, then we are losing light we otherwise could have coupled into the NFT. In Chapter 3 we discussed placing the mode stabilizing structures (MSS) next to the gain medium in the same fashion. Using these fabrication steps, we first demonstrate how the laser can be integrated with the waveguide-resonator-NFT system. Then we fabricate our actual system on a Si wafer (as opposed to GaAs) and test it using an external tunable laser.

In demonstrating the feasibility of laser integration with waveguide, all the fabrication steps are the same as described in Section 3.2 up to the part of placing the MSS next to the laser gain medium. Now instead of the MSS, we deposit a layer of Si_3N_4 and pattern it with photolithography into a waveguide. The result is shown in an SEM image in Figure 74.

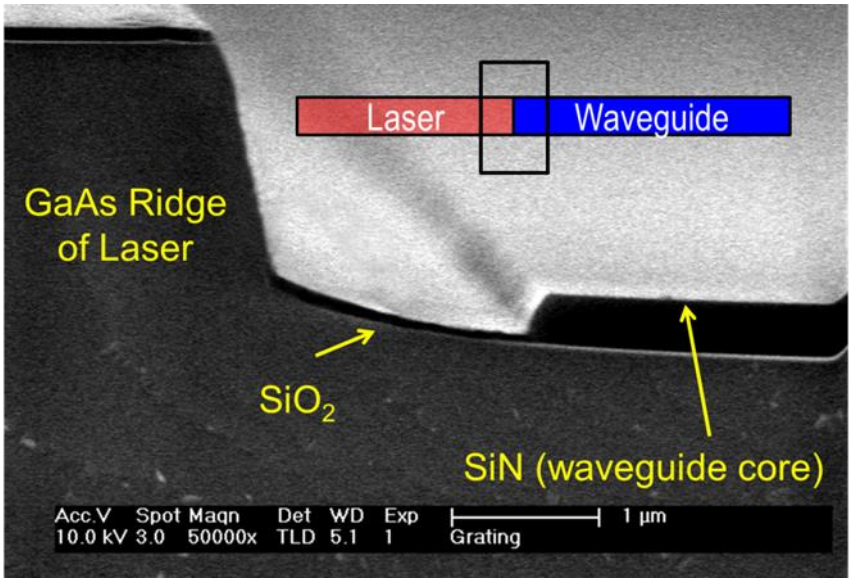

Figure 74: SEM cross section image of Si_3N_4 waveguide core placed in proximity of GaAs ridge of the laser. It is raised to the level of the gain medium with a sputtered layer of SiO_2, similar to the placement of the MSS.

In the SEM image, we show a Si_3N_4 waveguide placed within 1 µm of the GaAs laser ridge, which is a distance to achieve reasonable coupling [112]. A sputtered layer of SiO_2 controls its vertical placement in the same way it controls that of the MSS.

As mentioned previously, we will not test our system using the on-chip laser but instead with an external tunable laser. This setup requires that we couple light from the tunable laser into our waveguide using a grating coupler. An additional output coupler is required for detection by power meter. Due to the setup of our fiber, we will build the waveguide in a U-shape. We start our process on a Si wafer with a ~1 µm layer of native oxide. A 500 nm thick Si_3N_4 layer is sputter deposited. Using the fabrication steps described in Section 3.2, we define the waveguide and 11 µm radius resonator via photolithography and etch them through RIE. We use ebeam lithography to define the gap between resonator and waveguide and etch it again through RIE.

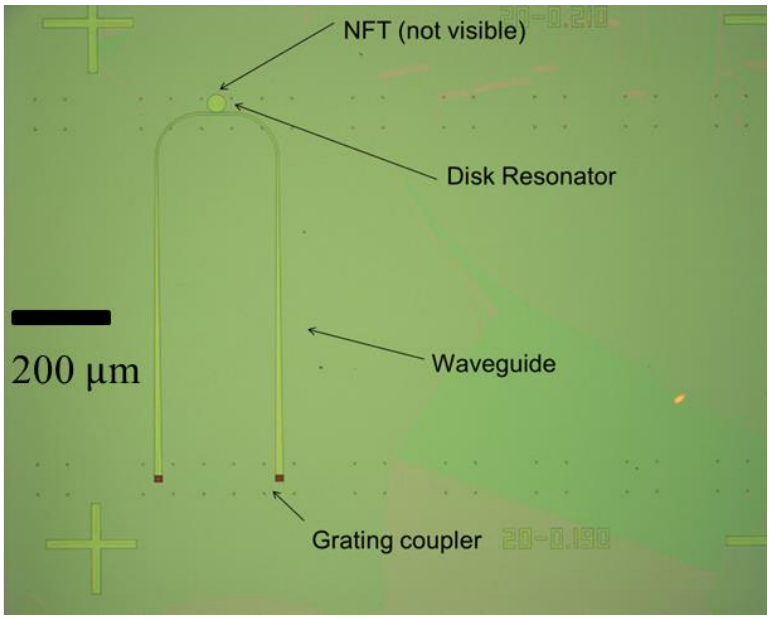

(a)

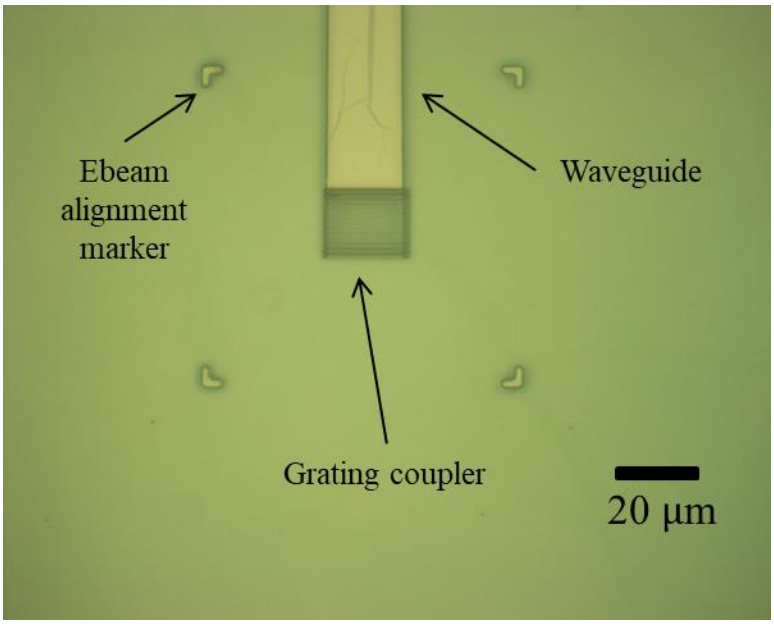

(b)

Figure 75: (a) Top view of waveguide-resonator-NFT system. The NFT along with its probe pads are not shown. (b) Zoomed in view of grating coupler.

A second ebeam step is used to define the NFT. We deposit 5 nm Ti for adhesion and 50 nm Au for the NFT in an ebeam evaporator and use PMMA for liftoff. The result is shown in Figure 75.

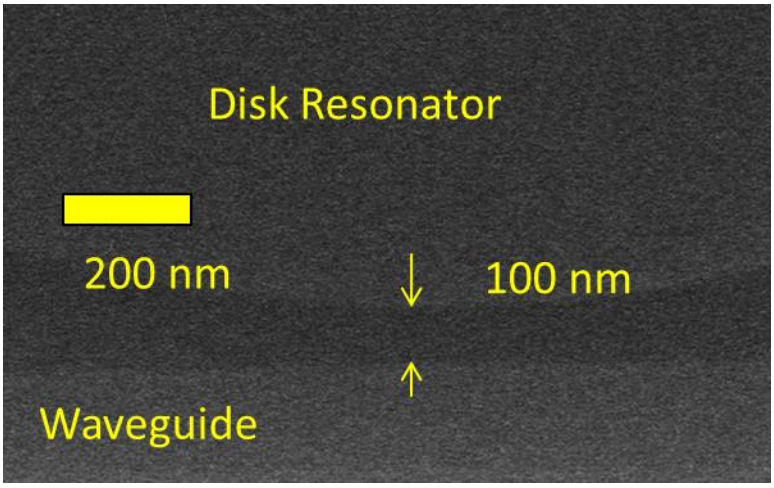

(a)

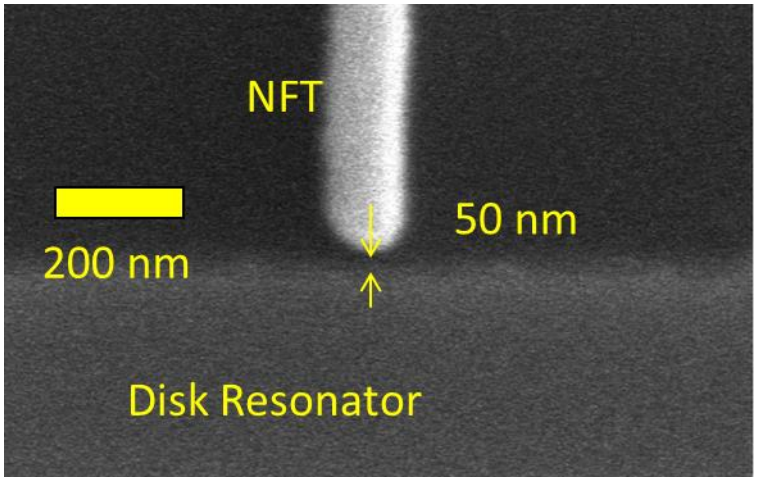

(b)

Figure 76: (a) Zoomed in view of 100 nm coupling gap between resonator and waveguide. (b) Zoomed in view of NFT next to disk resonator with 50 nm gap.

Figure 75a shows a top view of the U-shaped waveguide along with the resonator. The NFT is too small to see in this image. Figure 75b shows a zoomed in view of one of the grating

couplers. The L-shaped structures around the grating serve as markers during ebeam alignment. We show zoomed in views of the resonator coupling gap to waveguide and NFT next to resonator respectively in Figure 76a and Figure 76b. Although our system is technically complete at this point, we still need to perform additional steps to have the ability to test our system as currently there is no way for us to probe the NFT.

The next step is to deposit a 400 nm layer of PECVD oxide for electrical insulation, then use photolithography and RIE to define a via through the oxide. We sputter deposit Ti/Pt/Au in the same way for our lasers and liftoff the metal using Remover PG 1165. Figure 77a shows a cross section of the resonator made of Si_3N_4 along with the Ti/Au NFT. Figure 77b shows a top view of the NFT with probe pads connected. We discuss the reasons for picking the dimensions in Section 5.4.

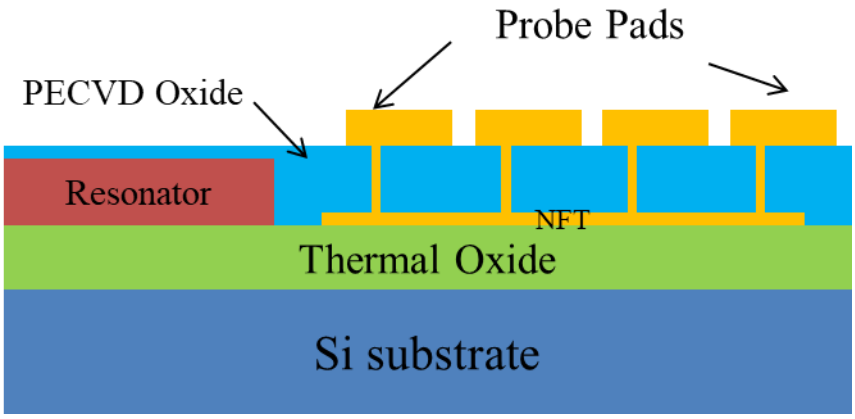

(a)

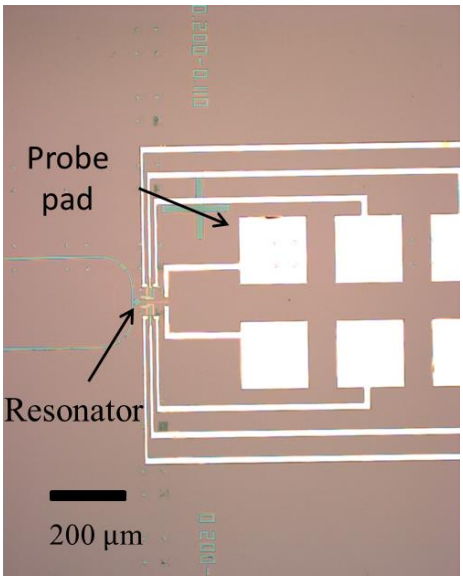

(b)

Figure 77: (a) Cross section of the waveguide-resonator-NFT system. Via's are made through a layer of insulating PECVD oxide to probe the NFT. (b) Top view of NFT with probe pads.

With a completed waveguide-resonator-NFT system, we are ready for testing. Figure 78a shows a block diagram of our testing setup and Figure 78b is a photograph showing the actual setup. It consists of a TSL-510 tunable laser as the light source around 1550nm. The fiber output from the laser goes through a polarization controller into one of the grating couplers. The second coupler serves as an output to a fiber leading into a power meter. A source meter provides a current source and lock-in measures. The laser and power meter are connected via GPIB to a computer with LabView while the lock-in is controlled with the manufacturer's specialized software. We automate the optical measurements with LabView to obtain plots of transmission vs. wavelength. The lock-in allows us to measure voltage amplitude and phase. Thus, the measurements are divided into optical and thermal, which we respectively discuss in Sections 5.3 and 5.4.

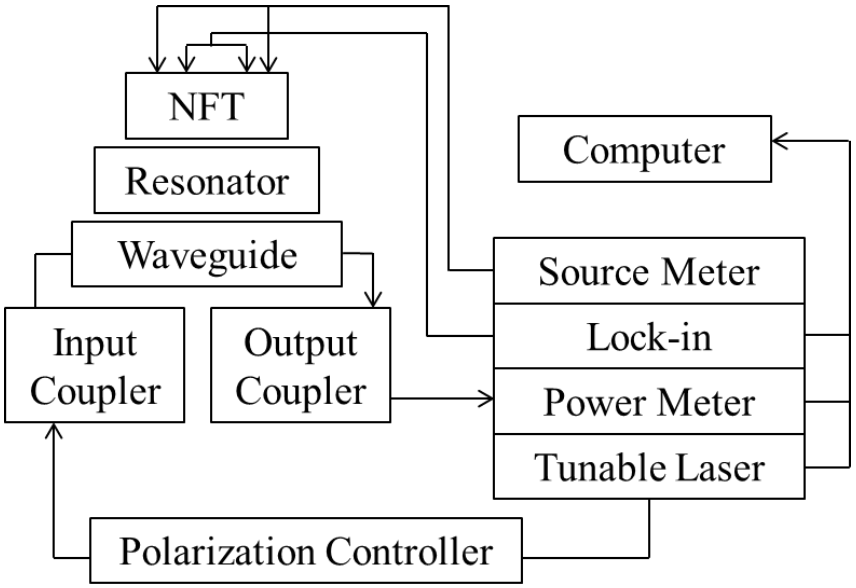

(a)

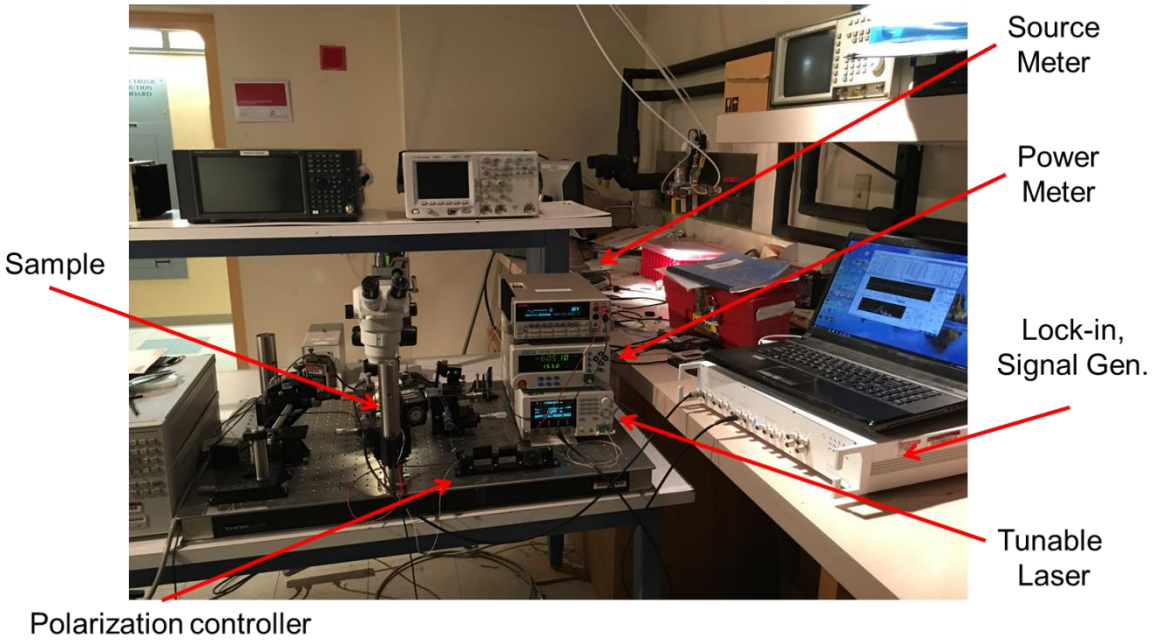

(b)

Figure 78: (a) Block diagram of our testing setup (microscope not shown). (b) Photograph of our testing setup.

5.3 Optical Measurements: Using Resonator as Sensor

Using the setup shown in Figure 78b, we examine the optical behavior of the resonator-NFT system through the transmission spectrum at the waveguide output. We align the tunable laser to the grating coupler by maximizing the power output at a non-resonant wavelength. In this case, we pick 1550 nm. For reasons unknown at this time, the grating coupling efficiency is much lower than predicted by simulation, resulting in insertion loss of more than -20 dB per grating. This work does not aim to improve the grating coupling efficiency, but we speculate two factors may be responsible: grating directionality and mode mismatch. If the grating directionality is low, then a beam coupling from the waveguide to a fiber will result in a large percentage being diffracted toward the substrate instead of being sent into the fiber. In the case of mode mismatch, the optical intensity profile of the grating has an exponential decay shape while the mode profile of standard optical fibers is Gaussian, resulting in reduced overlap integral [113]. Nevertheless, we are still able to characterize the operation of the resonator through spectra collected at the waveguide output.

Figure 79 shows plots of normalized transmission vs. wavelength, with the tunable laser sweeping from 1500 to 1600 nm. We use Figure 79a as a reference case where a resonator is placed 100 nm away from the waveguide with no NFT present in its vicinity. The locations where minima occur signify the resonant modes, as nearly all of the power in the waveguide couples into the resonator. These modes correspond to the ones obtained through simulation.

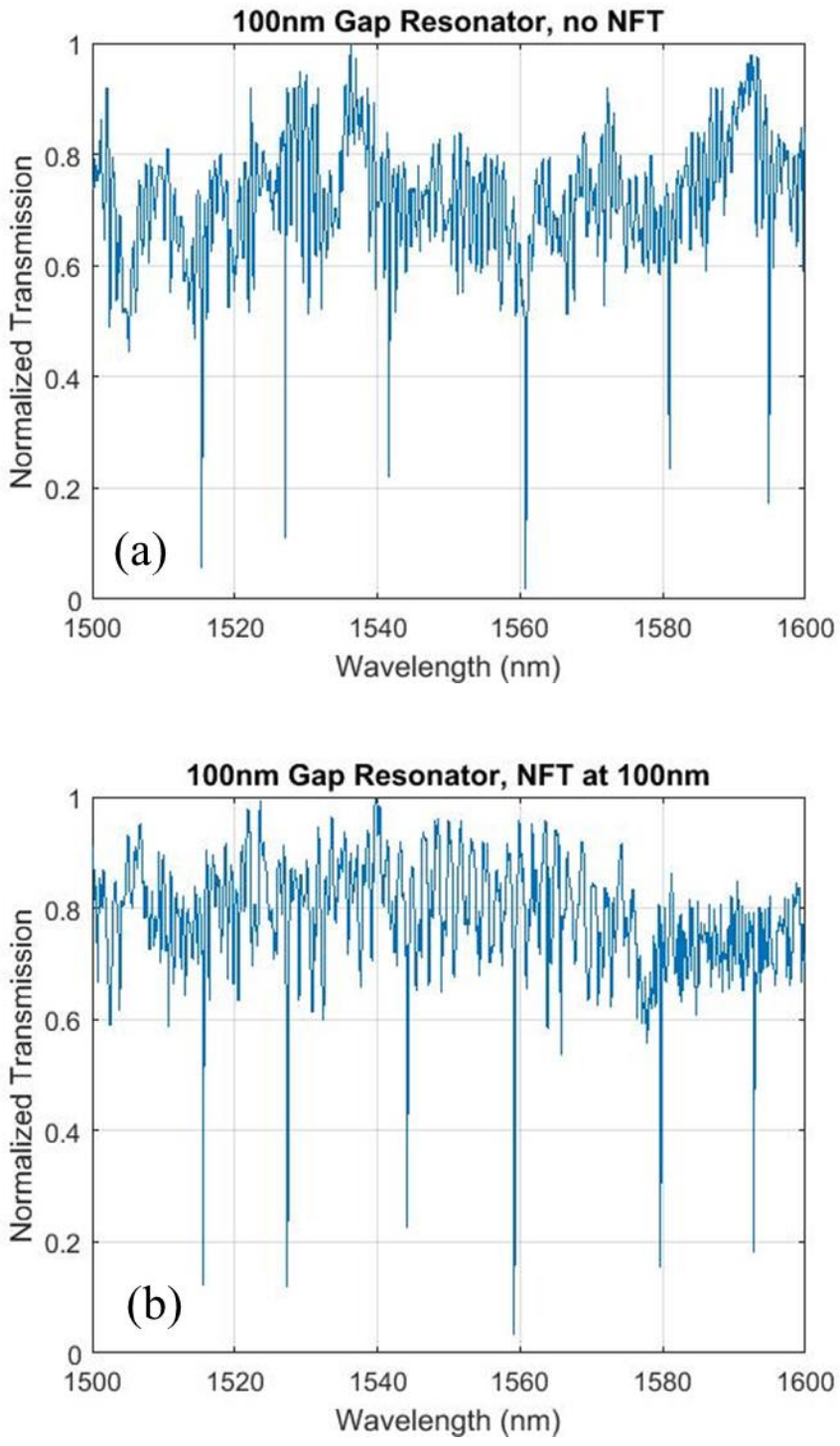

Figure 79: Plots of normalized transmission vs. wavelength for resonator 100 nm away from waveguide: (a) No NFT present next to resonator and (b) NFT present 100 nm away from NFT.

In Figure 79b, we show the transmission spectrum of a resonator with a NFT placed 100 nm away. The gap between the waveguide and the resonator is also fixed at 100 nm. Comparison the two spectra, there are no appreciable differences between the wavelengths of the resonant modes. This is not surprising as the NFT only acts as a small perturbation on the system. However, this perturbation may be enough to affect the extinction ratios of these modes as they have different minima compared to that of the resonator without NFT.

We now analyze the effect of NFT coupling on the Q of the resonator. Shown in Figure 80, the same resonant mode of 3 devices is compared: one with resonator and no NFT, the second with NFT 100 nm away, and the third with NFT placed 50 nm away. The coupling gap between waveguide and resonator is fixed at 100 nm.

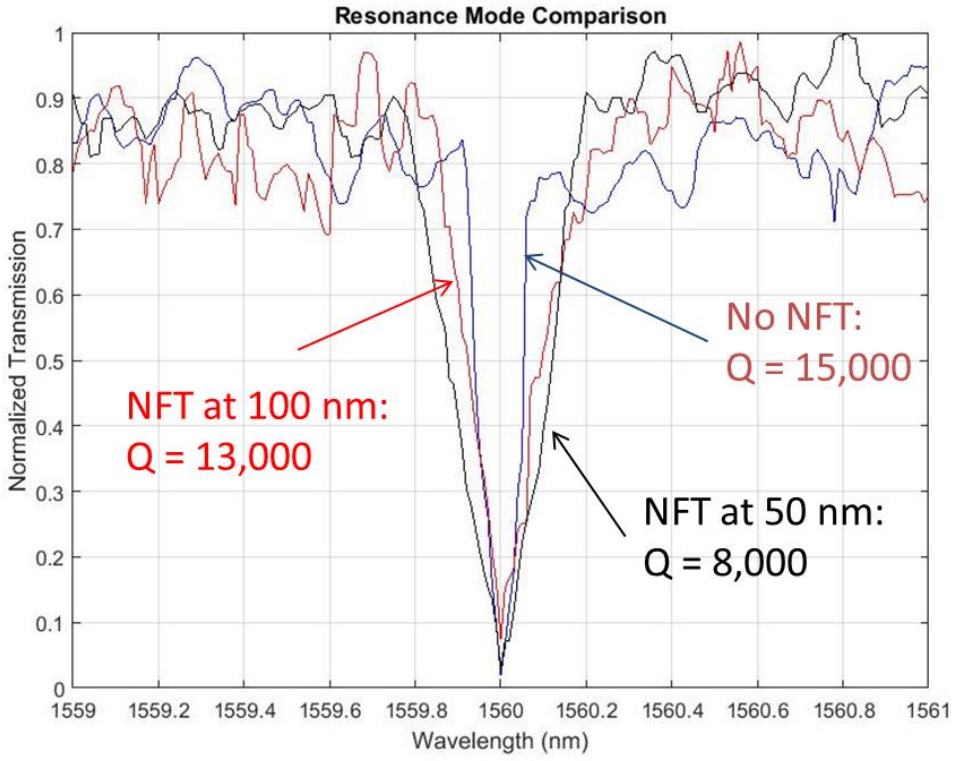

Figure 80: Plot of zoomed in resonance mode. The Q decreases with proximity of NFT.

For ease of comparison, the resonant modes have been adjusted so that they occur at exactly 1560 nm, since experimental variation has shown there to be 1-2 nm differences in the same mode. Using eq. (1.5.1) to calculate Q, we find that for the case without NFT the Q is about 15,000. For NFT at 100 nm and 50 nm, the Q is respectively 13,000 and 8,000. We note that measuring a Q of 15,000 is well within our laser's (Santec TSL-510) capabilities since it has been used to measure Q's up to 10^7 [114].

The Q of the resonator appears to decrease with an increase in NFT proximity. The Q decrease also correlates with the amount of energy coupled into the NFT. For example, when Q goes from 15,000 to 8,000, it signifies almost 50% of its stored energy has been transferred to the NFT at 50 nm away. If we want the NFT to be more insensitive to placement, i.e. not affect Q with coupling distance, then we would need a higher Q resonator. The behavior of the resonator Q can be verified using the following relationships [115] [116]:

$$Finesse = \frac{2\pi}{1-p} \quad (5.3.1)$$

$$FSR = \frac{c}{n_g \cdot 2\pi r} \quad (5.3.2)$$

$$Q = \frac{Finesse \times frequency}{FSR} \quad (5.3.3)$$

where p is the round trip losses in the resonator, FSR is the free spectral range (distance between adjacent resonant modes), n_g is the group index, c is the speed of light, and r is the disk resonator radius. Using eq. (5.3.1), the finesse for a round-trip loss of 5% is found to be 126. Given our material is Si_3N_4 and we are examining resonant modes in the 1500-1600 nm range,

eq. (5.3.2) results in a FSR of 2.17 THz. Finally, using eq. (5.3.3) we find a Q of 11,000 which is roughly comparable to a NFT coupling between 50-100 nm away.

We note here that our initial goal was to design a resonator with a high enough Q such that the NFT will act as the dominant loss in the system. This way the NFT can be relatively insensitive to placement. However, the data shown above clearly indicates that a difference of a few tens of nanometers can drastically affect the resonator Q. This signals that the Q is not high enough and the resonator loss is comparable to that of the NFT coupling interaction. A significant factor that can affect Q is the material quality of the resonator. Ours is made from sputter deposition of Si_3N_4, but much higher Q's have been achieved with this material in literature using other deposition methods such as low pressure chemical vapor deposition (LPCVD) and liquid source chemical vapor deposition (LSCVD) [117] [118]. Other methods to improve Q include making an undercut structure to prevent mode leakage into the substrate and surface tension reshaping in which the resonator undergoes thermal treatment to achieve a smooth surface [119]. These methods are promising leads in raising the Q of our resonator.

5.4 Thermal Measurements: Confirm NFT Mode Propagation

So far we have shown that the presence of the NFT can be detected from the optical behavior of the resonator, in particular the decrease in Q from increased NFT coupling interaction. In this section, we demonstrate the launch of plasmonic modes on the NFT using thermal characterization. We aid our explanation with Figure 81. Consider our external laser being pulsed and maximum power is being coupled into the NFT when the wavelength is tuned to one of the resonant modes of the resonator. This power will turn into heat which propagates down the NFT, and the propagation length δ indicates whether the power is being dissipated thermally (short δ) or carried by a launched optical mode (long δ). If we examine the

temperature profiles at various locations along the NFT, we can determine a δ based on the behavior of the temperature amplitude and phase lag relative to the laser pulse frequency. Generally, the amplitude decreases and the phase lag increases as distance from the NFT coupling origin is increased and δ is decreased. In practice, we will not measure temperature directly and instead measure changes in resistance which is a function of temperature.

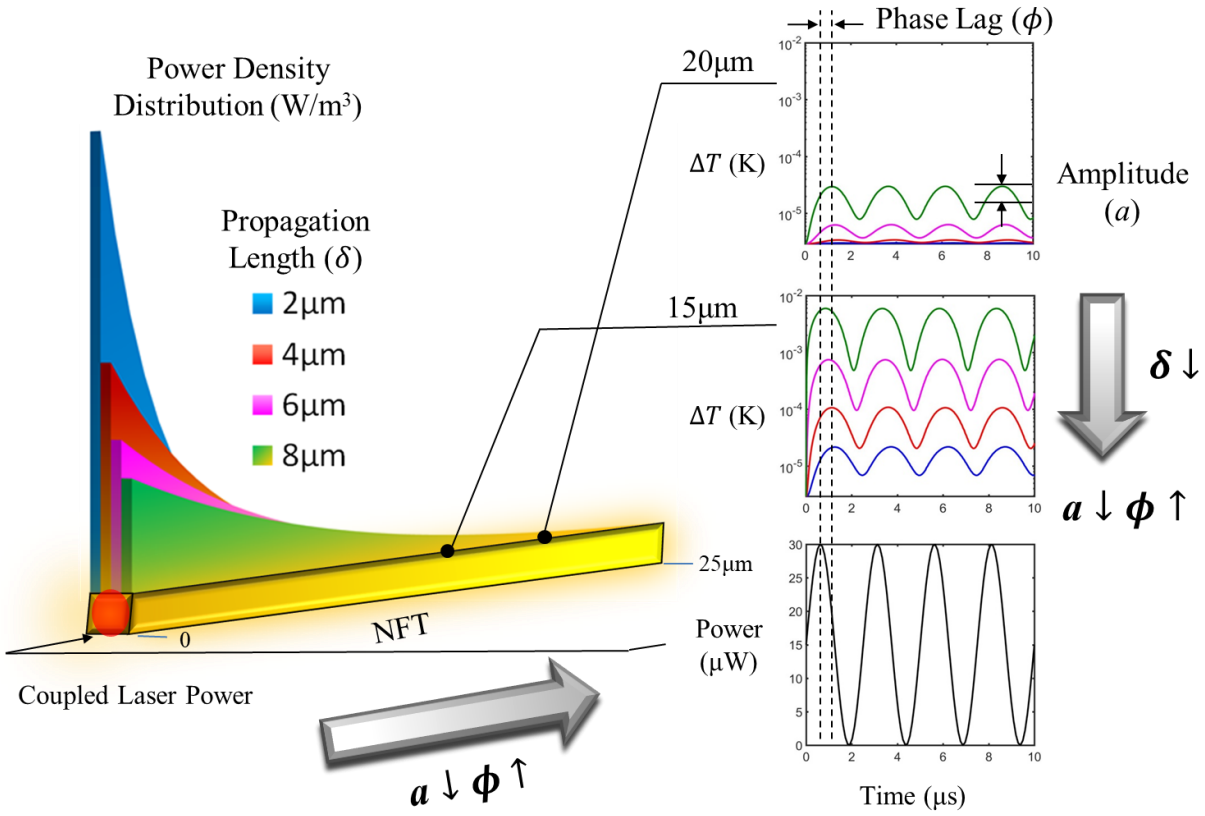

Figure 81: Power from a pulsed laser couples into the NFT at resonance which turns into heat. The propagation length of this heat indicates whether the coupled power is being dissipated thermally (short $\boldsymbol{\delta}$) or carried by a launched optical mode (long $\boldsymbol{\delta}$). The temperature profile is shown at 15 and 25 μm. We can use the amplitude and phase lag information of the temperature to determine a propagation length and thus prove that an optical mode has been launched. The amplitude decreases and the phase lag increases as distance from coupling origin is increased and $\boldsymbol{\delta}$ is decreased.

The propagation length δ of the plamonic mode power can be calculated according to:

$$\delta = \frac{\lambda_0}{4\pi k} \quad (5.4.1)$$

where k is the imaginary component of the effective mode index. The expected mode profile is shown in Figure 82a with effective mode index n = 1.64-0.016j. The E field propagates along the 4 corners of the NFT while a circumferential H field exists counter clockwise. The decay length is calculated to be δ = 8 μm. Other modes may be supported by the NFT (which we will designate as "transverse dipole modes") as shown in Figure 82b and Figure 82c. However, the E and H fields of these modes do not align well with those of the propagating mode in the resonator. Thus, we expect that the mode that will be launched with greatest efficiency on the NFT is the first with the circumferential H field.

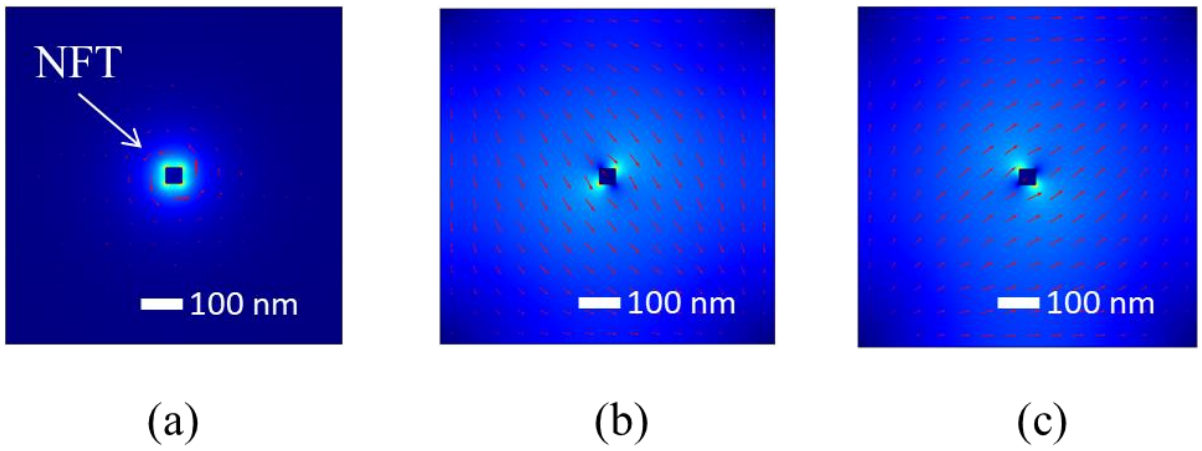

Figure 82: NFT mode profiles: (a) E field along 4 corners of NFT and counter clockwise circumferential H field. (b) Transverse dipole mode with E field at bottom left and upper right corners and diagonal H field pointing to bottom right. (c) Transverse dipole mode with E field at upper left and bottom right corners and diagonal H field pointing to upper right.

Temperature rise in the NFT will be reflected as a change in resistance R, since

$$R = \frac{\rho L}{A} \quad (5.4.2)$$

where ρ is resistivity, L is length, and A is the cross section area and change in resistivity can be expressed as:

$$\Delta\rho = \alpha \cdot \Delta T \cdot \rho_0 \quad (5.4.3)$$

where α is the temperature coefficient of resistance (TCR), ΔT is the change in temperature, and ρ_0 is the initial resistivity. We do not endeavor to measure resistance at DC since any changes will be too small to detect. Because of our low grating coupling efficiency, we only expect a small portion of the light from the tunable laser to couple into the resonator and therefore the NFT. However, if we pulse the laser using a sinusoidal modulation, we can use a lock-in amplifier to measure AC voltage amplitude to indirectly detect the change in resistance. We set up our lock-in and current source in a 4-point configuration in a region spanning from 5-15 μm as shown in Figure 83. For the lock-in, we use the HF2 model from Zurich Instruments which has a dynamic reserve of 120 dB [120]. This means that the lock-in can extract a signal in the presence of noise one million times higher in amplitude than the signal of interest.

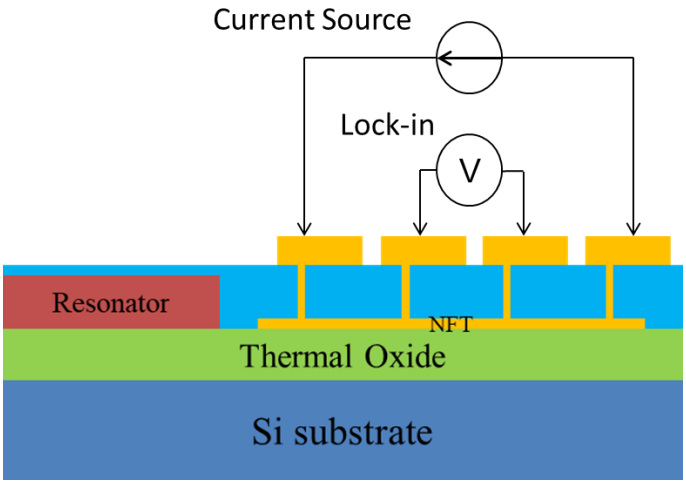

Figure 83: Diagram of 4-point test setup to measure AC voltage amplitude using a lock-in amplifier.

One concern using this setup is the metal leads interferring with optical proagation. We show in Figure 84 mode propagation along the NFT in the presence of a metal lead protruding out of the side at 10 μm. The resonator is modeled as a section of waveguide. A mode is launched on the NFT with E field normal propagation shown. The field propagates past the point with the metal lead. Power dissipated integration calculations in subsequent sections of the NFT show minimal change with and without the metal lead. Thus, we can still use them to make our thermal measurements.

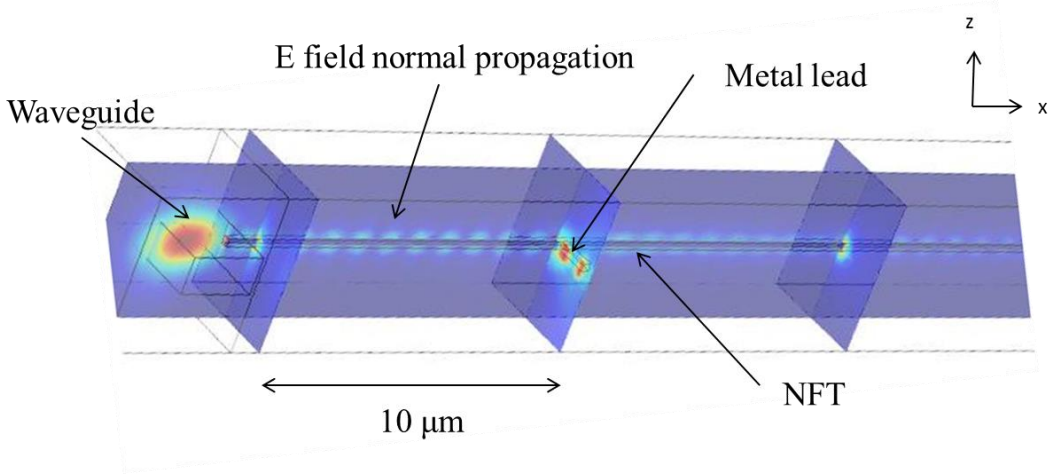

Figure 84: The NFT couples to the resonator which is modeled as a section of waveguide. Optical modes are launched in the NFT with yz slice showing E field propagation. A metal lead juts out at 10 μm but does not prevent E field from propagating past that point.

We also use this model to get a sense of what happens when the medium is placed at the end of the NFT. As mentioned previously, efficiently coupling to the NFT involves an impedance matching problem with the medium as its presence changes the termination condition on the NFT. To approximate its presence, we examine the NFT coupling behavior by changing its length. A plot of the percentage of the total power in the waveguide dissipated per length vs. the NFT length is shown in Figure 85.

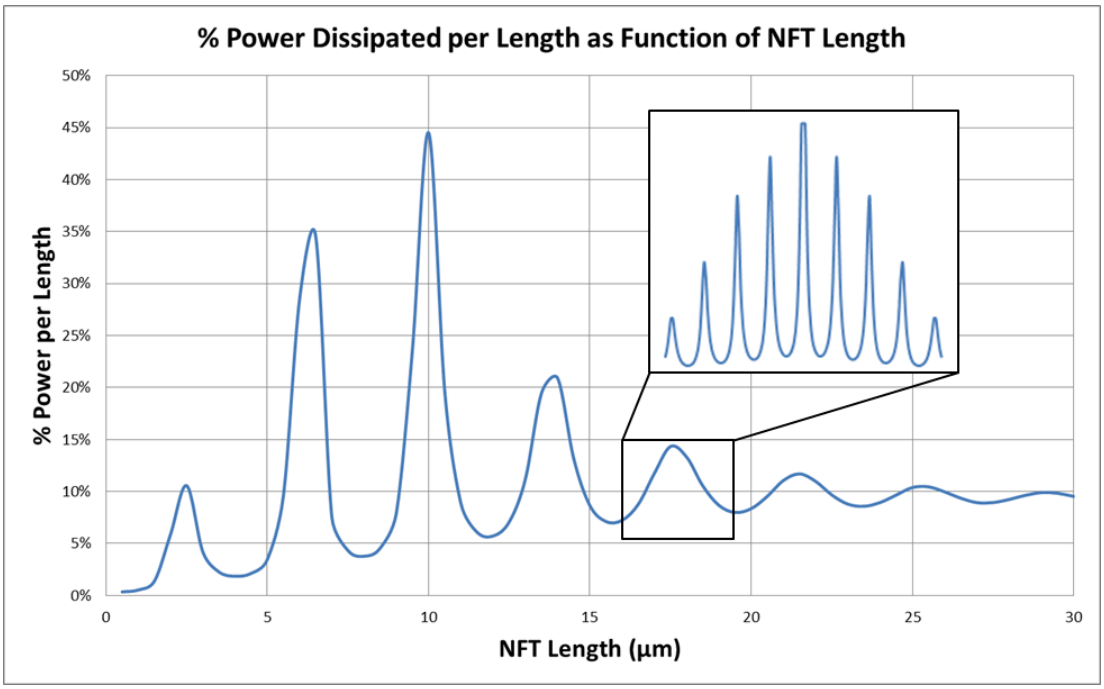

Figure 85: A plot of percentage power dissipated in the NFT per length vs. NFT length. The appearance of the peaks has to do with reflections from the end of the NFT. When the NFT increases in length, the reflections decrease and gradually disappear. A zoomed in view shows that each peak is an envelope of finer spaced smaller peaks.

The peaks are present due to the reflections from the NFT end, and this is representative of poor impedance matching with the medium. Note that a zoomed in view shows a peak is actually an envelpe of finer spaced smaller peaks, and we neglect to show these for the entire graph due to simulation time. As the NFT increases in length past 20 μm, the amount of reflections decrease and gradually disappear. In reality a NFT will be much less than 20 μm in length. However, one can still design the NFT length such that the power dissipated per length will fall on a minimum (valley between 2 peaks) rather than a maximum (peak).

Using the setup in Figure 78b, we set the current source to 100 μA and laser to 15 mW. We pulse the laser with a sinusoidal waveform at 100 KHz such that there is a peak-to-peak amplitude of 30 mW ($\pm$15 mW swing). The current source and laser power values are picked to

assist in achieving AC voltage values that are measureable without the system overheating. The frequency is chosen for purposes of phase analysis which will be explained later on in this section. Probes are landed in a 4-point configuration as shown in Figure 83. Using the resonator transmission spectrum as a guide, the laser is tuned to the wavelength of a resonant mode such that the system is in a state of critical coupling. We set the lock-in demodulator to the same pulse frequency and obtain AC voltage amplitudes and phase. We will analyze our results using COMSOL modeling.

We set up our simulation in COMSOL using a NFT with the same dimensions as in our experiment as well as thermal conductivity, which can be found from the Wiedemann-Franz Law. This law states that the ratio of thermal conductivity *k* of a material and its electrical resistivity σ is directly proportional to temperature *T*:

$$\frac{k}{\sigma} = LT \quad (5.4.4)$$

where *L* is the Lorenz number with a value of 2.44 x 10^{-8} $\mathrm{W \cdot \Omega \cdot K^{-2}}$. Using eq. (5.4.2) and eq. (5.4.3) we calculate the resistivity to be 3 x 10^{-8} Ω-m for a 10 μm long section and cross sectional area of 100 by 100 nm^2. Using eq. (5.4.4) at room temperature, we calculate a thermal conductivity value of 244 W/m-K for the NFT made of gold. As a reference, the bulk thermal conductivity value for Au is ~317 W/m-K [121].

In our model, a 1 μm thick layer of thermal oxide surrounds the NFT. We use the bulk thermal conductivity value of 1.4 W/m-K for the oxide at this thickness as suggested by the data of Yamane *et al.* [122]. The oxide thermal conductivity is not expected to decrease below 0.5 W/m-K even for thin films. We have verified that the variation of 0.5-1.4 W/m-K does not significantly impact our simulation results.

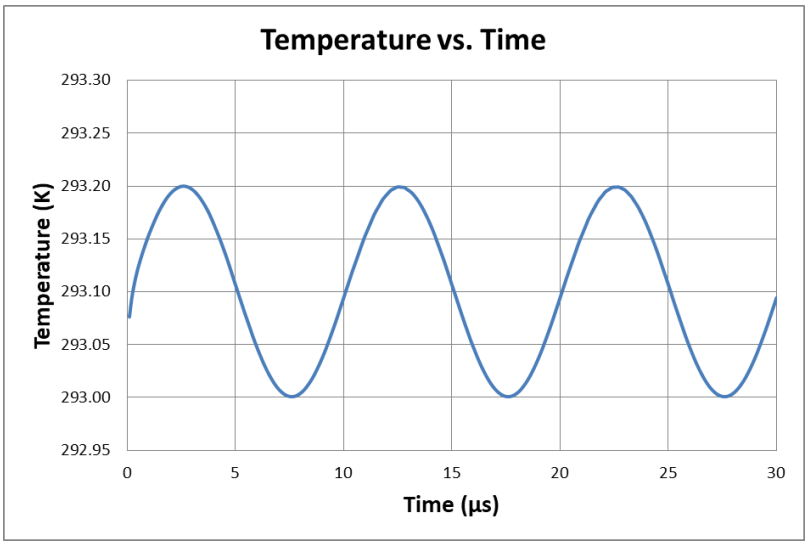

(a)

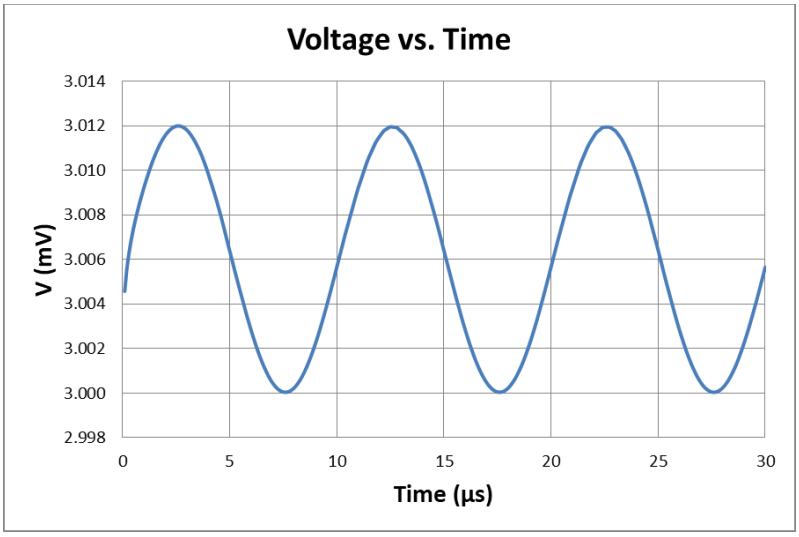

(b)

Figure 86: Simulated first 3 periods of (a) temperature vs. time and (b) voltage vs. time at 15 µm with frequency set to 100 KHz.

We create an exponentially decaying sinusoidal heat source due to optical propagation distributed along the entire length of the NFT in the z-direction:

$$P(z) = P_0 e^{-\frac{z}{\delta}}(1 + \sin(\omega t)) \quad (5.4.5)$$

where P_0 is the initial volumetric power density we arbitrarily set big enough to have significant changes in the NFT temperature in the locations of interest and δ is the decay length of the optical wave. A 100 μA current source is inserted, and a TCR value of 0.0034/K is used to couple the heat transfer and electric currents physics modules of COMSOL.

The boundary conditions of the model include setting the ends of the NFT and the edge of the oxide (1 μm away from the NFT) at room temperature and to be electrically insulated. We neglected to put a thermal interface resistance condition between the NFT and the oxide, which causes the results in this section to underestimate the real propagation length due to heat being able to spread into the oxide without any resistance in our model. We show sample plots of temperature and voltage as a function of time in Figure 86 taken at 15 μm and frequency set to 100 KHz with a δ of 8 μm as calculated by eq. (5.4.1). The values are scaled to be simliar to those found in our experiment.

For our measurements, we use 100 KHz and 400 KHz as frequencies to modulate the laser. We justifiy this choice by examining phase vs. frequency as shown in Figure 87a. In the plot of phase lag vs. frequency, phase lag only becomes more noticeable past 100 KHz. The upper limit of 400 KHz is chosen because that is the max modulation frequency setting of our tunable laser. In Figure 87b, we verify that the frequency range of 100-400 KHz will have sufficient thermal penetration depth in our gold NFT (>15 μm) so that we do expect temperature change at the probing regions of 5-15 μm and 15-25 μm (note we label the probe location with

the upper limit of this range). In addition, the penetration depth in SiO_2 is found to be <1 μm past 100 KHz. Thus, the room temperature boundary condition we set on our oxide in the simulation model is valid.

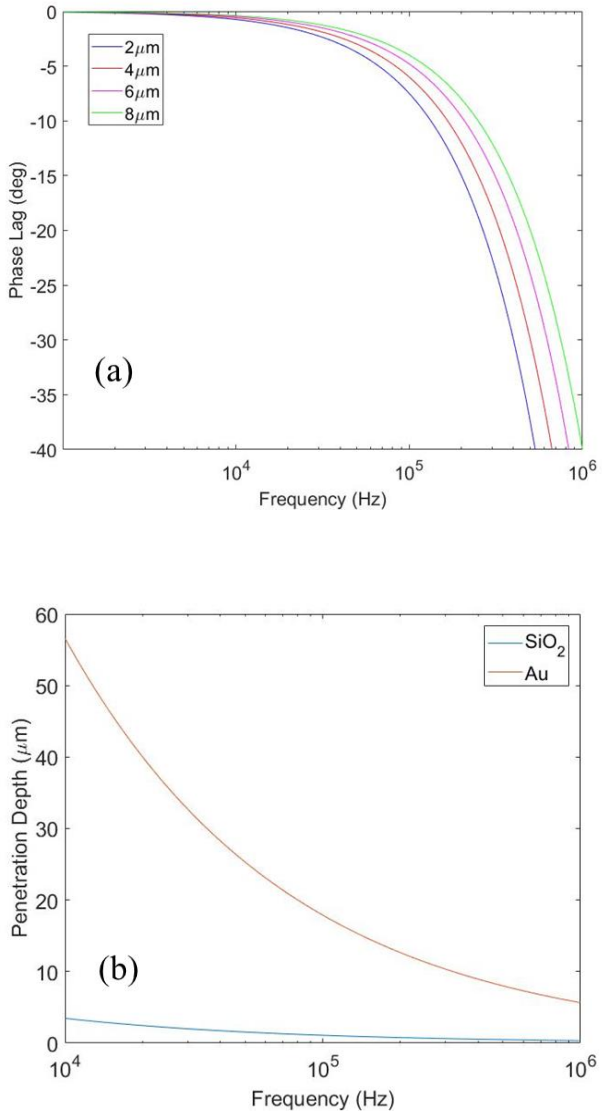

Figure 87; (a) Phase lag vs. frequency at 15 μm. Phase lag becomes more noticeable past 100 KHz. (b) Thermal penetration depth in Au (NFT) and SiO2 as a function of frequency. At 100 KHz, heat is still able to travel more than 15 μm in Au but is smaller than 1 μm in oxide. The oxide is thick enough to prevent heat from using it as a channel to spread into the substrate, verifying the temperature boundary condition we used in our model.

We first analyze our phase data by using our model to simulate contour curves of the phase lag as a function of the fraction of optical power into mode and the propagation length in Figure 88a at a single frequency and location (400 KHz, 15 μm). We have already discussed propagation length, but a high fraction of power into the optical mode is also convincing proof for launching the mode as that means the power is not being dissipated as heat.

We then take phase data at 2 different locations along the NFT (15 and 25 μm**)** with 2 different frequencies at each location (100 and 400 KHz). We generate a contour for each measured phase and plot them in Figure 88b. The intersection of these contours should tell us something about the characteristics of the launched mode since it has to remain constant across all measurements. In Figure 88b, the intersection of the contours show that we launched a mode with a propagation length of ~6 μm and over 50% of the coupled power into the NFT went into this mode instead of dissipating as heat. The propagation length of 6 μm is slightly different than the one calculated by eq. (5.4.1). This is most likely due to the fact that the width of the fabricated NFT is not exactly 100 nm which changes the mode index in the simulation from Figure 82a. For example, the sample could be underexposed and an 70 nm wide NFT will give a *k* of 0.0194, which results in a δ of 6.3 μm. A second factor is the optical conductivity for which we used the bulk value. In literature it has been shown that as the gold film thickness decreases the optical conductivity increases [123] and the electrical conductivity decreases [124]. Our experimental value for the electrical conductivity (3.33×10^7 S/m) is ~30% lower than the bulk value, and we estimate that the optical conductivity should have been 30% higher in our simulation. This new optical conductivity value gives a δ of 6.2 μm. Finally, a 2° phase error can easily account for this difference, and our measurements have an uncertainty of $\pm 1.5°$.

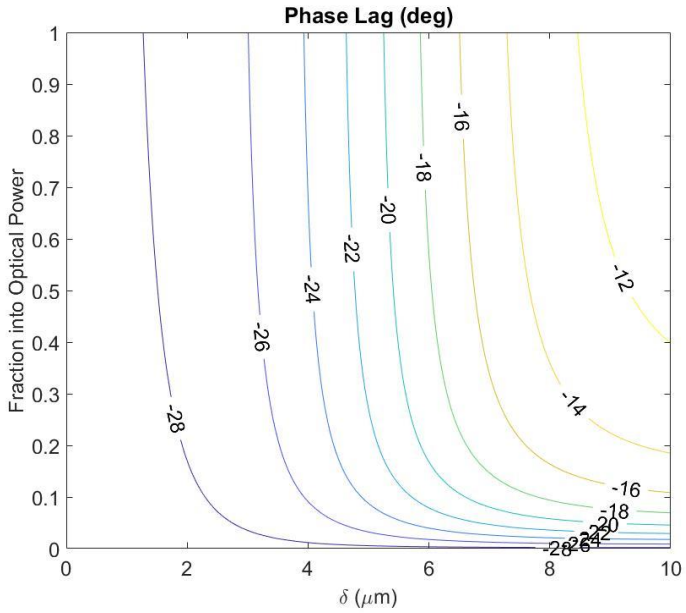

(a)

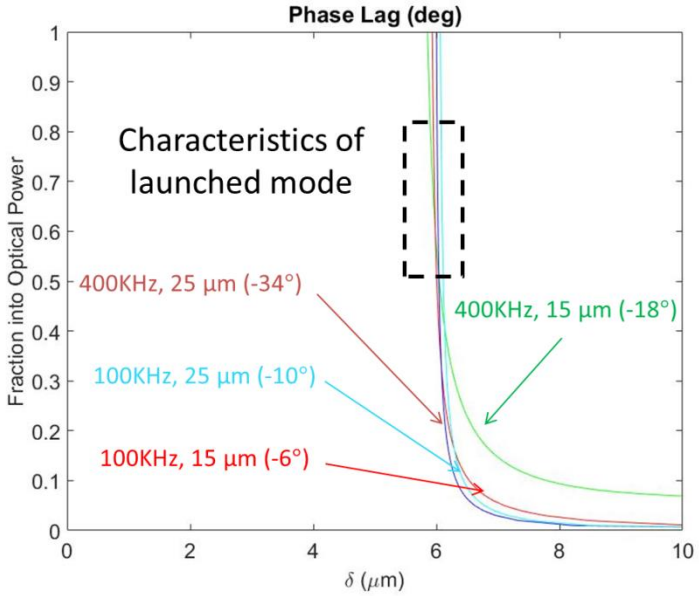

(b)

Figure 88: (a) Contour plot of phase lag at 400 KHz and 15 μm. Phase lag is a function of fraction into optical power and propagation length $\boldsymbol{\delta}$. (b) Experimental values for phase lag at 2 different frequencies at 2 different locations for a total of 4 phase contours. Their intersection shows that we launched a mode with $\boldsymbol{\delta \approx 6}$ μm and over 50% of the power coupling into this mode.

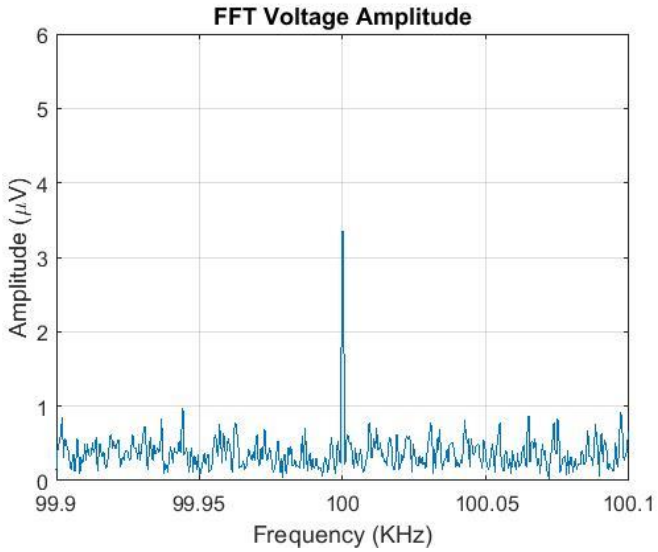

Figure 89: Fast fourier transform (FFT) of the AC voltage amplitude measured by lock-in at 15 μm and 100 KHz with 100 μA DC-sensing current source. The tunable laser is set to 15 mW with ±15 mW swing.

After determining a propagation length, we examine our amplitude data. The lock-in performs a fast fourier transform (FFT) on a measured waveform to clearly indicate the magnitude at the frequency of interest. The AC voltage amplitude at 15 μm is found to be 3.5 μV as shown in Figure 89. We use our measured amplitude to determine optical power into the NFT mode. We first use our simulation model to obtain a change of 0.09 K/μV and 19.3 μW/K in the region of interest. Given the amplitude is 3.5 μV, the power entering this region is 6.1 μW. Using a δ of 6 μm, the optical power entering at the NFT at the beginning is determined to be ~10 μW. The sensitivity of the voltage to δ is shown in Figure 90.

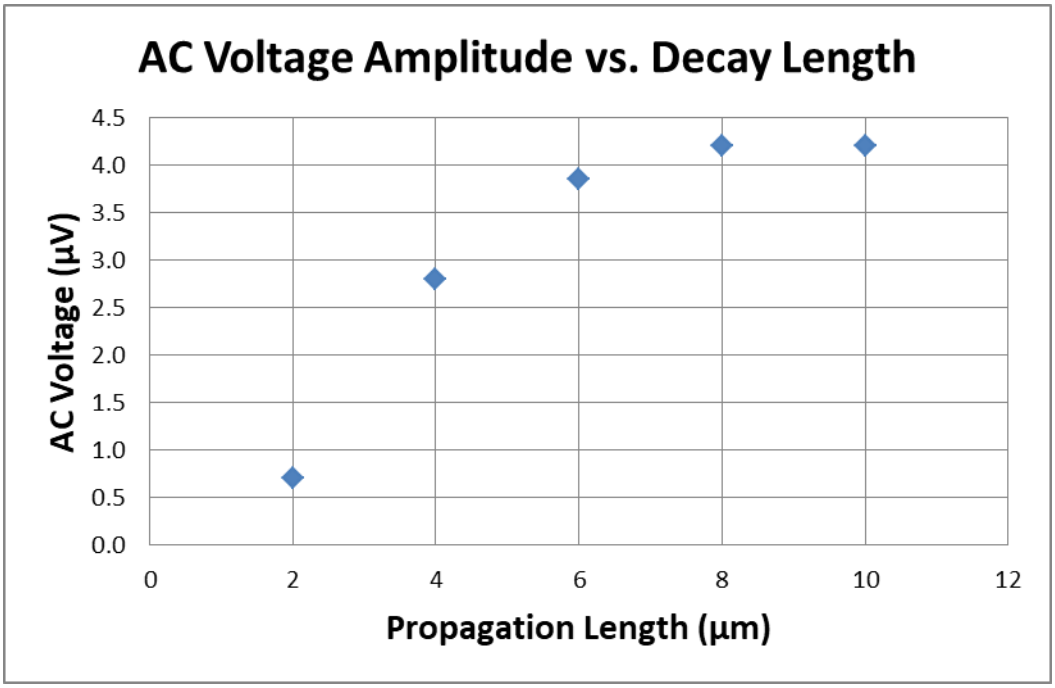

Figure 90: Plot of simulated AC voltage amplitude vs. decay length taken at 15 µm. Total distributed power in NFT is the same in all cases.

The AC voltage amplitude has a high sensitivity to changes in the propagation length below 6-8 µm. Our amplitude measurement indicates that we have a propagation length of at least 6 µm, which matches the length we determined from our phase measurements.

After determining we have launched the correct mode, we are interested in tracking the power flow in the system, in particular how much is scattered and how much is actually coupled into the NFT mode. We perform this analysis using first our experimental results followed by those from simulation. Experimentally, we estimate ~6 µW entering the region of interest (where we measure voltage) and that ~10 µW of optical power entered the NFT based on earlier discussion. If optical power makes up 50-80% of the total power, then the total power coupled to the NFT ranges from 12.5-20 µW. Due to a loss of 20 to 30 dB per grating, power coupled to the resonator can be 50 µW if we assume 25 dB loss average and laser AC power is 15 mW. This

also means the resonator has ~50 μW of output power available. Of this total power, 23 μW is estimated to be sent to the NFT because the resonator Q drops from 15,000 to 8,000 with the NFT at 50 nm away. Based on these calculations, the power breakdown is as follows: 13-46% resonator output power is scattered, 54-87% resonator output power is coupled into the NFT, and a net of 43% coupled resonator power is converted into the NFT mode.

For simulation, we use the same model shown in Figure 84 and redraw it from the top view as shown in Figure 91. We model a section of the resonator as a dielectric waveguide and create a standing wave in the cavity by launchin a 1W wave from each end, labelled as $P_{A,IN}$ and $P_{B,IN}$. We note that power exiting each end is 0.82W, labelled as $P_{A,OUT}$ and $P_{B,OUT}$. This means 0.36W is lost in one pass. Of this 0.36W, 0.25W passes through an integration plane along the entire length of the waveguide ($P_{Fullplane}$) and 0.19W passes through a plane along the length of the NFT mode ($P_{Partplane}$). The propagation power of this mode as a function of distance along the NFT is represented by P_{NFT}. Based on our 2D mode profile calculation for the NFT, we determine that the evanescent decay length is ~200 nm on each side of the wire (above and below the wire in Figure 91) . Based on these numbers, we determine that 31% of the output power is scattered and 53% is coupled into the NFT mode. This is in agreement with the power breakdown calculations from our experimental results.

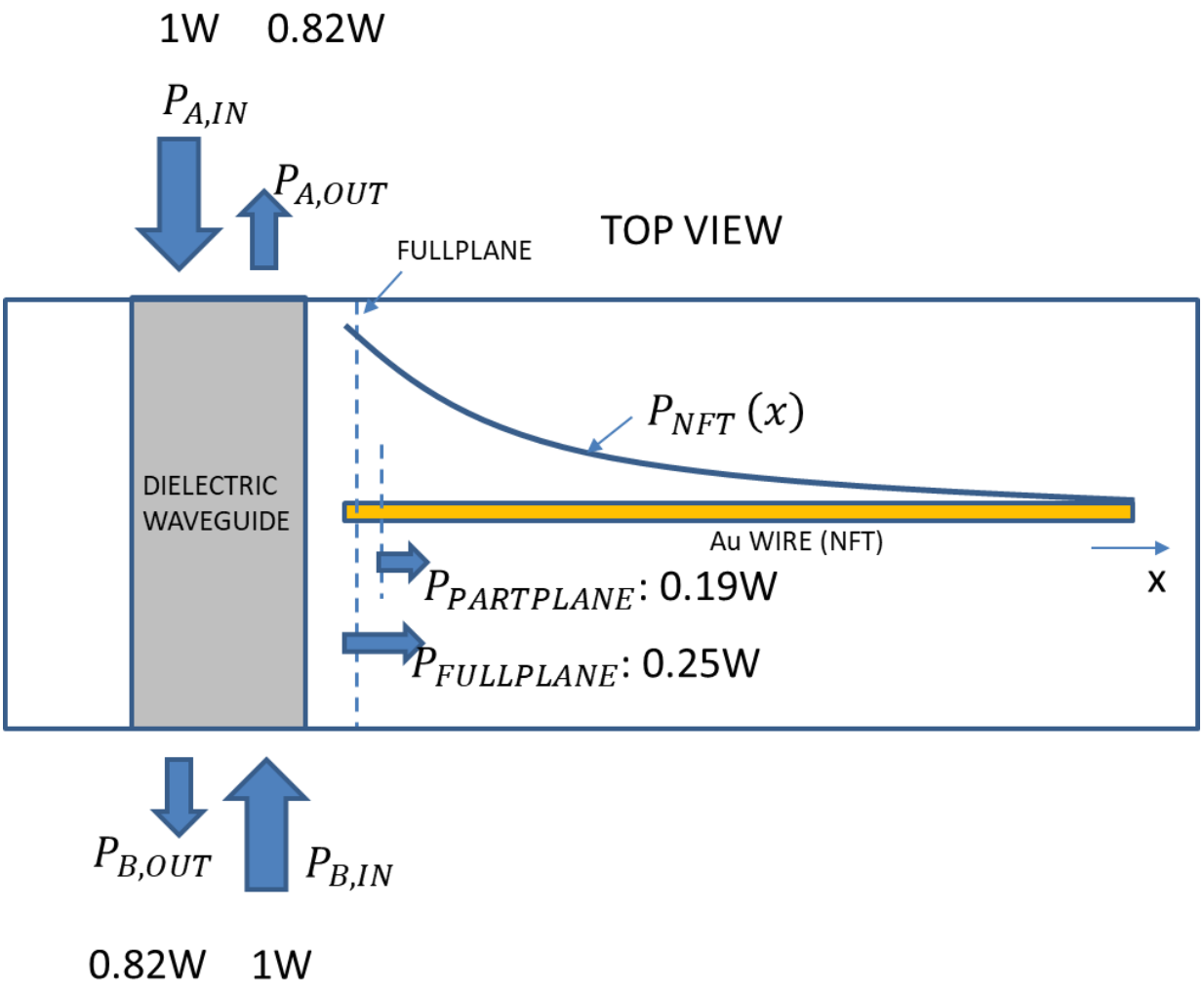

Figure 91: Our model used for simulations in Section 5.4 is redrawn in the top view to show the breakdown of power flow. A 1W wave is sent from each end of the dielectric waveguide to create a standing wave in the cavity and 0.82W exits each end. An integration plane along the entire side of the waveguide ($P_{Fullplane}$) shows 0.25W crossing and a part plane the width of the NFT mode ($P_{Partplane}$) shows 0.19W crossing. The propagation power of this mode as a function of distance along the NFT is represented by P_{NFT}.

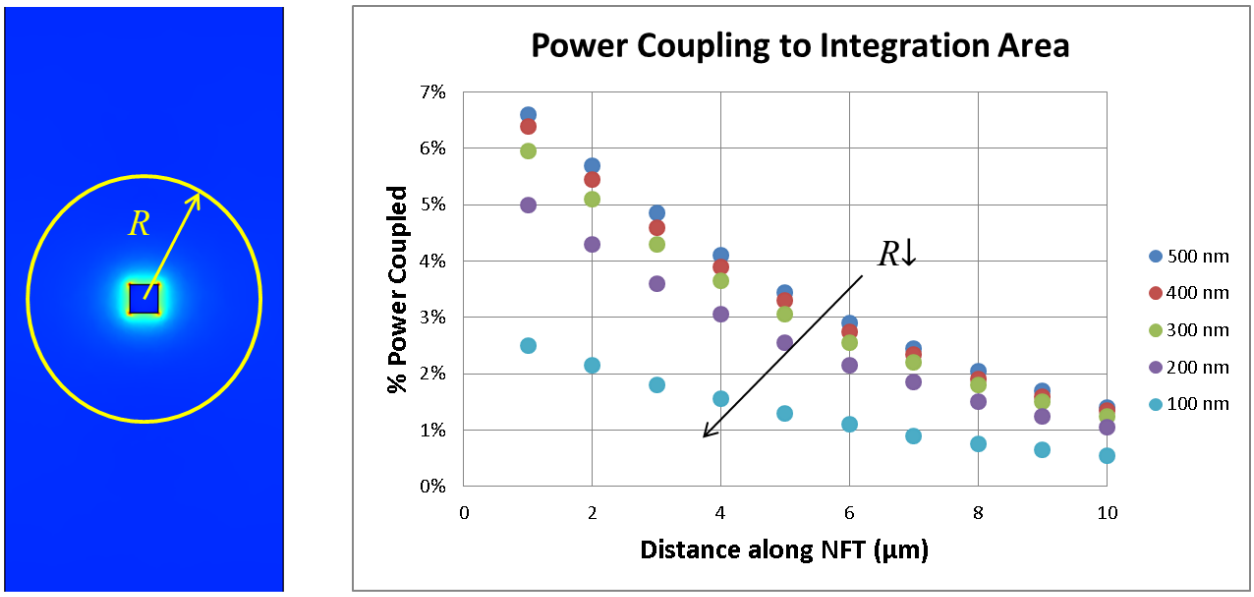

(a) (b)

Figure 92: (a) Circular integration area with radius *R* around the NFT (b) Power coupling to the integration area for radius 100 to 500 nm as a function of distance along NFT. The amount of power passing through the integration area only changes when the radius decreases to about 200 nm, which is the 1/e decay length of the NFT mode. This signifies the power is localized around the NFT.

We further confirm power coupling to the NFT mode by examining a cross section slice of the NFT and the surrounding material as shown in Figure 92a. We had calculated that the NFT mode decay length is 200 nm on each side of the NFT. If we pick a circular integration area with radius *R* and the NFT as the center, then power coupled should not change much with $R > 200$ nm. In Figure 92b, we plot percentage power coupled as a function of distance along NFT for various integration radii from 100 to 500 nm. We note that power coupled only starts changing more noticeably after the radius has shrunk to 200 nm, signifying that power is localized around the NFT and matches the power distribution of our desired NFT mode.

5.5 Conclusion

Our novel light delivery system for HAMR consisting of a mode stabilized laser, resonator, and NFT is estimated to have a coupling efficiency of 50% based on transmission spectra from the waveguide output. We believe this efficiency can be improved by increasing the Q of the resonator. Other aspects of the resonator-NFT portion of the system such as the grating, taper, waveguide dimensions, critical coupling gap width have been designed through various simulations using COMSOL and Lumerical software. The grating requires more investigation because loss per grating drops coupled power to more than -20 dB and our simulation shows a coupling efficiency of 40% in the 1550 nm regime. Nevertheless, we are able to launch plasmonic modes on the NFT under this condition. We verify mode propagation through a series of thermal measurements that use a lock-in to measure AC voltage amplitude and phase lag. The amplitude measurements match our hand calculations as well as simulations performed in COMSOL. The phase lag results indicate a plasmonic mode with a propagation length of ~6 μm has been launched on the NFT and ~50% of the coupled power went into this mode instead of dissipating as heat. This is confirmed by an analysis of power breakdown using both experimental and simulation results.

Chapter 6: NFT Heat Dissipation and Thermal Interface Resistance

The HAMR NFT must dissipate some of the heat generated in its body into the surroundings or else it may significantly deform from overheating, causing HAMR to be entirely nonfunctional. We can encase the NFT, typically made of Au, in a high thermal conductivity (> 25 W/m-K, as in AlN) dielectric. In this scenario, the thermal dissipation into the dielectric will be limited by the thermal resistance associated with heat crossing the interface from the Au where it is carried by electrons, to the dielectric where it is carried by phonons. We examine the role of adhesion layers between Au and a prototypical high thermal conductivity dielectric, AlN, in improving thermal transport across this interface. Samples for this study consisted of an 80 nm thick Au film on top of a 100 nm thick AlN layer grown on a 500 μm thick sapphire substrate. A wedge shaped layer of Cr with thickness 0-5 nm was inserted between Au and AlN. Frequency domain thermoreflectance (FDTR) was used to characterize the interface thermal impedance between the Au and AlN. The presence of Cr decreased thermal resistance of the Au/AlN interface more than threefold. Without any Cr, the interface resistance is found to be 10 ± 1.6 m^2-K/GW while adding just 1 nm of Cr decreased that number to 5 ± 0.3 m^2-K/GW. Past 1 nm of Cr the interface showed no dramatic difference in thermal resistance, which suggests that the Au/AlN interface resistance can be vastly improved with sub-1 nm adhesion layers that do not adversely impact the plasmonic properties of the interface.

6.1 Thermal Interface Resistance

Thermal interface resistances can play a crucial role in dissipating the parasitic heat generated in HAMR NFTs into a surrounding dielectric. HAMR NFTs rely on plasmonic

localization of light at the interface between a metal (typically Au or Ag) and a dielectric, making heat transport across such an interface a common aspect of NFT design. We have examined the thermal resistance at the interface between Au and AlN. We choose AlN as the dielectric because it has a high thermal conductivity and as such gives rise to the situation where the interface thermal resistance will dominate heat transport. During transport of heat across this interface, electrons in the metal will first couple to phonons in the metal, which then couple to phonons in the dielectric in order to transport heat across the interface. For a metal-dielectric interface, the acoustic (AMM) and diffuse mismatch models (DMM) both capture the mismatch in impedance when phonons try to cross a boundary between materials with significantly different properties [125].

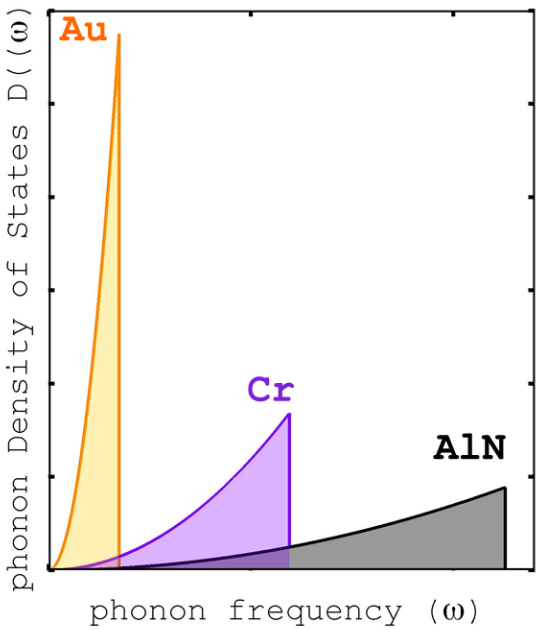

Figure 93: A visual representation of the Diffuse Mismatch Model (DMM), where phonon transmission probability is proportional to overlap of density of states D(ω).

In AMM, phonons are treated as plane waves and interact with boundaries at angles of reflection or refraction predicted by the acoustic analog of Snell's Law for electromagnetic waves. However, AMM is only accurate at low temperatures where phonons travel at wavelengths much greater than typical interatomic spacing. DMM predicts that all phonons scatter at an interface and is more reasonable at room temperatures. It assumes that the probability of a photon scattering into an interface is independent of where it came from and reflection or transmission is determined by the relative density of phonon states for the two materials. In particular, phonon transmission probability is proportional to the overlap of the density of states D(ω) [126]. Figure 93 shows a visual representation of DMM, where D(ω) is plotted as a function of phonon frequency ω according to eq. (6.1.1):

$$D(\omega) = \frac{\omega^2}{2\pi v_s^3} \quad (6.1.1)$$

where v_s is the speed of sound. Although these models have provided great insights into the mechanics of thermal transport, theory and experiment are often in poor agreement especially in high temperatures where a full spectrum of vibrational modes can be thermally excited [127].

Cahill *et al*. have done a series of experiments where the thermal resistance was measured at interfaces between highly dissimilar materials, epitaxial oxides, and metals ([125], [127], and [128]). For interfaces between two metals, electrons will contribute significantly to heat transport and we can ignore potential problems that may arise through electron-phonon coupling. It is reported that the thermal resistance of Al-Cu interfaces is below 1 m^2-K/GW in the temperature range of 70-300K, which is an order of magnitude smaller than typical metal-dielectric interfaces [128]. On the other end of the spectrum, Cahill reports the thermal resistance at the interface for two materials with highly dissimilar phonon properties, in this case Bi and

hydrogen-terminated diamond, to be more than 100 m^2-K/GW. The DMM quantifies this as the result of the materials having very different Debye temperatures θ_D [125].

In our present study, we aim to reduce thermal resistance between Au, a low Debye temperature metal (θ_D = 170 K), and AlN, a high Debye temperature dielectric (θ_D = 1150 K), through the addition of a thin interfacial layer of Cr (0-10 nm thick) between the two materials. The reason for choosing Cr is that it has a Debye temperature of 630K which is between the Debye temperatures of Au and AlN. Cahill's work provides experimental evidence on the importance of Debye temperature matching to facilitate thermal transport. We use as benchmark the lower limit of thermal resistance with a metal-metal interface of 1 m^2-K/GW and upper limit of a metal-dielectric interface with no interfacial material in between to be 10 m^2-K/GW [129]. Through measurement method known as frequency domain thermal reflectance (FDTR) and MATLAB data fitting, we obtain thermal resistances for various thicknesses of interfacial Cr and compare them against these benchmarks.

6.2 Sample Preparation and FDTR Measurement

For sample preparation, we deposited a film of AlN, approximately 100 nm thick, on 2" sapphire substrate whose tabulated Debye temperature of 1000K is close to that of AlN. The AlN was deposited using reactive sputtering from a metal Al target in a dedicated Tegal aluminum nitride sputtering system. AlN films were grown at a rate of 1.4 nm/s and the AlN thickness was measured by white light reflectometry on a Nanometrics Nanospec 210XP. We then deposited a wedge shaped layer of Cr using DC magnetron sputtering on top of AlN such that a continuous range of thicknesses, from 0-5 nm, can be sampled. The wedge films are prepared by moving the substrate into the target's deposition window at a controlled velocity before reversing the

direction so that the leading edge is exposed to the plasma longer than the trailing edge. The process is shown in Figure 94.

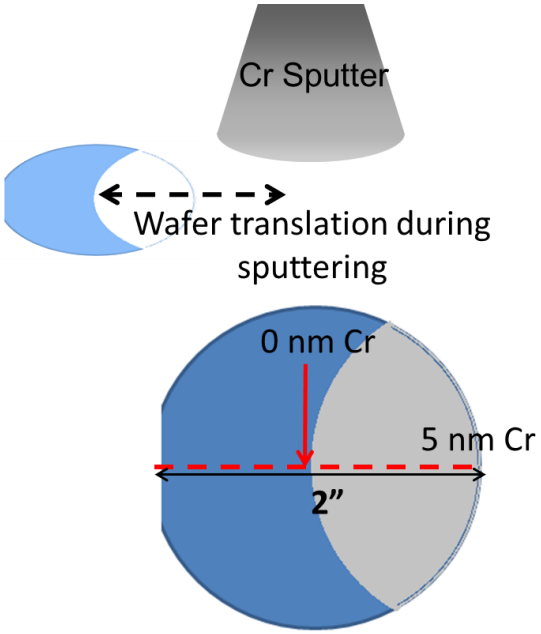

Figure 94: Wedge deposition process of Cr.

Finally we deposit 80 nm of Au on the Cr. The time between the Cr and Au depositions for each sample was kept to a minimum (~1 min) in order to minimize contamination of the Au/Cr interface. We note here that we used witness samples to confirm the thickness of Cr through X-ray reflectivity (XRR) and Au through profilometry.

We measure the interface thermal resistance by FDTR based on the setup shown in Figure 95a. A CW laser pump beam is modulated between 10 kHz-10 MHz by an electro-optic modulator (EOM) and heats the Au top layer. Changes in the temperature of the sample are monitored by changes in the intensity of the probe beam that is reflected from the Au surface due to a phase lag between pump and probe caused by thermal properties of the sample. The pump and probe signals, which may be isolated individually through a bandpass filter, are measured by

a photodiode and subsequently analyzed using an RF lock-in amplifier. We record the frequency-dependent phase lag of temperature change relative to the heat flux generated by the lock-in. The $1/e^2$ radius of the focused pump and probe beams is 2.7 ± 0.2 μm measured by knife-edge with the pump set to 300 mW and probe to 100 mW at room temperature.

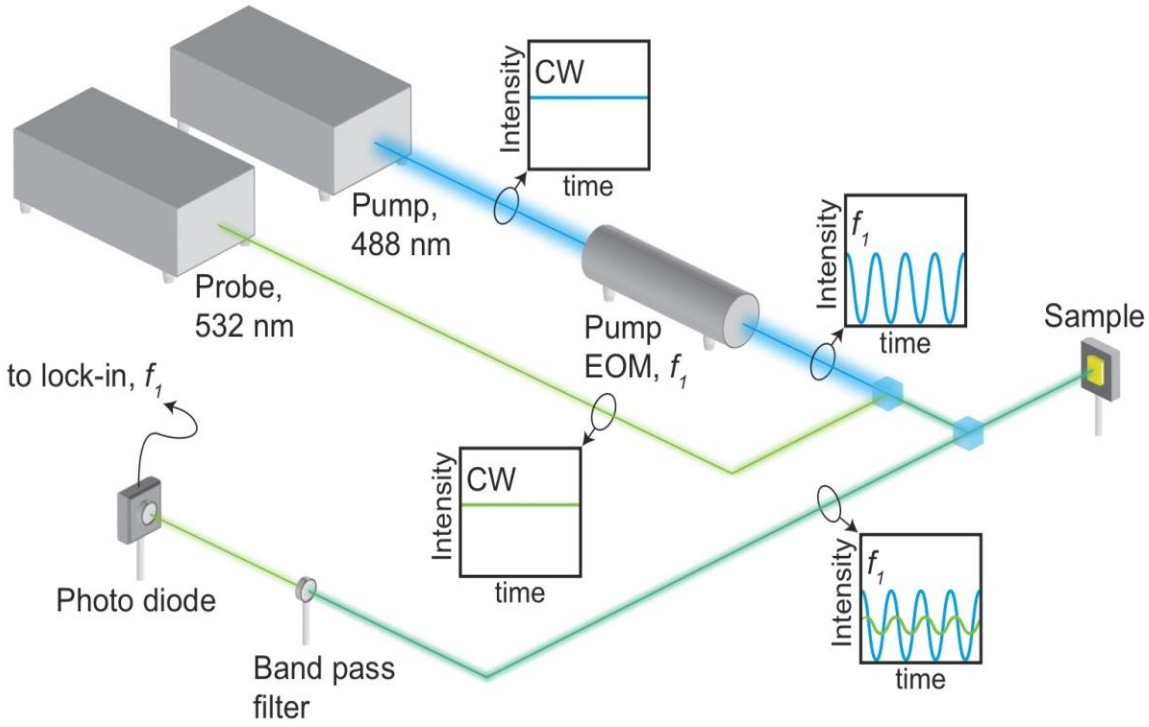

(a)

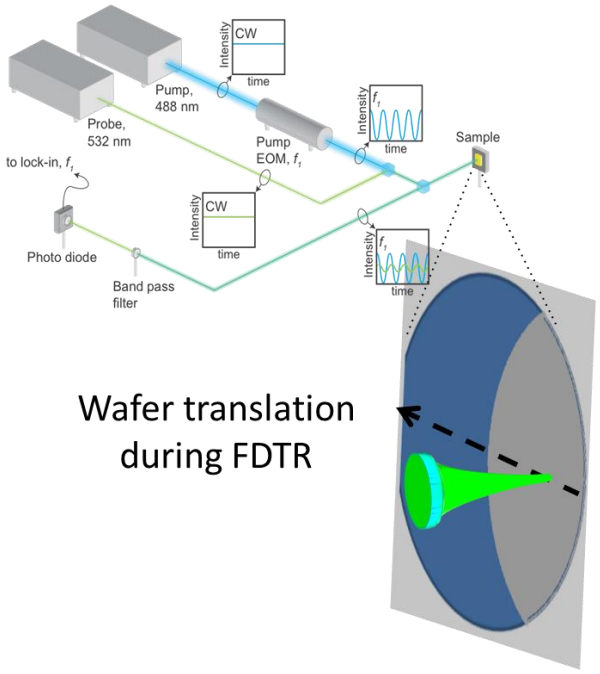

(b)

Figure 95: (a) Our experimental arrangement for FDTR based on cw lasers, a 532 nm probe and 488 nm pump laser. The pump is passed through an EOM, providing a modulated heat source. Both laser signals penetrate the sample and due to the sample heat properties, there will be a phase lag in the probe response **[130]**. A bandpass filter allows us to measure either the pump or probe signal response. (b) Movement of wafer translation during FDTR so that the entire thickness range of 0-5 nm Cr wedge can be measured.

When performing FDTR, we attach our sample to a motorized stage such that the entire range of 0-5 nm Cr wedge can be measured. The wafer translation movement is shown in Figure 95b.

6.3 Data Modeling and Results

Data collected from the FDTR experiment must be compared against a model of heat transport where unknown thermal properties are treated as free parameters and adjusted to minimize the difference between data and model. For our sample, we have the following 4 layers in order from top to bottom: Au, Cr, AlN, and sapphire. Each layer is described by a thermal conductivity k, density p, specific heat capacity C_p, and thickness L. We model interfaces as very

thin layers (1 Å) with no heat capacity. To calculate the changes in reflectivity, we employ the iterative solution described in [131] and compare it with the measured phase difference between pump and probe laser, measured as a function of modulation frequency. We optimize the fit between the prediction and the data by varying unknown parameters Au/AlN and AlN/sapphire interface resistances as well as laser spot size.

We model the Au/AlN interface, AlN, and AlN/sapphire interface as having thermal resistance, shown in Figure 96. In the presence of a thin Cr adhesion layer, we still treat the Au/Cr/AlN as a single interface. This parameter is allowed to vary as well as the AlN/sapphire interface resistance. We assume a value of 50 W/m-K for the thermal conductivity of AlN from a prior study [132] [133]. The thermal conductivity of the Au was calculated using the Wiedemann-Franz Law to be 136 W/m-K from four-point probe resistivity measurements. The AlN/sapphire interface resistance is constrained to have the same value in all samples and simultaneously fit to determine the Au/AlN interface resistance for each sample. In addition, we fit the laser spot size which is allowed to vary ± 0.2 from 2.7 μm.

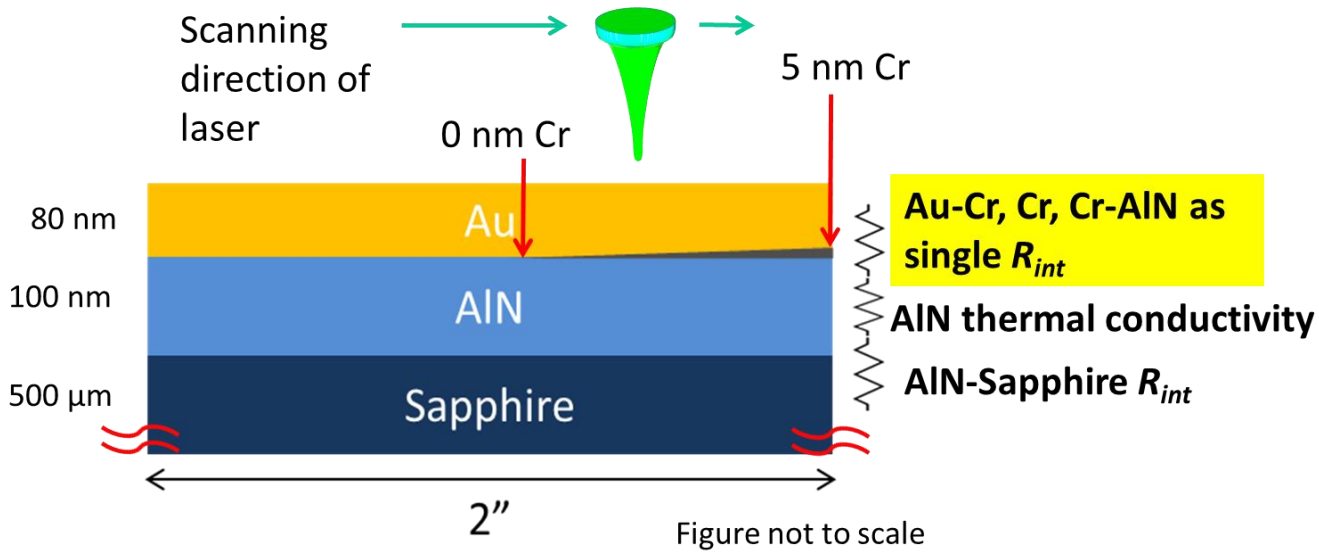

Figure 96: Our fitting model consists of 3 separate thermal interface resistances: Au/Cr/AlN, AlN, and AlN/Sapphire.

We plot the phase lag vs. the frequency of modulation from 100 kHz – 10 MHz for each FDTR measurement in Figure 97 and fit this data using a least squares curve fitting routine in MATLAB, afterwards using the computed Jacobian to obtain a confidence interval for our results.

To test the robustness of our simultaneous fitting program, we first fit the model to the data measured for each sample individually, with the AlN/sapphire interface resistance to vary from sample to sample. We used these values as initial guesses for the simultaneous fitting program and fit the model to all of the data simultaneously with the fitting constrained to use the same value for AlN/sapphire interface resistance. We observe the values resulting from these two methods differ by less than 5%. A thickness of 1 nm of Cr is enough to halve the interface resistance from 10 ± 1.6 m^2-K/GW to 5 ± 0.3 m^2-K/GW. Compare this to the reported value of 10 m^2-K/GW for a metal-dielectric interface [129], it is a significant improvement for such a thin layer. The interface resistance continues to decrease slightly past Cr thickness of 1 nm, though the rate of decrease is minimal. The AlN/sapphire interface resistance is fitted to be 5.0 m^2-K/GW.

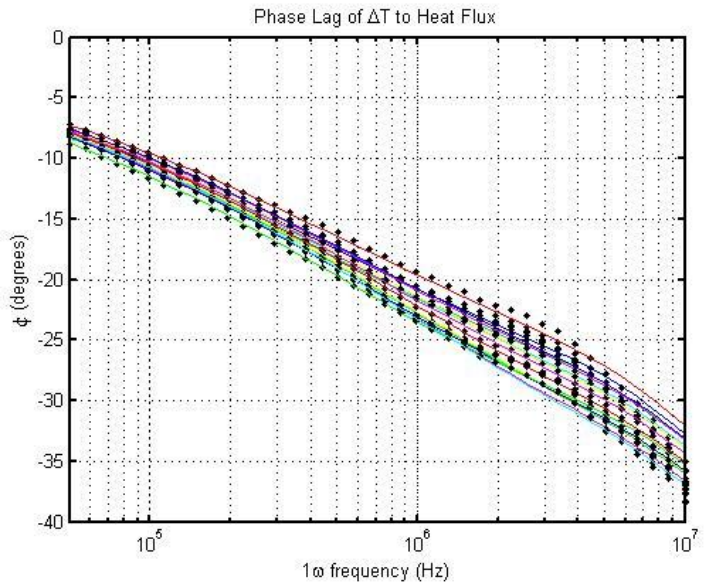

Figure 97: The calculated phase response for FDTR measurements over the range 100 kHz – 10 MHz of the sample at points with various Cr thicknesses.

The thermal interface resistance is plotted against Cr adhesion layer thickness in Figure 98, and we observe that the addition of a 1nm layer of Cr between Au and AlN drastically lowers the interface resistance. The Diffuse Mismatch Theory predicts that adding an adhesion layer with an intermediate Debye temperature in a metal-dielectric interface will result in lower interface resistance, but is it reasonable that this layer only needs to be ~1 nm thick? Our result suggests interfacial thermal transport between Cr and AlN is dominated by phonons with wavelengths less than 1 nm because in general a phonon mode is supported by a thin film when its wavelength is shorter than the film thickness. This is reasonable because long wavelength phonons have a much lower density of states than short wavelength phonons ($D(\lambda) \propto \lambda^{-2}$ based on the Debye linear dispersion model), therefore having a lower cumulative effect on the thermal interface resistance [134].

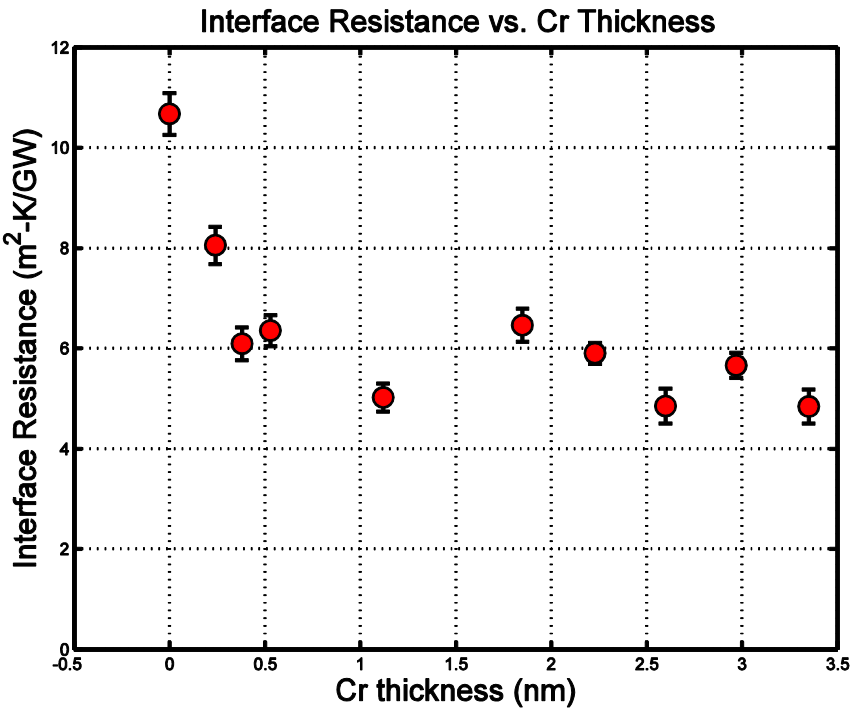

Figure 98: Plot of Au/AlN interface resistance vs. Cr thickness. A sharp decrease in resistance is observed with the addition of a 1nm layer of Cr.

6.4 Conclusion

The addition of a sub 1-nm Cr adhesion layer between Au and AlN decreased the thermal interface resistance more by about half from 10 ± 1.6 m^2-K/GW to 5 ± 0.3 m^2-K/GW. Past 1 nm Cr, there was minimal change in Au/AlN interface resistance. The region of interest is thus between Cr thickness 0-1 nm and we would like to make more samples to reproduce the results presented in Section 6.3. The main difficulty will lie in controlling and verifying the exact thickness of Cr deposited in the sub-1 nm range. From a practical perspective this result suggests that metal adhesion layers may be used to improve thermal transport without completely changing other interfacial properties such as the plasmonic properties needed in NFT technologies.

Chapter 7: Future Directions

So far in this work we have presented a complete HAMR light delivery system where 80% of the laser light can get coupled into the NFT. Now we discuss in this last section areas requiring further exploration. One is the integration of our system with the HAMR slider. Since our system is designed with an on-chip laser in mind, it will be built on GaAs substrate with the typical GaAs/AlGaAs laser layers. We discuss a method called transfer printing that enables us to transfer whatever we have fabricated on one type of substrate to an entirely different type. Another area that requires exploration is NFT designs. We used a simple rectangular shaped NFT out of convenience but perhaps other geometries may yield better coupling results, in particular with the recording medium. Other parameters such as operating wavelength and material refraction indices may have to be taken into consideration as well. In addition, the spot size generated by the NFT is also of great concern.

7.1 System Integration via Transfer Printing

Rogers *et al*. used transfer printing methods to achieve hybrid integration of III-V devices on Si platform. In their procedure they epitaxially release thin-film microscale GaAs based lasers after they have been fully fabricated on GaAs native substrates. An indium silver based alloy is then used to bond the laser to a Si substrate for enhanced performance [135]. This method has been known to achieve an alignment accuracy of ± 1 μm [136].

We would like to use transfer printing to release our light delivery system (LDS) onto the HAMR slider back and thus the head wafer. The only modification we would have to make for our existing process is to include a layer of AlAs between the LDS and the GaAs substrate which would be done during the laser layer growth process. As the first step, this sacrificial layer can be

etched with an undercut in a solution of HCl such that most of the LDS is floating and only a small area is connected to the native GaAs substrate by the AlAs. Then we can use a polydimethylsiloxane (PDMS) stamp to pick up the LDS and perform full release from the GaAs substrate. Afterwards, we print the LDS structure onto a HAMR head wafer coated with an indium silver based alloy at 150^0C in order to allow reflow in the paste without affecting any constituent materials in the laser structure. Finally, we remove the stamp after cooling to room temperature. This process is shown in Figure 99.

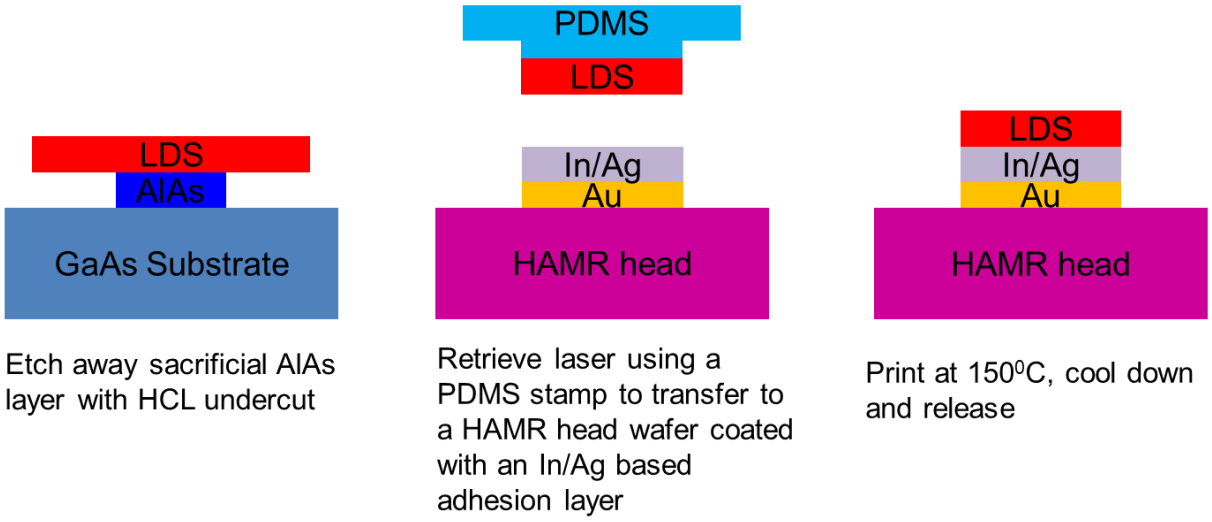

Figure 99: The transfer printing method can be applied to our laser such that we can integrate our light delivery system (LDS) with the HAMR head wafer.

7.2 Incorporation of Other NFT Designs

In our HAMR light delivery system, we concentrated our efforts on maximizing coupling efficiency between the laser and the NFT through a high Q resonator. Due to convenience, we employed a rectangular geometry for the NFT and minimal time was devoted to exploring other designs. However, it is beneficial to optimize various design parameters for the NFT not only to

maximize coupling but also to minimize the generated spot size. After all to make the NFT suitable for HAMR, it has to be able to focus optical fields down to 10-20 nm [137].

Within the 10-20 nm spot, we have to deliver a minimum power of ~210 μW [11]. Typically in power transfer problems, impedance matching plays an important role. In this case, we have to match the impedances of the waveguide and recording media with the NFT resonance. In addition, we need to be aware of the fact that optical power between waveguide and media is transferred through 2 modes, a symmetric and asymmetric plasmon mode. The NFT needs to emphasize higher coupling into the "suitable" mode. Vivek *et al*. performed a study using a taper based NFT design and found maximum coupling when keeping the wavelength range narrow and waveguide material index high [39].

Datta *et al*. also incorporates tapers into their designs to improve both optical and thermal performances of the NFT [38]. It has been previously demonstrated with bowtie apertures that having a tapered side wall instead of straight results in higher field concentration at the sub-20 nm spot size [138]. In Ref. [38], a traditional E antenna NFT is modified by including a taper in its notch. The optical coupling efficiency of the modified NFT improves by over 1.5 times compared to that of the traditional design. An even larger benefit is found in thermal figures of merit as a tapered notch with a wide base acting as a form of heat sink.

Not all tapered structures are beneficial for HAMR, but specifically designed tapers can deliver highly focused optical beams [139]. Thus, a tapered NFT holds great promise as it will utilize the lightning rod effect in which there is a rise in optical field concentration at the sharp metal termination. The structure will support surface plasmon polaritons (SPPs) which will experience considerable field concentration as they propagate toward the tip [140].

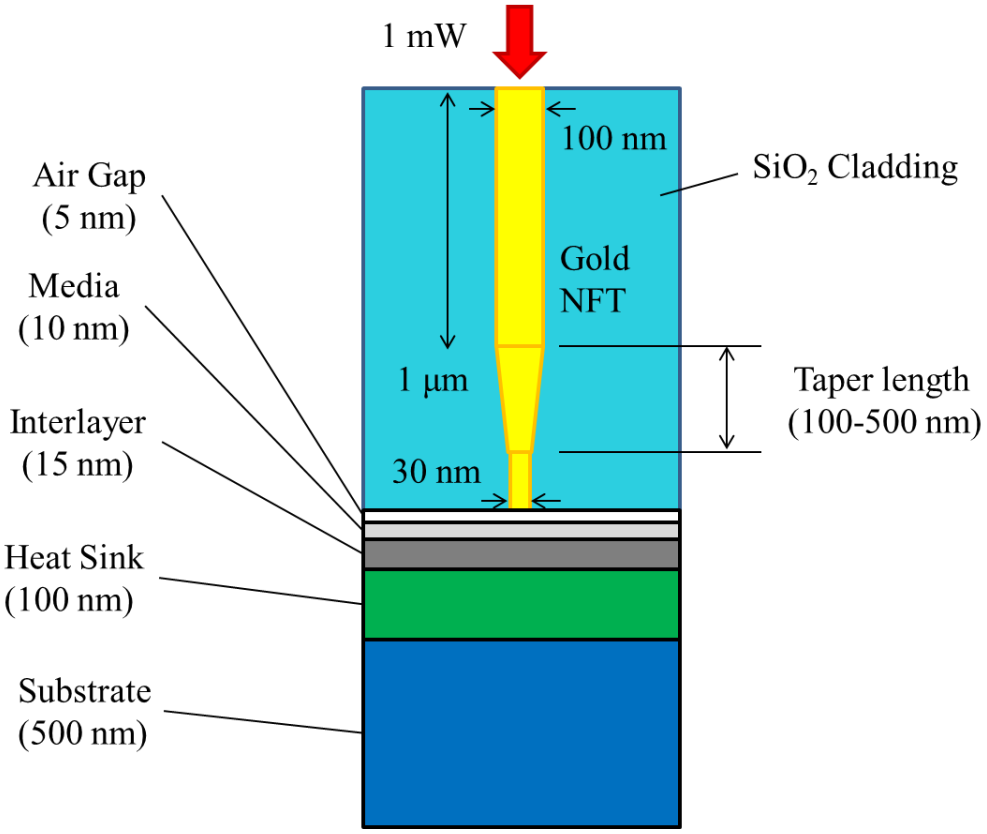

Figure 100: Simulation model for tapered NFT sending power into the media.

Taper Length (nm)	% Power Absorbed	% Power to Media	% Power Scattered
100	57%	32%	12%
200	70%	21%	9%
300	62%	30%	8%
400	77%	16%	7%
500	82%	15%	3%

Table 5: Simulated power absorbed by NFT, delivered to media, and scattered for NFT taper length 100 to 500 nm. The wavelength is set at 1500 nm.

We briefly analyze the coupling behavior of our NFT to the media by using a simple taper structure as shown in Figure 100. A gold NFT is surrounded by SiO_2 cladding. A 5 nm air gap sits above a 10 nm thick media, while a 15 nm interlayer and an 100 nm heat sink are placed below. The substrate is 500 nm thick in our model. Our current NFT is 100 nm in width, and we

need to taper down to about < 30 nm in reality. We vary the taper length from 100 to 500 nm and keep the launch section length constant at 1 μm. An incident power of 1 mW is sent into the NFT at a wavelength of 1500 nm. Percentages for power absorbed by the NFT, power delivered to the media, and scattered power are shown in Table 5. The data suggests that a short taper length will minimize NFT power absorption and maximize coupling to media, with an 100 nm taper NFT absorbing 57% of power and 32% delivered to the media. The media coupling percentage is comparable to the ~25% reported in [141]. A good taper structure may be challenging to fabricate, but our simulation suggests it can be integrated with our NFT to deliver the required power to the media.

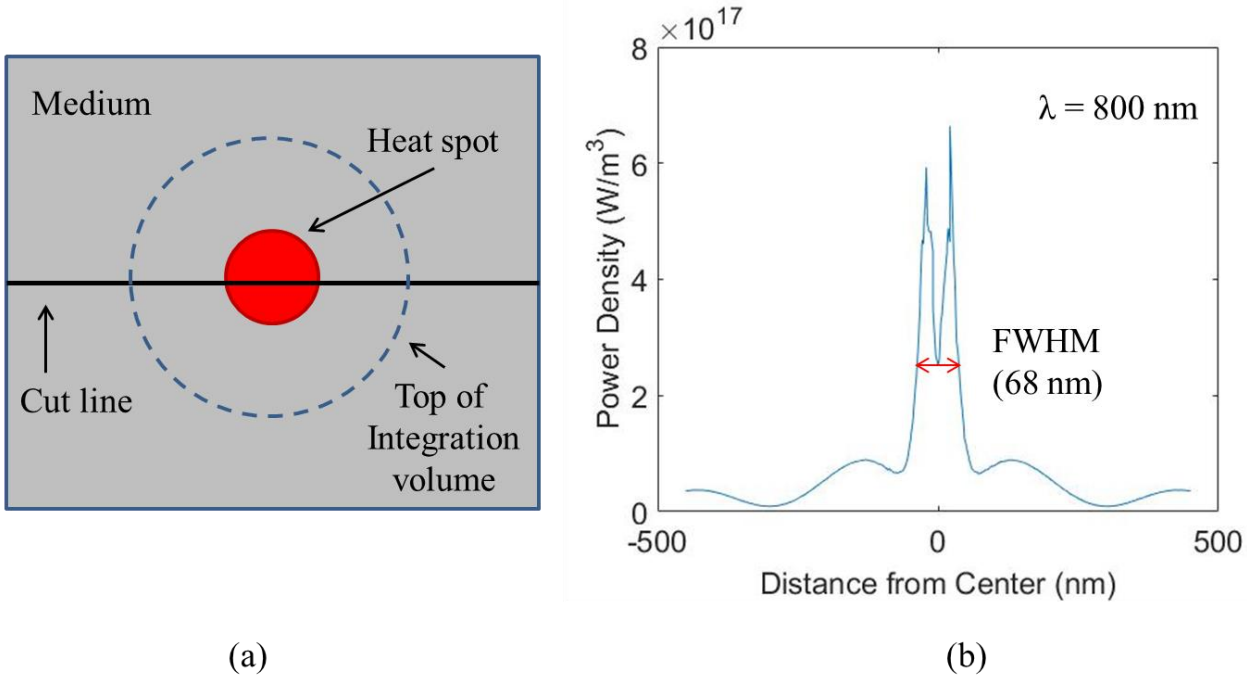

Figure 101: (a) Top view of medium with heat spot. A cut line is placed in our simulation to calculate the dissipated power density. We use an integration volume to later determine the degree of localization for comparison of launch waves of different wavelengths. (b) Plot of power density vs. distance from center of heat spot along cut line for 800 nm wavelength. We define our FWHM (68 nm) and use twice this value as the diameter of a cylindrical integration volume. We use the percentage of power dissipated within this volume relative to the whole media as a measure of heat localization for a launch wavelength.

One final area of exploration is the choice of lasing wavelength to use with this taper structure. First mentioned in Section 5.1, the industry standard is ~800 nm, our QD lasers operate at ~1000 nm, and we have been testing our resonator-waveguide-NFT system at ~1500 nm. The optimum wavelength is one that provides the highest localization for the generated heat spot in the medium. In Figure 101a, we show the top view of the medium as used in our model in Figure 100. We use a cut line through the heat spot and plot the dissipated power density along this line vs. the center of the heat spot. We show such a plot for a launch (laser) wavelength of 800 nm in Figure 101b using the same 30 nm taper end width in Figure 100. We define a FWHM and find a value of 68 nm. In a cylindrical volume with a diameter twice of the FWHM value, we calculate the dissipated power density as a percentage of the total for the whole medium. For 800 nm, we find a total of 13.5% dissipated in this volume. We repeat this process for lasing wavelengths of 1000 nm and 1500 nm. The percentages of total power dissipated are respectively 12.2% and 8.1%. These results suggest that heat is most localized at 800 nm but only marginally better than at 1000 nm. Due to the advantages associated with QD lasers, a 1% drop in power dissipation may be an acceptable penalty.

Wavelength (nm)	**% Localized (2 x FWHM)**	**% Non-localized**	**% Absorbed (NFT)**	**% Scattered (Cladding)**
800	14%	23%	38%	25%
1000	12%	23%	45%	20%
1500	8%	24%	57%	12%

Table 6: Power percentage breakdowns for launch wavelengths at 800 nm, 1000 nm, and 1500 nm. The percentage for power coupling into media is separated into localized (2 x FWHM) and non-localized regions. The rest of the power is either absorbed by the NFT or assumed to be scattered.

For our various wavelengths, the distribution of power into a localized cylindrical region with diameter twice the FWHM, the rest of the medium (non-localized), absorbed by NFT, and

scattered into the surrounding cladding is shown in Table 6. The data suggests that shorter wavelengths have less NFT power absorption (NFT heating) in addition to better localization. However, they lose more power to scattering. Thus depending on the needs of the system design, a compromise may be required.

7.3 Conclusion

The main focus of this work has been on the design, fabrication and demonstration of the feasibility of a novel HAMR light delivery system that can potentially couple 80% of the laser light into the NFT. This system consists of a mode stabilized laser, a dielectric waveguide, a high Q resonator, and the NFT. We divide the mode stabilized laser as one portion of the system to study and the waveguide-resonator-NFT as the second portion. Although they have been studied separately in this work, we show the feasibility of integrating the two into a complete system.

In Chapter 3, we discuss how we stabilize the mode of the laser by introducing external periodic loss in the form of an array of metallic nanostructures placed along the gain medium. We developed a fabrication technique using a combination of sputtered oxide and HF etching to control the height of the MSS such that they are placed on the same level as the gain medium. After MSS placement, the propagating E fields inside the laser cavity will align themselves such that they couple with the MSS at the minima. If the laser tries to shift to another mode, it will experience more loss as the MSS will no longer couple at the minima. Thus, the mode is stabilized.

Many methods for mode stabilization exist such as DFB and DBR lasers, but we distinguish ours with the fact that the laser can be mode stabilized post processing and avoids the complex patterning processes of DFB and DBR lasers. The MSS can be placed down next to the

laser after it has already been fabricated. This method can essentially transform any edge emitting laser into a mode stabilized one. It also provides flexibility to applications such as HAMR where the laser must undergo several integration steps. Mode stabilization can then be viewed as an add-on to improve laser performance that can be inserted into nearly any step in the integration process.

We discuss further improvements that can be made to our laser in terms of geometry and heat sinking in Chapter 4. We examined ring vs. bar lasers and found that for the footprint of the HAMR sliders (700 μm^2), bar lasers will cause a higher temperature rise than ring lasers (60-100K vs. at most 60K). We examine the requirements for our laser to operate in CW and conclude that a p-side mounted copper heat sink or decreasing ridge width to 1 μm is sufficient.

In Chapter 5, we study the waveguide-resonator-NFT portion of our light delivery system. While we test this part of the system using an external tunable laser, we show the feasibility of integration with our mode stabilized laser by fabricating a Si_3N_4 waveguide and placing it next to the laser gain medium using the same method for placing the MSS. We demonstrate the coupling effect of the NFT on the resonator Q via the waveguide output transmission spectra. We also determine plasmonic mode propagation along the NFT by pulsing our external laser and measuring the AC voltage amplitude and phase lag at specific locations. Successful launching of plasmonic modes not only allows HAMR to deliver small enough heat spots with the NFT but provides a platform for general photonic integration involving metallic nanostructures.

Future work can focus on NFT design and integrating our light delivery system with the HAMR slider. In Chapter 6, we demonstrate that the addition of a sub 1-nm Cr adhesion layer between metal and dielectric can lower interface thermal resistance by a factor of 2. Decreasing

the thermal resistance prevents the NFT from overheating and possibly melting as well as allows coupled power to be efficiently delivered to the end of the NFT. In Chapter 7, we discuss other NFT designs that minimize generated spot size and using transfer printing to integrate our system with the HAMR slider.

In summary, listed below are the major contributions of this work along with their respective publishing venues:

- Demonstrated laser mode stabilization method with a SMSR of ~20 dB that can be applied post processing of the laser, providing more flexibility in device integration and avoiding complex fabrication techniques of DFB and DBR lasers.
    - **H. Liang** and J. A. Bain, "Diode Laser Mode Selection via Periodic Arrays of Adjacent Nanoscale Metallic Structures." *The 17th IEEE International Conference on Nanotechnology*, Pittsburgh, PA (2017).
    - Submission in progress to *Optics Letters*
- Developed fabrication process that allows accurate placement of nanostructures within 50 nm of the laser gain medium, useful for any application that requires an on-chip laser to be integrated with other photonic devices.
    - **H. Liang** and J. A. Bain, "Diode Laser Mode Selection via Periodic Arrays of Adjacent Nanoscale Metallic Structures." *The 17th IEEE International Conference on Nanotechnology*, Pittsburgh, PA (2017).
- Determined that the ring geometry for lasers produces less device heating than the bar geometry for mounting on the HAMR slider backside, with temperature increase for the former no more than 60K and the latter as much as 110K.

- **H. Liang**, J. A. Bain, L. Chomas, T. E. Schlesinger, and K. Kuriyama, "Bending Loss Analysis of GaAs/AlGaAs Quantum Dot Ridge-Guided Ring Lasers for Coupling to HAMR NFT." *The 13th Joint MMM-Intermag Conference*, San Diego, CA (2016).
- **H. Liang**, J. A. Bain, L. Chomas, T. E. Schlesinger, and K. Kuriyama, "Internal vs. Bending Loss of GaAs/AlGaAs Quantum Dot Ridge Ring Lasers." *Annual Conference on Magnetism and Magnetic Materials (MMM)*, Honolulu, HI (2014).

- Demonstrated plasmonic modes with a propagation length of 6 μm can be launched on a gold NFT via the use of an 11 μm radius disk resonator with a Q of ~15,000.
  - Planned submission to archival journal
- Decreased NFT thermal interface resistance by factor of 2 via a sub-1 nm layer of Cr.
  - M. Jeong, J. P. Freedman, **H. Liang**, C. Chow, V. M. Sokalski, J. A. Bain, and J. A. Malen. "Enhancement of Thermal Conductance at Metal-Dielectric Interfaces Using Subnanometer Metal Adhesion Layers." *Physical Review Applied* 5.014009 (2016).
  - **H. Liang**, J. A. Bain, and J. A. Malen, "The Use of Metallic Adhesion Layers in Reducing Interface Thermal Resistance." *Annual Conference on Magnetism and Magnetic Materials (MMM)*, Honolulu, HI (2014).
- Demonstrated feasibility of a high efficiency HAMR light delivery system with laser power source requirements as low as 1 mW.
  - Planned submission to archival journal

References

[1] R. Cook, July 2014. [Online]. Available: http://www.thessdreview.com/featured/ssd-throughput-latency-iopsexplained/.

[2] J. S. Domingo, "SSD vs. HDD: What's the Difference?," 20 June 2016. [Online]. Available: http://www.pcmag.com/article2/0,2817,2404258,00.asp.

[3] D. Bates, "Think before You Save! World Could Run out of Computer Hard Drive Space by 2020, Expert Warns.," 22 Dec. 2014. [Online]. Available: http://www.dailymail.co.uk/sciencetech/article-2883722/Be-careful-save-World-run-computer-hard-drive-space-2020-expert-warns.html.

[4] F. G. Sanchez, "1.2 Magnetic Recording Crisis and Challenges.," Nov. 2007. [Online]. Available: http://www.fgarciasanchez.es/thesisfelipe/node5.html.

[5] V. Beal, "Perpendicular Hard Drive Recording Technology.," 21 Apr 2006. [Online]. Available: http://www.webopedia.com/DidYouKnow/Computer_Science/perpendicular_hard_drive_technology.asp.

[6] M. H. Kryder, E. C. Gage, T. W. Mcdaniel, W. A. Challener, R. E. Rottmayer, G. Ju, Y.-T. Hsia and M. F. Erden, "Heat Assisted Magnetic Recording," *Proceedings of the IEEE,* vol. 96, no. 11, 2008.

[7] D. Weller et al., "A HAMR Media Technology Roadmap to an Areal Density of 4 TB/in^2," *IEEE Transactions on Magnetics ,* vol. 50, no. 1, 2014.

[8] S. Xiong, "Head-disk Interface Study for Heat Assisted Magnetic Recording (HAMR) and Plasmonic Nanolithography for Patterned Media," Unviersity of California, Berkeley, 2014.

[9] D. Lim and Y. Kim, "Light Delivery for the Heat Assisted Magnetic Recording (HAMR) Head with Grating Structure," *Optical Data Storage,* 2007.

[10] M. Hirata et al., "Light Delivery System for Heat-Assisted Magnetic Recording," *IEEE Transactions on Magnetics,* vol. 45, no. 11, pp. 5016-021, 2009.

[11] V. Krishnamurthy et al., "Efficient Integrated Light-Delivery System Design for HAMR: Maximal Optical Coupling for Transducer and Nanowaveguide," *IEEE Transactions on Magnetics,* vol. 52, no. 2, pp. 1-7, 2016.

[12] N. P. Barnes, "Solid-State Lasers From an Efficiency Perspective," *IEEE JOURNAL OF SELECTED TOPICS IN QUANTUM ELECTRONICS,* vol. 13, no. 3, 2007.

[13] "Power Consumption of PC Components in Watts," Build Computers.net, 2016. [Online]. Available: http://www.buildcomputers.net/power-consumption-of-pc-components.html.

[14] "Photonic Integration," Infinera, 2015.

[15] A. Witvrouw, "CMOS-MEMS Integration: Why, How and What?," in *IEEE/ACM International Conference on Computer-Aided Design*, San Jose, CA, USA, 2006.

[16] S. Melle, "Photonic Integrated Circuits: a Technology Update," *IEEE Communications Magazine,* vol. 46, no. 2, 2008.

[17] T. A. Heumier and J. L. Carlsten, "Mode Hopping in Semiconductor Lasers".

[18] J. Spencer and Y. Preston, "Contrasting the Photodigm DBR Laser Diode Architecture with Competing DFB Designs.," Photodigm, Inc., [Online]. Available: http://www.photodigm.com/difference-between-dbr-and-dfb-lasers.

[19] R. Paschotta, "Distributed Feedback Lasers".

[20] R. Paschotta, "Distributed Bragg Reflector Lasers".

[21] "Laser Diodes," QD Photonics, [Online]. Available: http://www.qphotonics.com/.

[22] "How Much Do Laser Diodes Cost?," Laser Diode Source, [Online]. Available: https://www.laserdiodesource.com/how-much-does-a-laser-diode-cost.

[23] C. M. Bender and S. Boettcher, "Real Spectra in Non-Hermitian Hamiltonians having PT Symmetry," *Phys. Rev. Lett.,* vol. 80, pp. 5243-246, 1998.

[24] P. Bo et al., "Parity Time Symmetric Whispering-Gallery Microcavities," *Nature Physics,* vol. 10, no. 5, pp. 394-8, 2014.

[25] C. Witte, "Hamiltonian Operator," in *Compendium of Quantum Physics*, Berlin, Springer, 2009.

[26] L. van Dommelen, "Hermitian Operators," Florida State University, [Online]. Available: http://www.eng.fsu.edu/~dommelen/quantum/style_a/herm.html.

[27] C. M. Bender, "Making Sense of Non-Hermitian Hamiltonians," *Rept. Prog. Phys.,* vol. 70, p. 947, 2007.

[28] G. Barton, "Introduction to Advanced Field Theory," in *Ch. 12*, New York, John Wiley & Sons, 1963.

[29] H. Hodaei et al., "Parity-time-symmetric Coupled Microring Lasers Operating around an Exceptional Point," *Optics Letters,* vol. 40, no. 21, 2015.

[30] M. Chamanzar et al., "Hybrid photonic surface-plasmon-polariton ring resonators for sensing applications," *Applied Physics B Lasers and Optics,* vol. 101, pp. 263-271, 2010.

[31] M. Juan, "Plasmon Nano-Optical Tweezers," *Nature Photonics,* vol. 5, pp. 349-356, 2011.

[32] R. Tripp et al., "Novel Nanostructures for SERS Biosensing," *Nano Today,* vol. 3, pp. 31-37, 2008.

[33] H. Atwater and A. Polman, "Plasmonics for Improved Photovoltaic Devices," *Nature Materials,* vol. 9, pp. 205-213, 2010.

[34] X. Huang et al., "Cancer Cell Imaging and Photothermal Therapy in the Near Infrared Region Using Gold Nanorods," *J. Am. Chem. Soc.,* vol. 128, pp. 2115-2120, 2006.

[35] N. Zhou et al., "Plasmonic Near-field Transducer for Heat-assisted Magnetic Recording," *Nanophotonics,* vol. 3, no. 3, 2014.

[36] R. Ikkawi et al., "Near-Field Optical Transducer for Heat-Assisted Magnetic Recording for Beyond-10-Tbit/in2 Densities," *Journal of Nanoelectronics and Optoelectronics,* vol. 3, no. 1, pp. 44-54, 2008.

[37] W. A. Challener et al., "Heat-assisted Magnetic Recording by a Near-field Transducer with Efficient Optical Energy Transfer," *Nature Photonics,* vol. 3, no. 5, 2009.

[38] A. Datta and X. Xu, "Improved Near-Field Transducer Design for Heat-Assisted Magnetic Recording," *IEEE Transactions on Magnetics,* vol. 52, no. 12, 2016.

[39] V. Krishnamurthy et al., "Maximizing the Plasmonic Near-Field Transducer Efficiency to Its Limit for HAMR," *Journal of Lightwave Technology,* vol. 34, no. 4, pp. 1184-190, 2016.

[40] S. Bhargava and E. Yablonovitch, "HAMR Thermal Reliability via Inverse Electromagnetic Design," University of California, Berkeley.

[41] S. K. Dash et al., "Dielectric Resonator Antennas: An Application Oriented Survey," *Journal of RF and Microwave Computer-Aided Engineering ,* vol. 10, no. 1002, 2016.

[42] C. Wang and K. Zaki, "Dielectric Resonators and Filters," *IEEE Microwave Magazine,* vol. 8, no. 5, pp. 115-27, 2007.

[43] M. Soltani et al., "Ultra-high Q Planar Silicon Microdisk Resonators for Chip-scale Silicon Photonics," *Optics Express,* vol. 15, no. 8, 2007.

[44] L. Hady et al., "Dual Function of a Dielectric Resonator: A High-Q Resonator and a Low-Q Radiator," *IEEE MTT-S International Microwave Symposium Digest,* 2008.

[45] P. Bhattacharya, Semiconductor Optoelectronic Devices, Englewood Cliffs: Prentice Hall, 1994.

[46] S. C. Horst et al., "GaAs/AlGaAs Ridge Lasers with Etched Mirrors Formed by an Inductively Coupled Plasma Reactor," *Applied Physics Letters,* vol. 71, no. 11, 1997.

[47] P. Derry et al., in *Semiconductor Lasers*, Boeing Defense & Space Group.

[48] B. Streetman and S. Banerjee, Solid State Electronic Devices, Upper Saddle River: Prentice Hall, 2000.

[49] R. G. Hunsperger, Integrated Optics, Theory and Technology, Berlin: Springer-Verlag, 1984.

[50] M. Kuno, "Density of States," in *Introdutory Nanoscience*, London, Garland Science, 2012.

[51] G. J. Devlin and R. O'Connor, *Quantum Electronics Project: Quantum Wells, Wires, & Dots and Quantum Well Lasers.*

[52] D. Bimberg et al., "Quantum Dot Lasers: Theory and Experiment," in *AIP Conference Proceedings*, 2001.

[53] "DOS multdim.jpg," Wikimedia Commons, [Online]. Available: https://commons.wikimedia.org/w/index.php?title=File:DOS_multdim.jpg&oldid=201614929.

[54] J. Coleman et al., "Semiconductor Quantum Dot Lasers: A Tutorial," *Journal of Lightwave Technology,* vol. 29, no. 4, pp. 499-510, 2011.

[55] R. Syms and J. R. Cozens, "The Slab Waveguide," in *Optical Guided Waves and Devices*, London, McGraw-Hill, 1992.

[56] M. Khan, "Analysis of Metal-Clad TM-Pass Polarizers Using the Method of Lines," 2001.

[57] "Optical Cavity and Laser Modes," University of Babylon.

[58] S. Liao et al., *Ch.13 Maxwell's Equations and Magnetic Waves,* 2004.

[59] M. Gomilsek, "Whispering Gallery Modes," Ljubljana, Slovenia, 2011.

[60] M. Foreman, "Whispering Gallery Mode Sensors," *Adv. Opt. Photon.,* pp. 168-240, 2015.

[61] K. Grutter, "Optical Whispering-Gallery Mode Resonators for Applications in Optical Communication and Frequency Control," 2013.

[62] R. D. Kekatpure, "First-Principles Full-Vectorial Eigenfrequency Computations for Axially Symmetric Resonators," *Journal of Lightwave Technology,* vol. 29, no. 3, pp. 253-59, 2011.

[63] U. o. Oklahoma, "2.4 Circular Waveguide," [Online]. Available: https://www.nhn.ou.edu/~johnson/Education/Juniorlab/Microwave/CylindricalWaveguide.pdf.

[64] Rochester Institute of Technology, [Online]. Available: https://www.cis.rit.edu/class/simg303/Notes/Ch7-PropagationofWaves.pdf.

[65] D. S. Weile, "Cylindrical Waves," 2006.

[66] J. A. Stratton, Electromagnetic Theory, McGraw-Hill, 1941.

[67] A. Yariv, "Critical Coupling and Its Control in Optical Waveguide-ring Resonator Systems," *IEEE Photonics Technology Letters,* vol. 14, no. 4, pp. 483-5, 2002.

[68] T. Kamalakis and T. Sphicopoulos, "Frequency Dependence of the Coupling Coefficients and Resonant Frequency Detuning in a Nanophotonic Waveguide-Cavity System," *IEEE Journal of Quantum Electronics,* vol. 42, no. 8, pp. 827-37, 2006.

[69] K. Garcia, "Calculating Component Coupling Coefficients," 2000.

[70] M. Chabalko, "Heat Assisted Magnetic Recording Near Field Transducer Analysis and Design," 2012.

[71] M. Altissimo, "E-beam Lithography for Micro-/nanofabrication," 2010.

[72] D. K. Cheng, Field and Wave Electromagnetics, Pearson Education Limited, 2014.

[73] G. Stareev, "Formation of Extremely Low Resistance Ti/Pt/Au Ohmic Contacts to p-GaAs," *Applied Physics Letters,* vol. 62, no. 22, pp. 2801-2803, 1993.

[74] A. G. Baca, "A Survey of Ohmic Contacts to III-V Compound Semiconductors," *Thin Solid Films,* pp. 599-606, 1997.

[75] L. V. Asryan and S. Luryi, "Effect of Internal Optical Loss on Threshold Characteristics of Semiconductor Lasers with a Quantum-Confined Active Region," *IEEE Journal of Quantum Electronics,* vol. 40, no. 7, 2004.

[76] T. Ito et al., "Internal Loss and Gain Factor of InGaAsP/GaAs Laser," *Japanese Journal of Applied Physics,* vol. 26, no. 3, pp. 501-2, 1987.

[77] A. Haug, "Free-Carrier Absorption in Semiconductor Lasers," *Semiconductor Science Technology,* pp. 373-8, 1992.

[78] P. Togher, "The Temperature Dependence of Gain in Semiconductor Lasers," 1996.

[79] J. Huang and L. W. Casperson, "Gain and Saturation in Semiconductor Lasers," *Optical and Quantum*

Electronics, pp. 369-390, 1993.

[80] "What is the normal operating temperature for Seagate disk drives?," Seagate Technology, [Online]. Available: http://knowledge.seagate.com/articles/en_US/FAQ/193771en.

[81] "Spectral Properties of Miniature CW Lasers," Integrated Optics, 2017. [Online]. Available: https://integratedoptics.com/spectral-properties-of-cw-lasers.

[82] B. Liu et al., "Femto Slider: Fabrication and Evaluation," *IEEE Transactions on Magnetics,* vol. 39, no. 2, pp. 909-914, 2003.

[83] M. Bass et al., "Semiconductor Lasers," in *Handbook of Optics*, New York, McGraw-Hill, 2010.

[84] E. Marcatili and S. E. Miller, "Improved Relations Describing Directional Control in Electromagnetic Wave Guidance," *Bell System Technical Journal,* pp. 2161-188, 1969.

[85] T. R. Chen et al., "Experimental Determination of Transparency Current Density and Estimation of the Threshold Current of Semiconductor Quantum Well Lasers," *Applied Physics Letters,* vol. 56, no. 11, 1990.

[86] K. Kamath et al., "Small-signal Modulation and Differential Gain of Single-mode Self-organized In[sub 0.4]Ga[sub 0.6]As/GaAs Quantum Dot Lasers," *Applied Physics Letters,* vol. 70, no. 22, 1997.

[87] H. Li et al., "Carrier Lifetime and Radiative Recombination in Quantum Dot LEDs," in *IEEE Lasers and Electro-Optics Society 2000 Annual Meeting*, 2000.

[88] P. Bhattacharya, "High-Performance Quantum Dot Lasers," *Comprehensive Semiconductor Science and Technology,* 2011.

[89] V. M. Ustinov et al., Quantum Dot Lasers, Oxford, 2003.

[90] M. Austin and P. Flavin, "Small-radii Curved Rib Waveguides in GaAs/GaAlAs Using Electron-beam Lithography," *Journal of Lightwave Technology,* vol. 1, no. 1, pp. 236-40, 1983.

[91] N. Tansu et al., "Temperature Analysis and Characteristics of Highly Strained InGaAs-GaAsP-GaAs (λ> 1.17μm) Quantum-well Lasers," *IEEE Journal of Quantum Electronics,* vol. 38, no. 6, pp. 640-51, 2002.

[92] M. Asada et al., "The Temperature Dependence of the Threshold Current of GaInAsP/InP DH Lasers," *IEEE Journal of Quantum Electronics,* vol. 17, no. 5, pp. 611-19, 1981.

[93] Y. Zou et al., "Experimental Study of Auger Recombination, Gain, and Temperature Sensitivity of 1.5μm Compressively Strained Semiconductor Lasers," *IEEE Journal of Quantum Electronics,* vol. 29, no. 6, pp. 1565-575, 1993.

[94] L. Huang et al., "HAMR Thermal Modeling Including Media Hot Spot," *IEEE TRANSACTIONS ON MAGNETICS,* vol. 49, no. 6, 2013.

[95] C. P. Seassal et al., "InP Microdisk Lasers on Silicon Wafer: CW Room Temperature Operation at 1.6 μm," *Electronics Letters,* vol. 37, no. 4, 2001.

[96] J. P. Hohimer et al., "CW Room-temperature Operation of Y-junction Semiconductor Ring Lasers," *Electronics Letters,* vol. 28, no. 4, 1992.

[97] S. Yamamoto et al., "680 nm CW Operation at Room Temperature by AlGaAs Double Heterojunction Lasers," *IEEE Journal of Quantum Electronics,* vol. 19, no. 6, 1983.

[98] "Joule's Law of Heating," Electrical Engineering and Technology, 2016. [Online]. Available: http://www.electrical4u.com/joules-law/.

[99] J. D. Thomson et al., "Temperature Dependence of the Lasing Wavelength of InGaAs Quantum Dot Lasers," *Journal of Applied Physics,* vol. 90, no. 9, pp. 4859-861, 2001.

[100] A. Castle, "How-To: Properly Apply Thermal Paste and Install a CPU," PC Gamer, 2010. [Online]. Available: https://www.pcgamer.com/how-to-properly-apply-thermal-paste-and-install-a-cpu/.

[101] "A piece of paper folded 103 times is as thick as the Universe," Science Alert, [Online]. Available: https://www.sciencealert.com/a-piece-of-paper-folded-103-times-will-be-as-thick-as-the-universe.

[102] "11 Best Thermal Pastes 2018," Gaming Factors, [Online]. Available: https://www.gamingfactors.com/best-thermal-paste/.

[103] "Substrate, Wafer and Die Thinning," Valley Design Corp., [Online]. Available: http://www.ceramicsubstrates.com/substrate-thinning.htm.

[104] X. Huang et al., "Ridge-width Dependence of the Threshold of Long Wavelength (λ ≈14 μm) Quantum Cascade Lasers with Sloped and Vertical Sidewalls," *Optics Express,* vol. 20, no. 3, 2012.

[105] M. Leers et al., "Next Generation Heat Sinks for High-power Diode Laser Bars," in *Twenty-Third Annual IEEE Semiconductor Thermal Measurement and Management Symposium* , 2007.

[106] Y. Luo et al., "A Silicon-aluminum Micro Heat Sink for Light Emitting Diode (LED) Chips," in *16th International Conference on Electronic Packaging Technology (ICEPT)* , 2015.

[107] M. Tien et al., "Ultra-high Quality Factor Planar Si3N4 Ring Resonators on Si Substrates," *Optics Express,* vol. 19, no. 14, 2011.

[108] K. R. Harper, "Theory, Design, and Fabrication of Diffractive Grating Coupler for Slab Waveguide," 2003.

[109] T. Tamir and S. T. Peng, "Analysis and Design of Grating Couplers," *Applied Physics,* vol. 14, no. 3, pp. 235-54, 1977.

[110] Y. Fu et al., "Efficient Adiabatic Silicon-on-insulator Waveguide Taper," *Photonics Research,* vol. 2, no. 3, 2014.

[111] D. Gallagher and T. P. Felici, "Eigenmode Expansion Methods for Simulation of Optical Propagation in Photonics: Pros and Cons," *Optics: Devices, Materials, and Technologies VII ,* 2003.

[112] P. Karioja and D. Howe, "Diode-Laser-to-Waveguide Butt Coupling," *Applied Optics,* vol. 35, no. 3, 1996.

[113] R. Marchetti et al., "High-efficiency Grating-couplers: Demonstration of a New Design Strategy," *Scientific Reports,* vol. 7, no. 1, 2017.

[114] M. Zhang et. al, "Monolithic Ultra-High-Q Lithium Niobate Microring Resonator," *Optica,* vol. 4, no. 12, 2017.

[115] R. Paschotta, "Finesse".

[116] K. Leong and J. Mazierska, "Precise Measurements of the Q Factor of Dielectric Resonators in the Transmission Mode-accounting for Noise, Crosstalk, Delay of Uncalibrated Lines, Coupling Loss, and Coupling Reactance," *IEEE Transactions on Microwave Theory and Techniques ,* vol. 50, no. 9, pp. 2115-127, 2002.

[117] D. Spencer et al., "Integrated Si3N4/SiO2 Ultra High Q Ring Resonators," in *IEEE Photonics Conference*, 2012.

[118] X. Cheng et al., "Fabrication of a High-Q Factor Ring Resonator Using LSCVD Deposited Si3N4 Film," *Optical Materials Express,* vol. 7, no. 7, 2017.

[119] T. Wang et al., "High-Quality LiNbO3 Microdisk Resonators by Undercut Etching and Surface Tension Reshaping," *Optics Express,* vol. 20, no. 27, 2012.

[120] "Principles of Lock-in Detection and the State of the Art," Zurich Instruments, 2016.

[121] Connected Textiles, [Online]. Available: www.tibtech.com/conductivity.php.

[122] T. Yamane et al., "Measurement of Thermal Conductivity of Silicon Dioxide Thin Films Using a 3ω Method," *Journal of Applied Physics,* vol. 91, no. 12, 2002.

[123] D. Yakubovsky et al., "Optical Constants and Structural Properties of Thin Gold Films," *Optics Express,* vol. 25, no. 21, 2017.

[124] H. Lin et al., "Thermal and Electrical Conduction in 6.4 nm Thin Gold Films," *Nanoscale,* vol. 5, no. 11, pp. 4652-4656, 2013.

[125] D. Cahill et al., "Nanoscale Thermal Transport," *Journal of Applied Physics,* vol. 93, no. 793, 2003.

[126] E. T. Swartz and R. O. Pohl, "Thermal Boundary Resistance," *Reviews of Modern Physics,* vol. 61, no. 3, pp. 605-68, 1989.

[127] R. M. Costescu et al., "Thermal Conductance of Epitaxial Interfaces," *Physical Review B,* vol. 67, no. 5, 2003.

[128] B. C. Gundrum et al., "Thermal Conductance of Metal-metal Interfaces," *Physical Review B,* vol. 72, no. 24, 2005.

[129] H. Chien et al., "Measurement and Evaluation of the Interfacial Thermal Resistance between a Metal and a Dielectric," *Applied Physics Letters,* vol. 93, no. 23, 2008.

[130] A. Schmidt et al., "A Frequency-domain Thermoreflectance Method for the Characterization of Thermal Properties," *Review of Scientific Instruments,* vol. 80, no. 9, 2009.

[131] D. G. Cahill, "Analysis of Heat Flow in Layered Structures for Time-domain Thermoreflectance," *Review of Scientific Instruments,* vol. 75, no. 12, pp. 5119-122, 2004.

[132] Z. Su et al., "The Impact of Film Thickness and Substrate Surface Roughness on the Thermal Resistance of Aluminum Nitride Nucleation Layers," *Journal of Appliled Physics,* vol. 113, no. 21, 2013.

[133] Z. Su et al., "Layer-by-layer Thermal Conductivities of the Group III Nitride Films in Blue/green Light Emitting Diodes," *Applied Physics Letters,* vol. 100, no. 20, 2012.

[134] *NSF GOALI Collaboration proposal #1403447,* 2013.

[135] X. Sheng et al., "Transfer Printing of Fully Formed Thin-film Microscale GaAs Lasers on Silicon with a Thermally Conductive Interface Material," *Laser & Photonics Reviews,* vol. 9, no. 4, 2015.

[136] N. Ye et al., "High-Alignment-Accuracy Transfer Printing of Passive Silicon Waveguide Structures," *Optics Express,* vol. 26, no. 2, 2018.

[137] Y. Kong et al., "Evanescent Coupling Between Dielectric and Plasmonic Waveguides for HAMR Applications," *IEEE Transactions on Magnetics,* vol. 47, no. 10, pp. 2364-367, 2011.

[138] Y. Chen et al., "Fabrication of Bowtie Aperture Antennas for Producing Sub-20 nm Optical Spots," *Optics Express,* vol. 23, no. 7, pp. 9093-099, 2015.

[139] L. Miao and T. Y. Hsiang, "Tapered Waveguide Design for Heat-Assisted Magnetic Recording Applications," *IEEE Transactions on Magnetics,* vol. 50, no. 1, 2014.

[140] J. A. Schuller et al., "Plasmonics for Extreme Light Concentration and Manipulation," *Nature Materials,* vol. 9, no. 3, pp. 193-204, 2010.

[141] B. Xu et al., "Relationship Between Near Field Optical Transducer Laser Absorption and its Efficiency," *IEEE TRANSACTIONS ON MAGNETICS,* vol. 48, no. 5, 2012.